Resonance Ionization Spectroscopy of Protactinium

Studies on Intrinsic Quantum Chaos and the Ionization Potential

Dissertation

zur Erlangung des Grades
„Doktor der Naturwissenschaften“
am Fachbereich Physik, Mathematik und Informatik (FB 08)
der Johannes Gutenberg-Universität Mainz

Pascal Naubereit
geb. in Aschaffenburg

Carl Zeiss Stiftung

LARISSA

JOHANNES GUTENBERG UNIVERSITÄT MAINZ

JG|U

Mainz, den 30. Mai 2020

Tag der Prüfung: 2. Oktober 2020

Pascal Naubereit
WA QUANTUM/LARISSA
Institut für Physik
Staudingerweg 7
Johannes Gutenberg-Universität D-55128 Mainz
naubereit@uni-mainz.de

Abstract

The rare and all-radioactive actinide element protactinium (Pa) is one of the very few examples where even the most powerful experimental technique of resonance ionization spectroscopy (RIS) ultimately reaches its limits. On the one hand, the chemical properties of this element hinders the efficient production of a stable ion beam using RIS in a hot cavity ion source. Additionally, only small sample sizes of Pa can be used for the measurements due to its radioactivity and due its availability at all. On the other hand, even in the case one does really succeed to record atomic spectra, the analysis is strongly hampered due to the extraordinary complexity of the observed level structure.

The present thesis is addressing exactly these challenges. This is why the spectroscopy and especially the subsequent analysis of the spectra make up the main part of this work. Beforehand, the method RIS as well as the apparatus used need to be introduced. Following a generalized introduction, an explanation of RIS, the laser system and the spectrometer setup used, a first featured article, *Resonance ionization spectroscopy of sodium Rydberg levels using difference frequency generation of high-repetition-rate pulsed Ti:sapphire lasers*, validates RIS in combination with Rydberg analysis as method of choice for extraction of the ionization potential (IP) of almost any element. Additionally, the tool of difference frequency generation was applied to the Mainz Ti:sapphire lasers in order to significantly enlarge their available wavelength range.

Most often, highly elaborate experiments are only possible if a functional and diversified research network of expert groups is working together. Luckily, the LARISSA working group has built up a set of several valuable collaborations. Exemplarily, the outcome of one of those collaborations is presented in the second featured article, *Developments towards in-gas-jet laser spectroscopy studies of actinium isotopes at LISOL*, describing preparatory activities, which will give rise to many upcoming collaborative publications. Here, the novel technique of RIS in a supersonic gas jet was tested and approved to be highly efficient as well as to offer extremely high spectral resolution in the obtained data, which both is necessary for on-line production and investigations of rare isotopes far-off stability.

The main part of the present thesis comprises different studies on the actinide element protactinium. At first, a sketch of the history of its discovery and the challenges one has to face for its study are presented. In the following third publication,

Excited atomic energy levels in protactinium by resonance ionization spectroscopy, the RIS measurements on protactinium are presented. A rather large contribution to this article is also the level analysis which was necessary to arrange the vast collection of energy levels in proper order. More than 1500 energy levels with excitation energies of up to 50000 cm^{-1} were extracted from the extremely dense spectra.

After spectroscopy, the subsequent chapter addresses the search for the IP of Pa. Since all conventional methods could not be successfully applied to the withstanding element, a procedure implying a combination of two different methods of analysis has been developed and is presented in detail. With this procedure the extraction of the IP from the complex level structure of the RIS spectra was achieved and led to an IP of $E_{IP}^{Pa} = 49034(10)$ cm^{-1}.

Due to the extraordinary complexity of the Pa spectra, the presence of intrinsic quantum chaos (IQC) was speculated. Despite the fact, that this introduces a completely new research area to the LARISSA group, the last chapter of the thesis' main part covers this assumption including a qualitative introduction to quantum chaos and a complete analysis of the spectra regarding IQC aspects. The results of this analysis are comprised in a forth featured publication, *Intrinsic quantum chaos and spectral fluctuations within the protactinium atom*. Herein, the spectral statistics were investigated thoroughly and the influence of missing levels or mixed level sets was analyzed in detail.

List of Included Articles

Four peer-reviewed publications together with Chapter 4 form the basis of this cumulative thesis. They show the outcome of three years of research, mainly done in the LARISSA[1] laboratories in Mainz, but also within several international collaborations. Even though the data for Article I was already gathered before the PhD studies were started, the main analysis was carried out during this period. It gives an overview of the method of resonance ionization spectroscopy in general, including the laser sources and the analysis methods applied within the LARISSA group, whereas Article II is an example of the excellent collaborative work marking the LARISSA network. Articles III and IV illustrate the extensive work invested into the spectroscopy and analysis of the protactinium atom. Chapter 4 also belongs to the latter research topic, but, unfortunately, a successful preparation and submission of a publication was not yet feasible withing the timeframe of this work, however it is still planned for the near future, based on the considerations given here.

Article I: *Resonance ionization spectroscopy of sodium Rydberg levels using difference frequency generation of high-repetition-rate pulsed Ti:sapphire lasers.*
P. Naubereit, J. Marín-Sáez, F. Schneider, A. Hakimi, M. Franzmann, T. Kron, S. Richter, and K. Wendt.
Phys. Rev. A **93**, 052518 (2016).

Article II: *Developments towards in-gas-jet laser spectroscopy studies of actinium isotopes at LISOL.*
S. Raeder, B. Bastin, M. Block, P. Creemers, P. Delahaye, R. Ferrer, X. Fléchard, S. Franchoo, L. Ghys, L.P. Gaffney, C. Granados, R. Heinke, L. Hijazi, M. Huyse, T. Kron, Yu. Kudryavtsev, M. Laatiaoui, N. Lecesne, F. Luton, I.D. Moore, Y. Martinez, E. Mogilevskiy, **P. Naubereit**, J. Piot, S. Rothe, H. Savajols, S. Sels, V. Sonnenschein, E. Traykov, C. Van Beveren, P. Van den Bergh, P. Van Duppen, K. Wendt, and A. Zadvornaya.
Nucl. Instrum. Meth. B **376**, 382 (2016).

[1] LAser Resonance Ionization Spectroscopy and Selective Applications

Article III: *Excited atomic energy levels in protactinium by resonance ionization spectroscopy.*
P. Naubereit, T. Gottwald, D. Studer, and K. Wendt.
Phys. Rev. A **98**, 022505 (2018).

Article IV: *Intrinsic quantum chaos and spectral fluctuations within the protactinium atom.*
P. Naubereit, D. Studer, A.V. Viatkina, A. Buchleitner, B. Dietz, V.V. Flambaum, and K. Wendt.
Phys. Rev. A **98**, 022506 (2018).

Contents

List of Figures

The figures appearing in the featured publications are not given in this listing.

List of Abbreviations

AC	Autocorrelation
AI	Auto-Ionizing state
CERN	Former french *Conseil européen pour la recherche nucléaire,* now European Organization for Nuclear Research
CM	Curved Mirror
CRC	French: *Centre de Recherche du Cyclotron*
CRIS	Collinear Resonance Ionization Spectroscopy
DFG	Difference Frequency Generation
DFI	Delayed Field Ionization
EA	Electron Affinity
EM	End Mirror
FHG	Fourth Harmonic Generation
FPE	Fabry-Pérot Etalon
G	(Refraction) Grating
GANIL	French: *Grand Accélérateur National d'Ions Lourds*
GOE	Gaussian Orthogonal Ensemble
GISELE	Ganil Ion Source using Electron Laser Excitation
HWHM	Half Width at Half Maximum
IAESTE	International Association for the Exchange of Students for Technical Experience
ICE	Isolated Core Excitation

IGISOL	Ion Guide Isotope Separation On-Line
IGLIS	In-Gas-Laser Ionization and Spectroscopy
IP	Ionization Potential
IQC	Intrinsic Quantum Chaos
ISAC	Isotope Separator and Accelerator
ISOLDE	Isotope Separator On Line DEvice
JYFL	Jyväskylä accelerator laboratory
LARISSA	LAser Resonance Ionization Spectroscopy and Selective Applications
LDC	Level Density Collapse
LF	Lyot Filter, synonymous birefringent filter
LISOL	Leuven Isotope Separator On-Line
MABU	Mainz Atomic Beam Unit
OC	Output Coupler
PALIS	PArasitic Laser Ion-Source
PBE	Prism Beam Expander
PL	Pump Lens
PM	Pump Mirror
RC	Rydberg Correlation
RIB	Radioactive Ion Beam
RIBF	Radioactive Ion Beam Factory
RIKEN	From Japanese: Institute of physics and chemistry
RILIS	Resonance Ionization Laser Ion Source
RIS	Resonance Ionization Spectroscopy
RMT	Random Matrix Theory
S3	Super Separator Spectrometer
SFG	Sum Frequency Generation

SHG Second Harmonic Generation

SPIRAL2 French: *Système de Production d'Ions RAdioactifs en Ligne* generation 2

SPM Saddle Point Model

Ti:sapphire Titanium doped Al_2O_3 (sapphire)

THG Third Harmonic Generation

TRILIS TRIUMF Resonance Ionization Laser Ion Source

TRIUMF TRI University Meson Facility

UKAEA United Kingdom Atomic Energy Authority

Chapter 1

Introduction

The LARISSA group is looking back onto a long history of research studies in the field of resonance ionization spectroscopy (RIS). During almost three decades, the group around Prof. Dr. Klaus Wendt gained widespread experiences not only in the general field of RIS, but also in a variety of adjacent research areas. RIS can be used as a powerful tool for fundamental investigations in atomic physics, but also serves as methodical link to the large field of studies on ground state properties of atomic nuclei in nuclear physics. Based on an active worldwide research network, the group takes part in many collaborative activities at several Radioactive ion beam (RIB) facilities located usually at specific large scale research institutions. RIS is the tool, par excellence, to explore the formation of matter in the early universe. In this way, it is also the basis for this thesis. Its specific properties as well as the dedicated laser system developments by the group for different applications and collaborations within the LARISSA network are introduced in the first chapter of this thesis.

Besides this, the treatment and removal of still open spaces of knowledge regarding fundamental atomic properties, i.e. the ionization potential (IP) or electron affinity (EA), evolved quickly to the pet passion of the LARISSA group. During the years, many of such left-over gaps in the list of data on atomic elements could be closed, including, e.g. the direct measurement of the IP and EA of astatine, often referred to as the rarest naturally occurring element in the earth's crust [1,2], or the IP of various members of the lanthanide and actinide groups as well as further elements of the periodic table, e.g. in the region of the transition metals, see for example [3–5,22,37]. Many of the elements investigated in these studies are rare, radioactive and exhibit specifically complex atomic spectra. Nonetheless, the ionization potential could be determined, either by a direct measurement studying the convergence of Rydberg series or by an indirect approach applying e.g. field ionization within the saddle point model. The element protactinium has shown to be a very peculiar, unmanageable case: The IP of this actinide could not be determined by using the standard RIS techniques, neither via a direct nor an indirect approach. Even after several elabo-

rate measurement campaigns, this fundamental atomic property of Pa could not be unveiled due to unpleasant chemical properties in combination with an exceptional complex atomic spectrum do far. On the other hand, this atomic structure, especially the high level density, is used within this thesis to elicit the IP of protactinium. Analytical methods dedicatedly developed for this purpose were applied to the different atomic RIS excitation schemes of protactinium, which lead to a final value for the IP in the end.

The final determination of the IP is not the only scientifically relevant information obtained from the complex RIS spectra of protactinium. A rather different research field, completely new for the doctoral candidate as well as for the whole LARISSA group, was initiated by the statement, how *chaotic* those spectra look. Since studies on quantum chaos experienced a renaissance in the 1990's and early 2000's by investigating microwave systems, also studies on many other complex quantum chaotical systems became possible by more sophisticated research techniques. In this context, the protactinium spectrum was investigated regarding intrinsic quantum chaos (IQC) during the PhD studies documented here. It is the first time, that an atomic system of such complexity was accessible for quantum chaos research, making it even more interesting. Nonetheless, with stepping into this rather advanced, very theoretical research field, the whole LARISSA group break fresh ground. Even though it was somewhat difficult and time consuming to get used to the new topic, it delivered a valuable outcome with many stimulating ideas and new scientific contacts. The topic gained interest by several experts in the field requesting presentations and discussion meetings about the quantum chaos in protactinium. All results found during this lively period were put together in a publication featured in the last chapter of this thesis.

Lastly it should be mentioned, that this thesis is not foreseen to replace elaborate textbooks. Therefore, in each of the sections not the full-depth theory, which can anyhow easily be found in these books for further reading, is given. Rather, the introductory parts of different chapters are addressed and compiled for the non-expert readers, so that the featured publications can be understood. Nonetheless, for interested readers, who want to develop deeper insight into the individual topics, further reading is given as reference.

Chapter 2

Resonance ionization spectroscopy

With the first description and utilization of RIS by Ambartzumian, Letokhov & Mishin [6,7], a new versatile technique for investigation not only on atomic but also on nuclear fundamental properties was born. It is based on a successive excitation of one (or more) valence electron(s) via laser radiation precisely in tune with atomic transitions. A last excitation step, resonant or non-resonant, finally ionizes the atom and, thus, the resulting ion can be manipulated by electric or magnetic fields and then be detected with highest probability. Exceptional elemental selectivity, exceeding other excitation or ionization methods, is ensured by the resonant excitation since the atomic transitions used are unique for every element. Even isotopic selectivity can be achieved if the laser linewidth is below the isotope shift between the transitions of specific isotopes of one element.

Resonance ionization is most often used in combination with a hot-cavity source for efficient atomization followed by a conventional mass separator. Thus, isobaric contaminants, stemming e.g. from surface ionization or non-resonant laser ionization, can be successfully eliminated. For more information on RIS, laser spectroscopy in general and correlated experiments in the atomic physics as well as the nuclear physics sector, please see the reviews [8,9].

The resonance ionization spectroscopy performed in the low-energy mass spectrometer MABU in the laboratory of the LARISSA group in Mainz serves as starting point for all publications this thesis is based on. Therefore, in the following sections a short summary of the utilized laser systems, the mass separator and the spectroscopic technique is comprised. Thereafter, the first publication *Resonance ionization spectroscopy of sodium Rydberg levels using difference frequency generation of high-repetition-rate pulsed Ti:sapphire lasers* is presented. This work explains the enlargement of the accessible Ti:sapphire wavelength range by difference frequency generation (DFG) as well as validates our method of Rydberg spectroscopy by comparing the measured ionization potential to the well-known IP of sodium.

2.1 Mainz Ti:sapphire laser system

For RIS, a broadly tunable, narrow bandwidth, highly stable and maintenance-free, pulsed laser system with high output power is essential. Since a laser system comprising all mentioned properties is not or at least not affordably available commercially, the laser systems were originally developed and stepwise updated and optimized within the Mainz LARISSA working group. Today, they are used at almost exclusively all leading RIB facilities worldwide. Ti:sapphire as active medium is most suitable for matching the above listed requirements.

Sapphire, an Al_2O_3 crystal, is therefore doped with Ti^{3+}-ions, so that the vibrationally broadened $^2T_2$ triplet and ^2E doublet of the Ti^{3+}-ion embedded in the lattice structure form the emission and absorption bands, respectively, of this quasi-four-level laser system. Fig. 2.1(a) shows a schematic view of the quasi-four-level scheme of a Ti:sapphire laser, where the absorption band is given as red shaded area allowing for pump wavelengths between 420 nm and 600 nm and the emission band as green shaded area allowing for stimulated emission in a range between 650 nm and 1100 nm, while Fig. 2.1(b) gives the absorption and emission spectra of Ti:Sapphire.

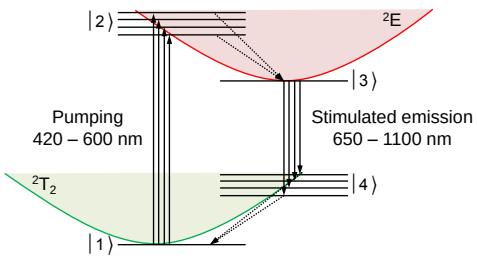

(a) Quasi-four-level laser system of Ti:sapphire. The red and green shaded areas depict the absorption and emission band of the Ti^{3+}-ion embedded in the sapphire crystal lattice. Graphic taken from [10].

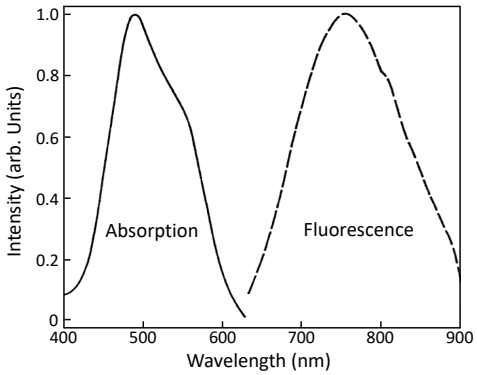

(b) Absorption and emission spectrum of Ti:sapphire. Figure adapted from [13].

Figure 2.1: Properties of Ti:sapphire as laser crystal.

The basic laser theory and principle of the Ti:sapphire laser shall not be given here since it can be found in great detail in numerous textbooks, theses or scientific articles [11–17].

2.1.1 Specialized versions of the Mainz lasers

All types of the Mainz Ti:sapphire lasers have some general properties in common, which are the repetition rate of typically 10 kHz, the pulse length between 30 ns and 80 ns, the high beam quality with $M^2 < 1.3$ and the average output powers between 1 W and 4 W. Nevertheless, different experimental requirements and needs led to specialized versions of the Mainz Ti:sapphire laser system. The main properties of a laser are primarily defined by the shape of the resonator cavity and the installed frequency selective elements. In this way, also the unique properties of the three main types of the Mainz Ti:sapphire lasers are defined:

Standard Ti:sapphire laser: The standard version of the Mainz Ti:sapphire laser is a high-stable low-maintenance system that is mostly used. A Z-shaped resonator with birefringent filter and Fabry-Pérot etalon enables high average output powers with suitable low laser linewidths. More details can be found in [18].

Grating-assisted Ti:sapphire laser: This version is based on a refraction grating as frequency selective element, which allows continuous and mode-hop-free wavelength tuning over almost the complete Ti:sapphire emission range. It is the most versatile system ensuring low linewidth and high output power aside of the wide-range scan-ability. The current stage of this system was developed in [15].

Injection-locked Ti:sapphire laser: Injection locking of a bow-tie traveling-wave resonator with a diode laser enables very narrow output linewidths with reasonable average output powers. This most elaborate system is used for experimental approaches relying on extremely narrow linewidths. [16] gives an overview on this Ti:sapphire laser.

Since the first two versions are frequently used throughout this work, their schematics are displayed in Fig. 2.2. Characteristics of all types of the Mainz Ti:sapphire laser systems can be found e.g. in [15,16].

2.1.2 Frequency conversion

Most optical atomic transitions between low-lying levels lie in the visible up to the blue or ultraviolet spectral range. Unfortunately, many of those are not directly reachable with the near-infrared radiation of the fundamental Ti:sapphire wavelength. Making use of non-linear optical processes the frequency of (pulsed) laser radiation can easily be converted, what can be applied for a very useful extension of the achievable wavelength range for Ti:sapphire lasers as well. Non-linear optical processes like second/third/fourth harmonic generation (SHG/THG/FHG), sum frequency generation (SFG) or difference frequency generation (DFG) require crystals with a non-linear optical susceptibility and additional birefringent properties

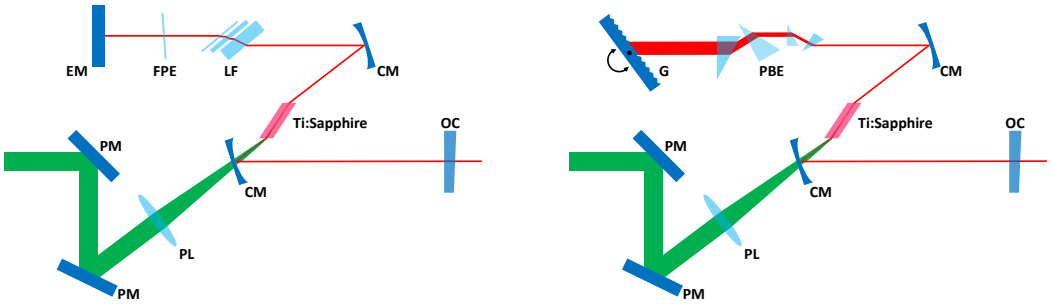

(a) Standard laser.

(b) Grating-assisted laser.

Figure 2.2: Schematics of the most common types of the Mainz Ti:sapphire laser system. Graphics adapted from [15], the explanation of the abbreviations can be found in the List of Abbreviations.

for enabling the necessary phase matching. Note, that for the sake of efficiency, the third harmonic is usually generated via a SFG process and the fourth harmonic via applying the SHG process twice. Optical media fulfilling these requirements are for example β-barium borate (BBO), bismuth borate (BiBO) or lithium triborate (LBO). The theory of non-linear optics is primarily given in [19] while the basics for SHG and DFG especially with pulsed Ti:sapphire lasers can also be found in [15, 20] as well as in the publication *Resonance ionization spectroscopy of sodium Rydberg levels using difference frequency generation of high-repetition-rate pulsed Ti:sapphire lasers*.

Fig. 2.3 shows a compilation of all wavelength ranges that are reachable with Ti:sapphire lasers involving frequency conversion processes.

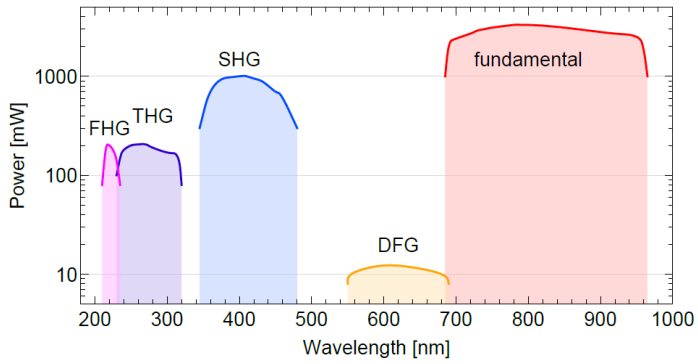

Figure 2.3: Compilation of wavelength ranges accessible with the Mainz Ti:sapphire lasers involving frequency conversion. Graphic adapted from [16].

2.2 Experiment and technique

2.2.1 Mainz atomic beam unit

The Mainz atomic beam unit (MABU) is a low-energy mass spectrometer equipped with a radio-frequency quadrupole for mass filtering. This table-top experiment, as given in Fig. 2.4(a), needs only very low voltages in the order of a few 100 V for ion extraction and ion beam shaping which makes it comfortable to use. Free atoms for resonant laser ionization are generated in a resistively heated atomizer furnace as shown in Fig. 2.4(b). After ionization and extraction, beam-shaping, mass-filtering and final detection of the ions on a channel electron multiplier in single ion counting mode is carried out. The apparatus is described in great detail in [21]. More Information can also be found in the upcoming publications *Resonance ionization spectroscopy of sodium Rydberg levels using difference frequency generation of high-repetition-rate pulsed Ti:sapphire lasers* and *Excited atomic energy levels in protactinium by resonance ionization spectroscopy*.

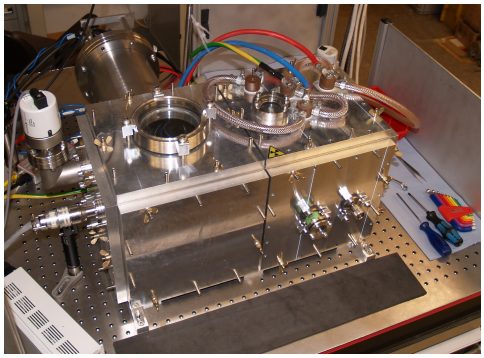

(a) Photograph of the MABU.

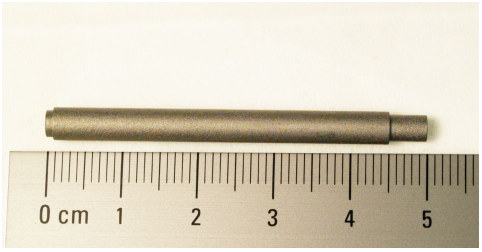

(b) Photograph of an atomizer furnace for the MABU.

Figure 2.4: Photographs of the Mainz atomic beam unit. Pictures taken from [21].

2.2.2 RIS technique

Within the atomizer furnace, which serves as atom-laser-interaction region, the evaporated atoms of an sample are excited by a set of two or three Ti:sapphire lasers. Obeying the transition rules for optical dipole transitions, the valence electron(s) are stepwise excited into high-lying energy states before the final ionization takes place.

Fig. 2.5 shows a generalized ionization scheme with typical excitation steps and three different possibilities for the last ionization step. Note, that an excitation via ν_{02} and via ν_{01} and ν_{12} into the same energy level $|2\rangle$ is not possible, because a change in parity is mandatory for every transition. Ionization takes place as soon as the energy of the valence electron is raised above the IP of the investigated element. In RIS, a distinction is made between resonant and non-resonant ionization. For

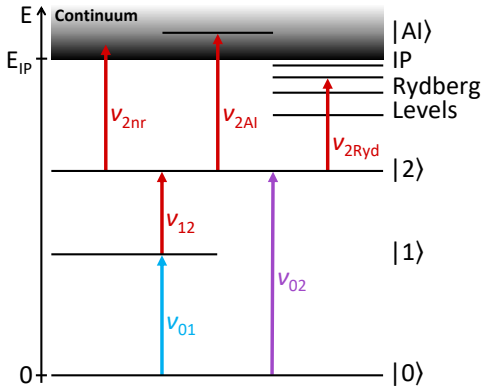

Figure 2.5: Generalized RIS ionization scheme. For details, please see text. Graphic adapted from [15].

the latter, an ionization laser excites the electron into the continuum above the IP. Much higher ionization efficiency can be achieved in the resonant case, namely if an auto-ionizing state (AI) is excited. Such an AI is a multi-electron excitation that transfers its energy with rather short decay times to a single electron whose energy is than high enough to exit the atom. A third also highly efficient ionization process implies the intermediate excitation of Rydberg states. Rydberg states are highly excited, only weakly bound energy levels with high principle quantum numbers n located just below the IP. These states are easily ionized by "third-party" processes as i.e. black-body radiation, electric or magnetic fields and collisions with other atoms, ions or electrons. A series of Rydberg levels converges towards the IP proportional to $1/n^2$, correspondingly the spectroscopy of Rydberg levels is often used for the direct determination of the IP, as also done in the publication presented in Sec. 2.3. More information on Rydberg spectroscopy and other methods for determining a value for the IP can be found e.g. in [22] or briefly in Sec. 4.

In spectra determined via RIS, the measured resonances exhibit typical line shapes. Several broadening effects determine the observed linewidth of the resonances. The most important underlying effects are discussed in the publication *Resonance ionization spectroscopy of sodium Rydberg levels using difference frequency generation of high-repetition-rate pulsed Ti:sapphire lasers*. Very detailed information on the RIS technique and selected experiments can be found for example in [8,9,23,24].

2.3 Publication: Resonance ionization spectroscopy of sodium Rydberg levels using difference frequency generation of high-repetition-rate pulsed Ti:sapphire lasers

The article was published in 2016 in *Physical Review A* although the data was already collected between autumn 2013 and spring 2014. In the meantime a proceeding [20] was published presenting details on the DFG with pulsed Ti:sapphire lasers and demonstrating the ionization of sodium via its famous D-doublet. The objective of the article presented herein was to demonstrate the RIS on transitions, where formerly dye-lasers were necessary. With the obvious spectroscopy of sodium via the famous D-lines in the orange wavelength regime, a showcase for the application and evaluation of the spectroscopic technique and the verification of the IP determination method via Rydberg convergences was given at the same time.

In the context of this thesis, the article gives a very valuable overview on the laser system involving frequency conversion, on the mass spectrometer MABU, as well as on several issues concerning the RIS method in general, i.e. the resonance broadening effects, on Rydberg spectroscopy and the therewith given possibility of a direct determination of the ionization potential.

As main author, the doctoral candidate not only prepared the manuscript of this publication, but also supervised the Spanish student Julia Marín-Sáez during her IAESTE internship and was responsible for the entire measurement campaign on NA and prepared the analysis given in this article.

Resonance ionization spectroscopy of sodium Rydberg levels using difference frequency generation of high-repetition-rate pulsed Ti:sapphire lasers

P. Naubereit,[*] J. Marín-Sáez,[†] F. Schneider, A. Hakimi, M. Franzmann,[‡] T. Kron, S. Richter, and K. Wendt
Institute of Physics, University of Mainz, D-55128 Mainz, Germany
(Received 8 March 2016; published 31 May 2016)

The generation of tunable laser light in the green to orange spectral range has generally been a deficiency of solid-state lasers. Hence, the formalisms of difference frequency generation (DFG) and optical parametric processes are well known, but the DFG of pulsed solid-state lasers was rarely efficient enough for its use in resonance ionization spectroscopy. Difference frequency generation of high-repetition-rate Ti:sapphire lasers was demonstrated for resonance ionization of sodium by efficiently exciting the well-known D_1 and D_2 lines in the orange spectral range (both ≈ 589 nm). In order to prove the applicability of the laser system for its use at resonance ionization laser ion sources of radioactive ion beam facilities, the first ionization potential of Na was remeasured by three-step resonance ionization into Rydberg levels and investigating Rydberg convergences. A result of $E_{\mathrm{IP}} = 41449.455(6)_{\mathrm{stat}}(7)_{\mathrm{sys}}\ \mathrm{cm}^{-1}$ was obtained, which is in perfect agreement with the literature value of $E_{\mathrm{IP}}^{\mathrm{lit}} = 41449.451(2)\ \mathrm{cm}^{-1}$. A total of 41 level positions for the odd-parity Rydberg series $nf\ ^2F^{o}_{5/2,7/2}$ for principal quantum numbers of $10 \leqslant n \leqslant 60$ were determined experimentally.

DOI: 10.1103/PhysRevA.93.052518

I. INTRODUCTION

Powerful tunable high-repetition-rate solid-state lasers are a most useful tool for spectroscopy and ion production at radioactive ion beam (RIB) facilities, which use resonance ionization laser ion sources (RILIS). Those lasers may be used in long-term stable and almost maintenance-free continuous operation and, moreover, they permit a rather simple spectral range extension by generation of the second, third, or fourth harmonic. Using a titanium:sapphire crystal as active laser medium a wavelength coverage of 680 nm to 1000 nm in fundamental mode and 210 nm to 450 nm by using frequency doubling, tripling and quadrupling, has been demonstrated. Nevertheless, a remaining gap in the visible spectral range between the fundamental (> 680 nm) and the second harmonic (< 450 nm) output is remaining. The second-order nonlinear process of difference frequency generation (DFG) allows to close that gap. The theory of this process can be found for example in [1]. The desired wavelength range is also achievable with a variety of different laser systems with or without DFG. Most of them are even commercially available for many years. However, those systems do not really fulfill the requirements at on-line facilities as pointed out explicitly above. Continuous-wave laser systems, for example, operating as Raman lasers [2] or using sum frequency generation [3], are not able to provide either the high output energies or the spectral coverage needed for saturation of a broadened excitation line for a thermal atom ensemble, in particular regarding weaker atomic transitions. In contrast, high pulse energies are needed for optical parametric oscillators or amplifiers [4] and are in most cases only achieved at low repetition rates. The corresponding duty cycle losses of such low-repetition-rate operation are a huge disadvantage concerning the efficiencies of ion production at RIB facilities. Dye lasers instead can provide both high repetition rate and high pulse energies with a broad range of output wavelengths [5]. Unlike the high-repetition-rate solid-state lasers, however, dye lasers need a lot of maintenance and care during long-term operation in order to guarantee suitable performance and stability as needed at RIB facilities. The principle of the DFG approach has been demonstrated using high-repetition-rate ns Ti:sapphire lasers in [6]. In this work, the reliable application in high-resolution multistep resonance ionization spectroscopy is shown.

As an evaluation case, Rydberg spectroscopy on the element with the probably best known transitions in the orange wavelength regime around 590 nm was chosen by addressing the famous D_1 and D_2 doublet lines of sodium. By using three-step resonance ionization, involving DFG in the first excitation step, spectroscopy around the sodium ionization potential was performed and its value was redetermined. Although this value has been known with high precision since 1992 ($E_{\mathrm{IP}}^{\mathrm{lit}} = 41449.451(2)\,\mathrm{cm}^{-1}$ [7,8]), energies of higher lying levels of odd-parity Rydberg series like $nf\ ^2F^{o}_{5/2,7/2}$ were just published for the first time during the analysis of our data in 2015 by Nadeem and co-workers [9]. These authors give an elaborate overview on the atomic spectroscopy of high-lying levels of sodium, to which we refer here for a general overview. They have carried out two-color, three-step resonance excitation based upon the $3s$-$3d$ two-photon transition from the ground state and finally populate nf levels in the range $15 \leqslant n \leqslant 51$. Results include level energies and oscillator strengths. They report an uncertainty of their level energies of $0.2\,\mathrm{cm}^{-1}$ due to strong broadening effects in their thermionic diode setup, which is almost one order of magnitude less precise than the results of our measurements with in-source laser geometry on a well-collimated atomic beam. In addition, our data, resulting from three-color, three-step resonance excitation along two different excitation ladders, which were based upon the D_1 and D_2 ground-state transitions, respectively, extend to higher principal quantum numbers of up to $n = 60$. Correspondingly,

[*]naubereit@uni-mainz.de
[†]Present address: Applied Physics Section of the Environmental Department, University of Lleida, Escuela Politécnica Superior, Jaume II 69, 25001 Lleida, Spain.
[‡]Institute for Radioecology and Radiation Protection, University of Hannover, D-30419 Hannover, Germany.

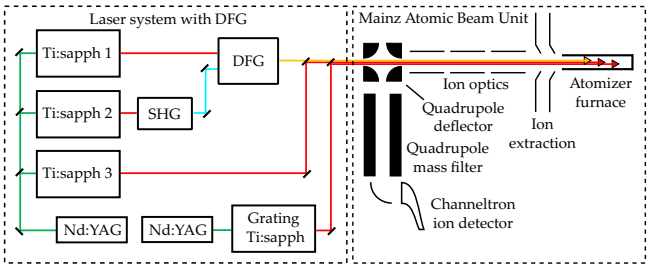

FIG. 1. Sketch of the experimental setup including the laser system and the atomic beam mass spectrometer unit MABU.

we have attempted a full Rydberg-Ritz analysis of our data including earlier known literature data as bandheads and redetermined the ionization potential with high accuracy. This approach resulted in a confirmation of the high-precision literature value of $E_{\mathrm{IP}}^{\mathrm{lit}} = 41449.451(2)\,\mathrm{cm}^{-1}$ from [7,8] in an independent measurement.

II. APPARATUS

Figure 1 gives an overview of the experimental apparatus used. It consists of two distinct components: the dedicated high-repetition-rate solid-state laser system including the DFG unit and the atomic beam apparatus with single ion detection MABU (Mainz atomic beam unit).

A. Laser system

1. General layout

For a resonant three-step ionization process involving DFG, four Ti:sapphire lasers are necessary: Two of them provide the input for the DFG, which is used for the first excitation step. The higher energetic pump wave of the DFG process is generated by frequency doubling of the fundamental laser light in a BBO crystal. The lower energetic, subtracted idler wave is provided in the fundamental infrared range of the Ti:sapphire laser. The radiation of the third laser excites the atoms in a second resonant step into the second excited state. Those three lasers are based on the standard Z-shaped cavity design of the Mainz Ti:sapphire lasers in the latest design according to [10]. The ionization step is then provided from a fourth laser, which is a grating-assisted Ti:sapphire laser [11] to guarantee a wide, continuously tunable scanning range.

To achieve sufficient pump power and temporal synchronous output pulses of the Ti:sapphire lasers, two commercial frequency-doubled Nd:YAG pump lasers with 10-kHz repetition rates (Quantronix Hawk-Pro 532-60-M and Photonics Industries DM 80-532) were used. The standard Mainz Ti:sapphire lasers provide an average power between 2 and 4 W at pump powers of 15 W. The pulse lengths span from 25 ns at the gain maximum of $\approx$ 810 nm to 100 ns at the edges of the tuning range around 700 and 1000 nm, respectively, whereas the spectral bandwidth amounts to typically $\Delta\nu_{\mathrm{fund}} = 4(1)$ GHz. In the experiment the grating-assisted laser had an output power of $\approx$ 280 mW with a bandwidth of 2 GHz. The lasers show a good long-term stability with frequency drifts of less than 1 GHz a day. Nevertheless, the wavelengths of all lasers were actively monitored during the experiment.

2. Considerations for difference frequency generation

In [6] a high-repetition-rate, pulsed, narrow-bandwidth Ti:sapphire laser involving injection locking was used for DFG. This laser has both a narrow bandwidth of 20 MHz and a suitable output power of 2.6 W. Frequency doubling was carried out in a very efficient but somewhat delicate intracavity approach. Despite some advantages of this setup, we followed a different approach here and used the standard Mainz Ti:sapphire lasers as described above to guarantee the universality of the DFG system without involving and controlling the sophisticated injection locking procedure. In addition we abstained from intracavity doubling for the DFG pump photon generation to provide a more simple frequency-tuning procedure for both the second harmonic light and the DFG light at the expense of a reduced output power. Based on calculations for optimization of the mixing process with the software SNLO [12], we expected considerable losses in the DFG process, as the different available BBO crystals had to be tilted quite far off from orthogonal orientation due to imperfect cutting angles for proper phase matching. After the mixing stage the laser beam in addition had to pass several dispersive optics, e.g., dichroitic mirrors and prisms, in order to separate the DFG light from the remaining blue and infrared parts. Regarding those limitations we expected rather low output power of the DFG light of just a few mW. Keeping in mind the pulsed structure of the laser light with a duty cycle of 10^{-3} this value should nevertheless ensure saturation of all reasonably strong optical transitions under our experimental conditions.

B. Atomic beam unit MABU

The atomic spectroscopy, mass separation, and detection of the sodium ions were performed in the atomic beam unit MABU. This machine is a low-energy mass spectrometer with an extraction field of well below 10 V/mm. For chemical decomposition of the sample molecule $NaHCO_3$, reduction and final atomization, a microscopic sample of a few mg was placed in a resistively heated graphite furnace with a diameter of 2.2 mm and a length of 50 mm. The laser beams were directed into the atomic vapor, which formed inside the hot cavity, to induce resonant multistep excitation of the sodium atoms into Rydberg levels, from which they ionize through collisions, black-body radiation from the heated furnace, as well as influences from the electric extraction field. Field ionization of Rydberg atoms is rather strong, but in our case gives only small contributions due to the low tension applied in the extraction region of our apparatus. The individual strengths of the remaining processes cannot easily be disentangled. After acceleration and beam shaping, the ions were guided through an electrostatic 90° quadrupole deflector to remove background from neutral species and a radio-frequency quadrupole mass filter to isolate ^{23}Na from other disturbing masses. Subsequently the highly isotopic pure ion beam was detected by an off-axis-mounted channel electron multiplier in single-ion counting operation.

III. RESULTS

A. Difference frequency generation

One of the two lasers necessary for DFG operated in its fundamental wavelength regime at a wavelength of 920 nm with an average output power of 2500 mW (idler). The second laser operated at 718 nm with 2900 mW and was externally frequency doubled using a BBO crystal cut at 32.8° for type I phase matching (pump). We achieved 700 mW in the blue spectral range around at 359 nm. The light was collimated, separated from the remaining fundamental light, and then focused together with the infrared light into another BBO crystal for DFG. Here, we also implemented type I phase matching at a BBO angle of 32°, which means that both the infrared idler wave and the DFG wave were in ordinary polarization (o) while the frequency-doubled pump light was introduced as an extraordinary (e) wave ($oo \rightarrow e$). After its generation, the DFG light was collimated and separated from the remaining idler and pump parts by a combination of different dichroitic mirrors and dispersive prisms, primarily to allow for power determination. With this simplified setup we obtained up to 11 mW of average power for the DFG light at 589 nm in good agreement with the expectations from the calculations. The overall conversion efficiency is $I_{\mathrm{DFG}}/(I_{\mathrm{idler}} + I_{\mathrm{pump}}) = 0.3\ \%$, which may be increased by using, e.g., the type II phase matching with a BBO suitably cut at 41.5° [12]. Due to the high transition strength of the sodium D lines, less than 2 mW of the DFG light were used for most of the spectroscopic measurements.

For the DFG laser radiation a linewidth (FWHM) of

$$\begin{aligned}\Delta\nu_{\mathrm{DFG}} &= \sqrt{\Delta\nu_{\mathrm{fund}}^2 + \Delta\nu_{\mathrm{SHG}}^2} \\ &= \sqrt{\Delta\nu_{\mathrm{fund}}^2 + (\sqrt{2}\Delta\nu_{\mathrm{fund}})^2} \\ &\approx 6.9(17)\ \mathrm{GHz} \end{aligned} \quad (1)$$

is expected, as only Gaussian contributions determine the width. The range of spectral coverage was not investigated because this is strongly dependent on the available crystals for DFG, which were not optimum during this study. With a set of four properly cut BBO crystals the range of $520 - 680$ nm should be easily accessible by DFG of our Ti:sapphire lasers. Access to the remaining gap of $450 - 520$ nm will require frequency tripling or quadrupling for the DFG pump wave, which will severely complicate the process and reduce the achievable output power.

B. Two-step excitation into the $3d\ 2D_J$ configuration

The three-step excitation scheme used in this work is shown in Fig. 2. It is based on the energy levels as given in [13]. The DFG process was used for the first transition, from the ground state $3s\ ^2S_{1/2}$ to either the level $3p\ ^2P_{1/2}$ at $16956.170\,\mathrm{cm}^{-1}$ (via the D_1 line of the doublet) or to level $3p\ ^2P_{3/2}$ at $16973.366\,\mathrm{cm}^{-1}$ (via D_2). The second transition is induced by a Ti:sapphire laser in fundamental mode to the levels $3d\ ^2D_{3/2,5/2}$ at $29172.887\,\mathrm{cm}^{-1}$ and $29172.837\,\mathrm{cm}^{-1}$, respectively, regarding the selection rule of $\Delta J = \pm 1, 0$. However, these two second excited levels are very close lying ($\Delta\nu \approx 1.5$ GHz) and due to the laser linewidth of $3 - 5$ GHz,

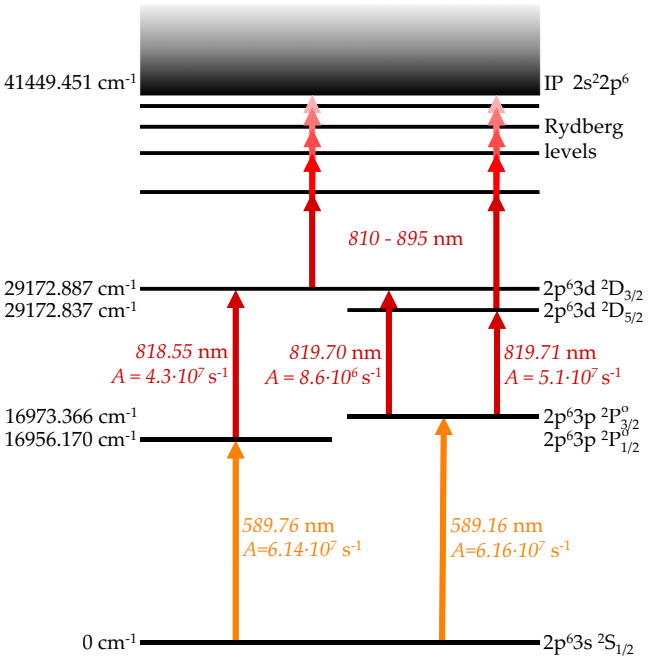

FIG. 2. Sodium excitation schemes investigated in this work. The energy level positions are taken from [13]. The lowest transition on the left side is classically denoted as the D_1 line, the right one as the D_2 line.

they were not resolved when scanning the laser frequency across the second transition. Thus, it was assumed that in the D_2 scheme the majority of the atoms were excited by the stronger transitions to the $J = 5/2$, according to the A factors in the excitation scheme of Fig. 2. For the data analysis, the energetic position of the second excited level during the D_2 excitation was set to a properly weighted intermediate value between the two fine structure sublevels.

To verify the energy position of the two first and second excited states and to get information about the bandwidth of the individual excitation steps, frequency scans on the different transitions were performed while the third step laser was tuned to above the IP for nonresonant ionization. Due to its single valence electron, the spectrum of sodium just above the IP is completely unstructured. Correspondingly, in the third step, no autoionizing state is accessible with our laser system and for excitation into the continuum no resonance structure was observed.

Figure 3 shows on the left the binned frequency scans for the first and second excitation steps of the right excitation ladder of Fig. 2 along the D_2 line and the saturation curves on the right side for all three transitions.

As expected, the saturation power of the first excitation step of 1.1(3) mW, as measured under our experimental conditions, is very low and the transition is easily saturated. The just slightly higher saturation power of 2.6(5) mW for the second step is also well expected due to a comparable oscillator strength as given in Fig. 2; the factor of 2 increase may even be ascribed to an imperfect spatial overlapping of the laser beams. Due to the different contributing broadening effects, a Voigt profile was fitted to the data points of the frequency

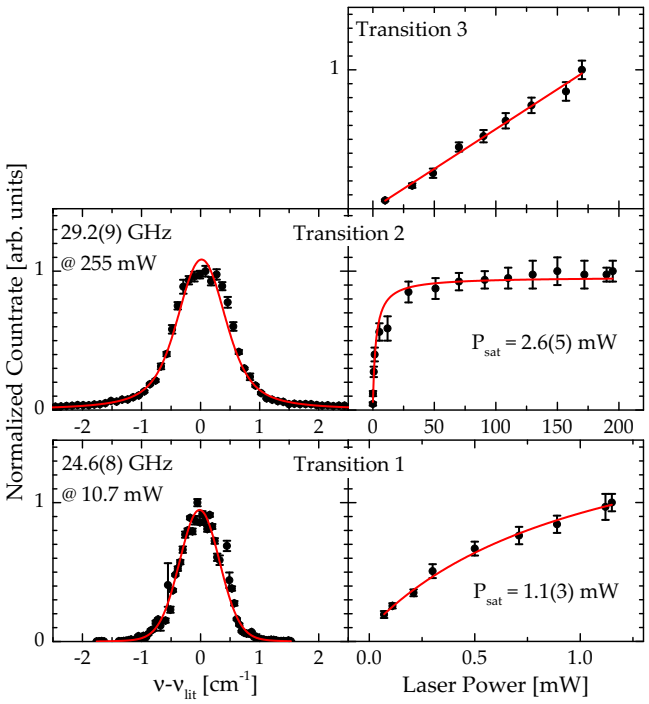

FIG. 3. Frequency scans and saturation curves of the three transitions of the excitation scheme via the D_2 line. Since the third step is nonresonantly ionizing, the resonance curve was omitted and the saturation curve has a constant slope. The extracted linewidths are noted in the graphs.

scans:

$$I(\nu) = A + B\frac{2\ln(2)}{\pi^{3/2}}\frac{\Delta\nu_L}{\Delta\nu_G^2} \times \int_{-\infty}^{\infty} \frac{\exp(-t^2)}{\left(\sqrt{\ln 2}\frac{\Delta\nu_L}{\Delta\nu_G}\right)^2 + \left(\sqrt{4\ln 2}\frac{\nu-\nu_{center}}{\Delta\nu_G} - t\right)^2} dt, \quad (2)$$

where $\Delta\nu_G$ and $\Delta\nu_L$ give the linewidths of the Gaussian and the Lorentzian contribution, respectively. The flattened top of the peak which results from the saturation is not included in the fit model. Nevertheless, the curves perfectly reproduce the outer wings of the peaks, which contain the most important information for the precise extraction of energy positions ν_{center} and FWHM $\Delta\nu$, as obtained using the numerical method given in [14] by

$$\Delta\nu = 0.5346\Delta\nu_L + \sqrt{0.2166\Delta\nu_L^2 + \Delta\nu_G^2}. \quad (3)$$

For the saturation powers P_{sat}, as quoted, a fit function with the form

$$I(P) = A + B\frac{P}{P + P_{sat}} \quad (4)$$

was applied to all three saturation curves. For the nonresonant ionization step an absolutely linear behavior was observed, as expected, for laser powers of up to 175 mW.

C. Linewidths and saturation

For the experimental linewidth of the transitions, we have to consider several contributions. Aside from the negligible natural linewidth (FWHM) of 9.8 MHz for the first step excitation [15] most of the broadening effects contribute in the GHz range. The minimal measured linewidth is limited by the laser linewidth given above. Besides this the Doppler broadening (FWHM) was taken into account with

$$\Delta\nu_{dop} = \frac{\nu_0}{c}\sqrt{\frac{8kT\ln 2}{m_{atom}}} = 2.5(1)\ \text{GHz}, \quad (5)$$

for a frequency of the transition of $\nu_0 = 508.8487$ THz, temperature in the hot furnace of $T \approx 1100$ K, as extrapolated from a pyrometric measurement, and the sodium mass $m_{atom} = 23$ u. The overall Gaussian contribution considers the linewidth of the DFG laser and the Doppler broadening, which is a small contribution due to the low oven temperatures:

$$\Delta\nu_G = \sqrt{\Delta\nu_{DFG}^2 + \Delta\nu_{dop}^2} = 7(2)\ \text{GHz}. \quad (6)$$

The saturation broadening can be approximated by a Lorentzian distribution and gives a significant contribution to the overall linewidth at a maximum laser power of 10.7(10) mW. It is calculated as (FWHM)

$$\Delta\nu_L = \Delta\nu_G\sqrt{1 + S_0} = 24(6)\ \text{GHz}, \quad (7)$$

where $\Delta\nu_G$ is the Gaussian contribution FWHM of the transition and $S_0 = \frac{I}{I_{sat}} = 10(3)$, with laser intensity I and saturation intensity of the transition I_{sat}. For combining Gaussian and Lorentzian contributions we used Eq. (3) with a resulting overall Voigt profile linewidth of the transition of

$$\Delta\nu_{calc} = 26(3)\ \text{GHz}. \quad (8)$$

For the second transition the same calculation with adapted parameters leads to a linewidth expectation of

$$32(5)\ \text{GHz}, \quad (9)$$

where the saturation parameter $S_0 = \frac{I}{I_{sat}} \times 10 = 48(14)$ must additionally be scaled by the saturation of the first excitation step. Notice that there is no additional contribution from the excitation of the pair of energy levels in that step, because this is fully covered by the five times larger laser linewidth.

The calculated linewidths of the two lower excitation steps reproduce the experimental values rather well. When addressing higher spectral resolutions, there are several ways to reduce the linewidths. The biggest contribution results from the large oversaturation, which easily is compensated for by adjusting the intensities of the lasers accordingly. The part resulting from the laser linewidth itself is more complicated to address and would require, e.g., the use of an injection locked system or alternatively a further passive wavelength selection within the laser resonator as discussed, e.g., in [6].

D. Rydberg spectroscopy

For the spectroscopy on sodium Rydberg levels, the laser for the third excitation step was continuously scanned using the wide-range tunable, grating-assisted Ti:sapphire laser to cover the energy range just below the literature value for

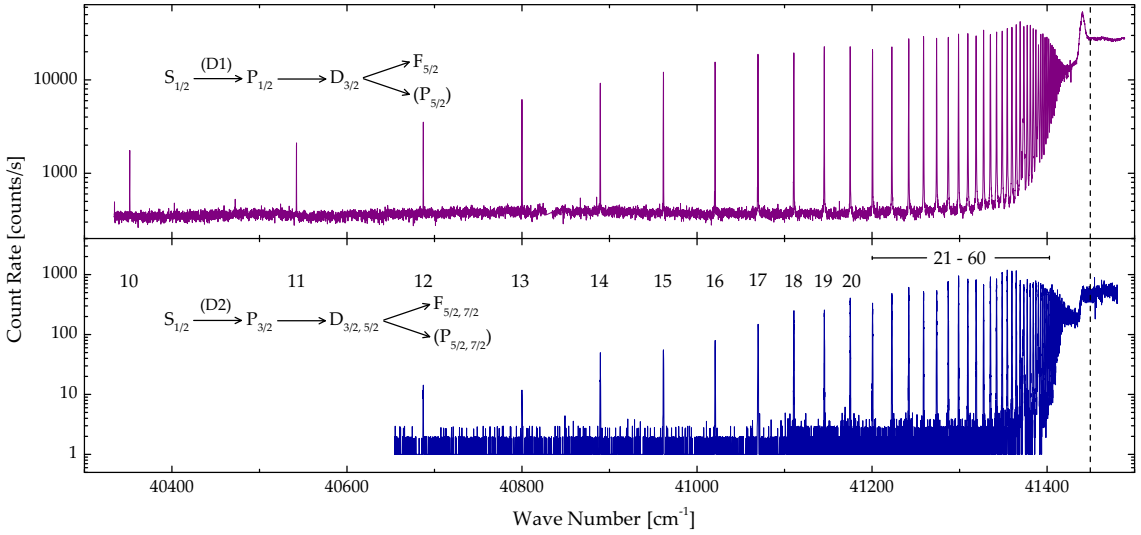

FIG. 4. Two examples of frequency scans of the third step for sodium resonance ionization via the D_1 transition (upper graph) and the D_2 transition (lower graph) as the first step. The excitation scheme and the principal quantum numbers of the determined states are indicated. It should be mentioned that the significant difference in the count rates of the two scans is due to variations in experimental conditions, i.e., settings of the ion optics, and not related to individual transition strengths.

the ionization potential of $E_{\mathrm{IP}}^{\mathrm{lit}} = 41449.451(2)\,\mathrm{cm}^{-1}$ [7,8]. A range of $E_{\mathrm{start}} \approx 40300\,\mathrm{cm}^{-1}$ to $E_{\mathrm{end}} \approx 41500\,\mathrm{cm}^{-1}$ of overall excitation energy was used in the case of the excitation via the D_1 and a slightly narrower range for the D_2 transition. Figure 4 shows representative scans for both schemes in logarithmic scale, where the investigated Rydberg states are numbered according to their principal quantum numbers and $E_{\mathrm{IP}}^{\mathrm{lit}}$ is marked with a dashed line.

We identified Rydberg states of the f series with principal quantum numbers from $n = 10$ to $n = 60$ for the excitation via D_1 and from $n = 12$ to $n = 59$ for the excitation via D_2. Only peaks of one Rydberg series, i.e., belonging to the unresolved $nf\ ^2F^o_{5/2,7/2}$, is visible. This is due to the very low transition strengths into the p series, which is three to four orders of magnitude lower than that into the f states according to [16]. The peaks in Fig. 4 show typical linewidths of $15 - 24$ GHz, which are slightly lower than the linewidth obtained in the frequency scans in Fig. 3 due to the avoidance of strong oversaturation in any of the three consecutive excitation steps during these measurements.

Several scans, upward and downward in energy, were averaged for both excitation schemes. The energy positions found with excitation via both the D_1 line and D_2 line are in a good agreement and perfectly overlap within the statistical error bars. It should be mentioned that the measured deviation for the first ten levels is with $0.09\,\mathrm{cm}^{-1}$ in average larger than for the rest of the levels with a deviation of only $0.03\,\mathrm{cm}^{-1}$ in average. This is due to the count rate, which was in the D_2 scan very low for the first ten peaks. This results in very few data points in each of those peaks, which occasionally led to a shifted energy position in the fit. The fitted and error weighted average energy positions for each Rydberg peak are listed together with the available high-precision literature data from [13] and the most recent data from [9] in Table I. This table also gives the quantum defects calculated with Eqs. (10) and (11) for each Rydberg level.

The statistical error of each level energy consists of the statistical readout error of the wave meter, the uncertainty of the fitted position and a very small error, which accounts for the correction of systematical shifts in wave numbers by the data acquisition system when scanning upward or downward. A systematic error of $0.007\,\mathrm{cm}^{-1}$, which is the $1\ \sigma$ absolute accuracy of the wavelength meter (High Finesse WS6-600), was added afterward to each value. This systematic shift is only applied once, because for the first and second excitation step the literature values, not the herein measured ones, were used for calculation of the total energy. The data in Table I are in perfect agreement with the earlier literature values for nine lower lying levels but slightly disagree for the two cases of $n = 15$ and $n = 19$. The minor discrepancies of 0.05 and $0.03\,\mathrm{cm}^{-1}$, respectively, are well below the uncertainty of the recent measurement of [9] and only slightly exceed the statistical uncertainty of our data, while being covered by the total error. It is thus ascribed to the fact that the literature values from $n = 15$ to $n = 20$ are not measured but calculated using interpolation. Further details of this approach are given in [17], which is the reference quoted in [13]. The data used for the interpolation was taken from [18,19]. Possibly the uncertainties given therein were also somewhat underestimated. In addition, we considered shifts caused by the Autler-Townes effect (ac Stark effect) [20] to be responsible for deviating level energies. In multistep resonance ionization, highly intense light fields can cause a broadening and a splitting of energy levels in the range of several GHz [21]. If the frequencies of the exiting lasers are furthermore detuned regarding the resonance frequencies, an asymmetry of the split structure can occur. In our case, none of the measured peaks are apparently broadened or split which is ascribed to relatively low laser intensities in the interaction region in comparison to those in [21]. Moreover, we set the lasers always at the resonance frequencies, so that only a symmetrical splitting could occur, which would not shift the

TABLE I. Energetic positions (in cm^{-1}) and quantum defects of the measured Rydberg levels of the f series together with literature values from [13,9]. The values marked with ^{*a} were used as bandheads for the Rydberg-Ritz fitting routine, those marked with ^{*b} were only interpolated according to [17].

Configuration	Ref. [13]	Ref. [9]	Weighted average	Quantum defect $\delta(n)$
$2p^6 4f$	34586.92(2)^{*a}			
$2p^6 5f$	37057.65(2)^{*a}			
$2p^6 6f$	38399.79(2)^{*a}			
$2p^6 7f$	39208.98(2)^{*a}			
$2p^6 8f$	39734.16(2)^{*a}			
$2p^6 9f$	40094.19(2)^{*a}			
$2p^6 10f$	40351.761(2)		40351.751(21)$_{stat}$(7)$_{sys}$	0.0016(1)
$2p^6 11f$	40542.293(2)		40542.293(21)$_{stat}$(7)$_{sys}$	0.0016(1)
$2p^6 12f$	40687.203(2)	40687.19(20)	40687.193(26)$_{stat}$(7)$_{sys}$	0.0017(2)
$2p^6 13f$	40799.974(2)	40799.92(20)	40799.964(26)$_{stat}$(7)$_{sys}$	0.0017(2)
$2p^6 14f$	40889.452(2)	40889.39(20)	40889.438(26)$_{stat}$(7)$_{sys}$	0.0018(3)
$2p^6 15f$	40961.637(2)^{*b}	40961.52(20)	40961.588(26)$_{stat}$(7)$_{sys}$	0.0024(3)
$2p^6 16f$	41020.714(2)^{*b}	41020.69(20)	41020.707(26)$_{stat}$(7)$_{sys}$	0.0018(4)
$2p^6 17f$	41069.674(2)^{*b}	41069.62(20)	41069.662(26)$_{stat}$(7)$_{sys}$	0.0019(5)
$2p^6 18f$	41110.703(2)^{*b}	41110.65(20)	41110.692(15)$_{stat}$(7)$_{sys}$	0.0020(4)
$2p^6 19f$	41145.425(2)^{*b}	41145.44(20)	41145.454(15)$_{stat}$(7)$_{sys}$	0.0008(5)
$2p^6 20f$	41175.070(2)^{*b}	41174.98(20)	41175.067(15)$_{stat}$(7)$_{sys}$	0.0019(6)
$2p^6 21f$		41200.56(20)	41200.576(15)$_{stat}$(7)$_{sys}$	0.0020(6)
$2p^6 22f$		41222.59(20)	41222.669(15)$_{stat}$(7)$_{sys}$	0.0030(7)
$2p^6 23f$		41241.95(20)	41241.980(15)$_{stat}$(7)$_{sys}$	0.0021(8)
$2p^6 24f$		41258.89(20)	41258.912(15)$_{stat}$(7)$_{sys}$	0.0020(10)
$2p^6 25f$		41273.80(20)	41273.825(15)$_{stat}$(7)$_{sys}$	0.0039(11)
$2p^6 26f$		41286.91(20)	41287.083(15)$_{stat}$(7)$_{sys}$	0.0034(12)
$2p^6 27f$		41298.76(20)	41298.880(15)$_{stat}$(7)$_{sys}$	0.0043(14)
$2p^6 28f$		41309.40(20)	41309.473(15)$_{stat}$(7)$_{sys}$	0.0015(15)
$2p^6 29f$		41318.89(20)	41318.919(15)$_{stat}$(7)$_{sys}$	0.0061(17)
$2p^6 30f$		41327.41(20)	41327.512(15)$_{stat}$(7)$_{sys}$	0.0020(19)
$2p^6 31f$		41335.14(20)	41335.246(15)$_{stat}$(7)$_{sys}$	0.0029(21)
$2p^6 32f$		41342.20(20)	41342.283(15)$_{stat}$(7)$_{sys}$	0.0015(23)
$2p^6 33f$		41348.67(20)	41348.682(15)$_{stat}$(7)$_{sys}$	0.0011(25)
$2p^6 34f$		41354.48(20)	41354.507(15)$_{stat}$(7)$_{sys}$	0.0040(27)
$2p^6 35f$		41359.77(20)	41359.867(15)$_{stat}$(7)$_{sys}$	0.0018(30)
$2p^6 36f$		41364.71(20)	41364.764(15)$_{stat}$(7)$_{sys}$	0.0041(32)
$2p^6 37f$		41369.22(20)	41369.264(15)$_{stat}$(7)$_{sys}$	0.0080(35)
$2p^6 38f$		41373.43(20)	41373.490(15)$_{stat}$(7)$_{sys}$	−0.0071(38)
$2p^6 39f$		41377.20(20)	41377.332(15)$_{stat}$(7)$_{sys}$	−0.0061(41)
$2p^6 40f$		41380.81(20)	41380.861(15)$_{stat}$(7)$_{sys}$	0.0029(44)
$2p^6 41f$		41384.12(20)	41384.204(15)$_{stat}$(7)$_{sys}$	−0.0088(48)
$2p^6 42f$		41387.16(20)	41387.196(15)$_{stat}$(7)$_{sys}$	0.0174(51)
$2p^6 43f$		41390.06(20)	41390.158(18)$_{stat}$(7)$_{sys}$	−0.0182(65)
$2p^6 44f$		41392.71(20)	41392.813(18)$_{stat}$(7)$_{sys}$	−0.0151(70)
$2p^6 45f$		41395.22(20)	41395.280(18)$_{stat}$(7)$_{sys}$	−0.0060(75)
$2p^6 46f$		41397.53(20)	41397.615(18)$_{stat}$(7)$_{sys}$	−0.0082(80)
$2p^6 47f$		41399.71(20)	41399.788(18)$_{stat}$(7)$_{sys}$	−0.0042(85)
$2p^6 48f$		41401.75(20)	41401.831(18)$_{stat}$(7)$_{sys}$	−0.0019(91)
$2p^6 49f$		41403.66(20)	41403.763(18)$_{stat}$(7)$_{sys}$	−0.0061(97)
$2p^6 50f$		41405.47(20)	41405.577(18)$_{stat}$(7)$_{sys}$	−0.0090(103)
$2p^6 51f$		41407.18(20)	41407.253(18)$_{stat}$(7)$_{sys}$	0.0082(109)
$2p^6 52f$			41408.912(18)$_{stat}$(7)$_{sys}$	−0.0248(115)
$2p^6 53f$			41410.417(18)$_{stat}$(7)$_{sys}$	−0.0182(122)
$2p^6 54f$			41411.821(18)$_{stat}$(7)$_{sys}$	0.0019(129)
$2p^6 55f$			41413.189(18)$_{stat}$(7)$_{sys}$	−0.0075(137)
$2p^6 56f$			41414.495(18)$_{stat}$(7)$_{sys}$	−0.0254(144)

TABLE I. (*Continued.*)

Configuration	Ref. [13]	Ref. [9]	Weighted average	Quantum defect $\delta(n)$
$2p^6 57f$			$41415.675(18)_{stat}(7)_{sys}$	0.0049(152)
$2p^6 58f$			$41416.859(18)_{stat}(7)_{sys}$	−0.0209(160)
$2p^6 59f$			$41417.944(18)_{stat}(7)_{sys}$	−0.0112(169)
$2p^6 60f$			$41418.982(25)_{stat}(7)_{sys}$	−0.0118(248)

center of the symmetrical fit function applied to the observed data.

To extract the ionization potential from the energy positions, the Rydberg-Ritz formula

$$E(n) = E_{IP} - R_M \frac{1}{n^{*2}}, \tag{10}$$

with the reduced-mass Rydberg constant R_M and the effective quantum number n^* as given by the principal quantum number n and the Ritz expansion of the quantum defect $\delta(n)$ in second order

$$n^* = n - \delta(n) = n - \left(A + B\frac{1}{(n-A)^2}\right), \tag{11}$$

was fitted to the data points as shown in Fig. 5. This graph, with residuals well below $0.05\,cm^{-1}$, is a representative plot for the different fits, which were also performed individually for the series with excitation via D_1 and D_2, respectively.

Since the peak positions for lower principal quantum numbers could not be measured experimentally in this work, we included the literature values for $n = 4$ to $n = 9$ as bandheads for the fit. This enables a better convergence of the fit, especially regarding the uncertainties of the A and B parameters of the Rydberg-Ritz expansion.

The fit parameters and their uncertainties are given individually for both excitation schemes in Table II. For comparison also the parameters for a fit ignoring the bandheads are included. The variation in the IP values between the two approaches for analysis are truly minor and do not significantly exceed the statistical error bars, while the much lower precision in the A and particularly the B parameters is obvious when omitting the bandheads. The corresponding distortion in the Rydberg-Ritz function even accidentally compensates for the slight discrepancy of $0.023\,cm^{-1}$ obtained between the two excitation schemes by inclusion of the data from [13]. Nevertheless, for both series, via D_1 and D_2, the energy of the average IP value matches the literature value of $E_{IP}^{lit} = 41449.451(2)\,cm^{-1}$ perfectly even within the statistical uncertainties. The trend of the values indicates the possibility that they are systematically shifted by about $\pm 0.007\,cm^{-1}$, which fully confirms the quoted uncertainty of our measurement. Correspondingly, we give the average of both measurements obtained with the inclusion of bandheads as our final value for the first ionization potential of sodium:

$$E_{IP} = 41449.455(6)_{stat}(7)_{sys}\ cm^{-1}.$$

This value is in good agreement with the literature value. The statistical uncertainty given accounts for the fit error which covers all errors in the energy positions of the experimental peaks addressed by the fit. On top of that a systematic error was added as discussed before.

Figure 6 shows the quantum defects for the f series in dependence of the effective quantum number n^*. Similar to that visible in the residuals of Fig. 5, in Fig. 6 minor irregularities are observed in the range of $38 \leqslant n \leqslant 44$. In that range an underlying peak structure which is also well visible in the base line of Fig. 4 but could not be identified, seemingly affects the peak positions and the fitting procedure. The situation is shown in detail in the magnification given in Fig. 7. Nevertheless, the additional peaks observed around $n = 38$ and $n = 43$ have no significant influence on the fit results for the IP.

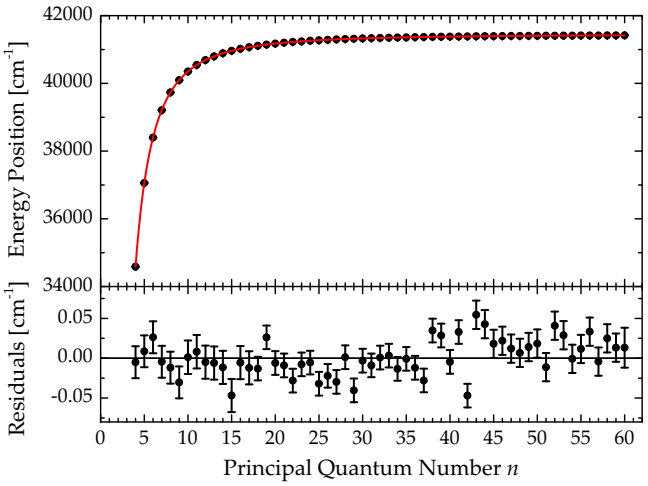

FIG. 5. Energy positions of the Rydberg peaks in dependence of the principal quantum number. The Rydberg-Ritz formula was fitted to the data (red curve). The resulting residuals are given in the lower graph.

TABLE II. Fit parameters for the Rydberg-Ritz fits of the different series. The literature value is from [7,8].

		With bandheads	Without bandheads
D_1	E_{IP} [cm^{-1}]	$41449.443(5)_{stat}(7)_{sys}$	$41449.456(6)_{stat}(7)_{sys}$
	A	0.00169(3)	0.0030(4)
	B	−0.0079(6)	−0.153(45)
D_2	E_{IP} [cm^{-1}]	$41449.466(3)_{stat}(7)_{sys}$	$41449.463(6)_{stat}(7)_{sys}$
	A	0.00172(2)	0.0011(9)
	B	−0.0083(3)	−0.068(240)
Avg.	E_{IP} [cm^{-1}]	$41449.455(6)_{stat}(7)_{sys}$	$41449.460(8)_{stat}(7)_{sys}$
Lit.	E_{IP} [cm^{-1}]	41449.451(2)	

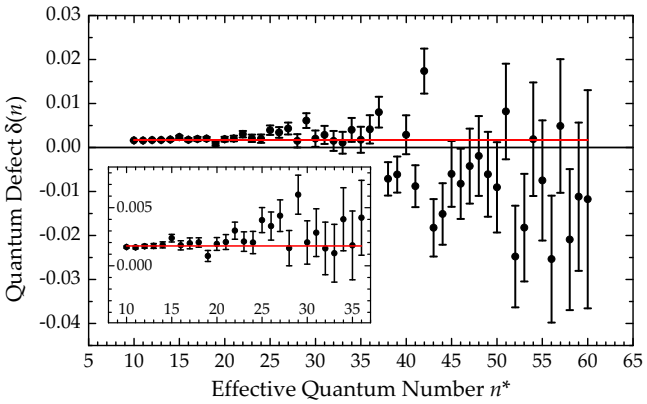

FIG. 6. Quantum defects of the Rydberg levels of the f series measured. The defects were calculated from the measured IP and the energy positions of the resonances. The red curve shows the error weighted average for the quantum defect of $\bar{\delta}(n) = 0.0017(1)$.

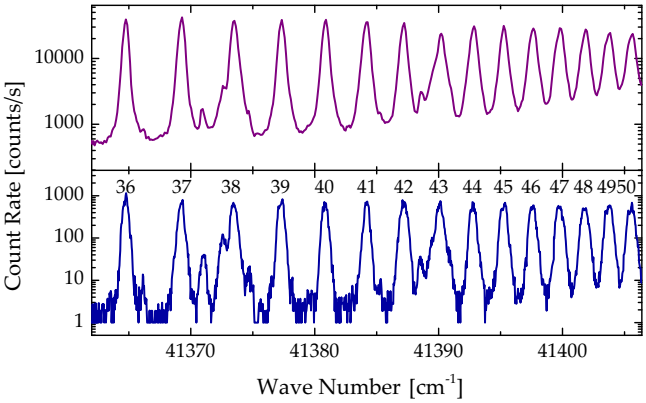

FIG. 7. Enlarged view of the wide range scans in Fig. 4 from $n = 36$ to $n = 50$. In this region an underlying peak structure slightly affects the energy positions of the Rydberg peaks. Excitation in the upper graph via D_1, in the lower via D_2.

IV. CONCLUSION AND OUTLOOK

A. Difference frequency generation

We showed that a laser system based upon the Mainz Ti:sapphire lasers including a DFG stage is ready for midresolution atomic spectroscopy on excitation schemes and high-lying atomic levels and is particularly well suited for operation in the frame of laser ion sources of on-line RIB facilities. Although the present output power of the DFG stage of only about 10 mW is already suitable for reasonably strong first-step transitions, it is still possible to increase this value with simple methods as discussed above, e.g., by involving intracavity frequency doubling for generation of the DFG pump wave. For optimum performance of such a system suitable mixing crystals must be used to deliver a truly significant gain in output power and beam profile. In addition the bandwidth can be lowered to about 50 MHz by using more narrow-band linewidth laser radiation for the fundamental and the frequency-doubled input lasers for DFG. Additionally, this will result in a higher spectral power density and therefore increase the output power.

B. Rydberg spectroscopy of sodium

Using the DFG system discussed above, we performed spectroscopic measurements on the odd-parity Rydberg series $nf\ ^2F^o_{5/2,7/2}$ of sodium. By three-step resonance ionization using excitation schemes via the well-known D_1 and D_2 lines of sodium, we determined the energetic position of 41 high-lying Rydberg states with a high precision of about $0.03\,\mathrm{cm}^{-1}$. We confirmed the already precisely measured first ionization potential of sodium with a precision of $0.02\,\mathrm{cm}^{-1}$ in order to demonstrate the accuracy of our system and the spectroscopic method of in-source multistep resonance ionization spectroscopy, which is becoming more and more popular at on-line laser ion sources.

A minor, so far unexplained finding is the appearance of unexpected humps in the count rate, seen particularly well pronounced in the third step scans in Fig. 4 at approximately $41440\,\mathrm{cm}^{-1}$, just very shortly below the IP. This hump appears in all recorded scans, but has not been observed in other spectroscopic measurement of any of the various elements studied by Ti:sapphire laser resonance ionization so far. It appears sometimes more or less pronounced, which might be ascribed to the conditions of the extraction field being responsible for additional ionization slightly below the IP. This aspect will be investigated systematically in the near future.

ACKNOWLEDGMENTS

J.M.-S. thanks the German Academic Exchange Service (DAAD) for support in the framework of the IAESTE program. P.N. gratefully thanks the Carl Zeiss Stiftung for financial support.

[1] Y. B. Band, C. Radzewicz, and J. S. Krasinski, Phys. Rev. A **49**, 517 (1994).
[2] D. Georgiev, V. P. Gapontsev, A. G. Dronov, M. Y. Vyatkin, A. B. Rulkov, S. V. Popov, and J. R. Taylor, Opt. Express **13**, 6772 (2005).
[3] J. C. Bienfang, C. A. Denman, B. W. Grime, P. D. Hillman, G. T. Moore, and J. M. Telle, Opt. Lett. **28**, 2219 (2003).
[4] W. R. Bosenberg, W. S. Pelouch, and C. L. Tang, Appl. Phys. Lett. **55**, 1952 (1989).
[5] T. W. Hänsch, Appl. Opt. **11**, 895 (1972).
[6] V. Sonnenschein, I. D. Moore, I. Pohjalainen, M. Reponen, S. Rothe, and K. Wendt, JPS Conf. Proc. **6**, 030126 (2015).
[7] M. Ciocca, C. E. Burkhardt, J. J. Leventhal, and T. Bergeman, Phys. Rev. A **45**, 4720 (1992).
[8] J. F. Baugh, C. E. Burkhardt, J. J. Leventhal, and T. Bergeman, Phys. Rev. A **58**, 1585 (1998).
[9] A. Nadeem, M. Shah, S. Shahzada, M. Ahmed, and S. U. Haq, J. Appl. Spectrosc. **82**, 719 (2015).
[10] S. Rothe, B. A. Marsh, C. Mattolat, V. N. Fedosseev, and K. Wendt, J. Phys.: Conf. Ser. **312**, 052020 (2011).

[11] A. Teigelhöfer, P. Bricault, O. Chachkova, M. Gillner, J. Lassen, J. P. Lavoie, R. Li, J. Meiner, W. Neu, and K. D. A. Wendt, Hyperfine Interact. **196**, 161 (2010).
[12] A. V. Smith, Proc. SPIE **4972**, 50 (2003).
[13] J. E. Sansonetti, J. Phys. Chem. Ref. Data **37**, 1659 (2008).
[14] J. J. Olivero and R. L. Longbothum, J. Quant. Spectrosc. Radiat. Transfer **17**, 233 (1977).
[15] C. W. Oates, K. R. Vogel, and J. L. Hall, Phys. Rev. Lett. **76**, 2866 (1996).
[16] *NIST Atomic Spectra Database*, URL http://physics.nist.gov/PhysRefData/ASD/lines_form.html (2015).
[17] S. Dyubko, V. Efremov, S. Podnos, X. Sun, and K. B. MacAdam, J. Phys. B **30**, 2345 (1997).
[18] X. Sun and K. B. MacAdam, Phys. Rev. A **49**, 2453 (1994).
[19] N. H. Tran, H. B. van Linden vanden Heuvell, R. Kachru, and T. F. Gallagher, Phys. Rev. A **30**, 2097 (1984).
[20] S. H. Autler and C. H. Townes, Phys. Rev. **100**, 703 (1955).
[21] S. E. Moody and M. Lambropoulos, Phys. Rev. A **15**, 1497 (1977).

2.4 Collaborative activity

Atomic and nuclear properties of exotic radioisotopes at the borderline of stability are of major interest for several important research fields, e.g. research on nucleosynthesis, nuclear structre and nuclear stability of matter and is therewith associated with the initial formation of matter in the early universe. To gain information on ground state configurations and the composition of rare short-lived nuclei far off stability, it is crucial to produce such species on-line at radioactive ion beam (RIB) facilities. The majority of RIB facilities worldwide utilizes the RIS technique either as ion source or for laser mass spectrometric measurements itself, see cf. [8, 9]. The Mainz LARISSA group is involved in several collaborations on corresponding experiments, for example RILIS [25] and CRIS [26] at ISOLDE (CERN, Switzerland), GISELE [27] at SPIRAL2/S3 (GANIL, France), TRILIS [28] at ISAC (TRIUMF, Canada), IGISOL [29] (JYFL, Finland), PALIS [30] at RIBF (RIKEN, Japan) or LISOL [31] (CRC, Belgium), which has been shut down recently and will be replaced by the GISELE/S3 activities. The latter one will be presented in detail within the following publication *Developments towards in-gas-jet laser spectroscopy studies of actinium isotopes at LISOL*.

2.5 Publication: Developments towards in-gas-jet laser spectroscopy studies of actinium isotopes at LISOL

This article was published in early 2016 and presents preparatory experiments for several important studies at the LISOL separator in Louvain-La-Neuve (Belgium). It comprises information on the experimental setup and first results on the novel technique of resonant ionization spectroscopy in a supersonic gas jet. The combination of RIS with a supersonic gas jet combines highest spectral resolution with highest efficiencies, two mandatory requirements for studies on rare isotopes, that are commonly regarded as contradictory. This work paved the way for revolutionary studies presented in [32] and [33].

The doctoral candidate co-authors this article for his contributions to the measurement campaign. Specifically, he was one together with T. Kron and S. Reader responsible for setting up and operating the laser system for resonance ionization spectroscopy during the measurement campaign at the RIB facility in Louvain-La-Neuve.

Nuclear Instruments and Methods in Physics Research B 376 (2016) 382–387

Contents lists available at ScienceDirect

Nuclear Instruments and Methods in Physics Research B

journal homepage: www.elsevier.com/locate/nimb

Developments towards in-gas-jet laser spectroscopy studies of actinium isotopes at LISOL

S. Raeder [a,b,c,*], B. Bastin [d], M. Block [b,c,f], P. Creemers [a], P. Delahaye [d], R. Ferrer [a], X. Fléchard [e], S. Franchoo [g], L. Ghys [a,l], L.P. Gaffney [a,1], C. Granados [a], R. Heinke [h], L. Hijazi [d], M. Huyse [a], T. Kron [h], Yu. Kudryavtsev [a], M. Laatiaoui [b,c], N. Lecesne [d], F. Luton [d], I.D. Moore [i], Y. Martinez [a], E. Mogilevskiy [a,j], P. Naubereit [h], J. Piot [d], S. Rothe [k], H. Savajols [d], S. Sels [a], V. Sonnenschein [i], E. Traykov [d], C. Van Beveren [a], P. Van den Bergh [a], P. Van Duppen [a], K. Wendt [h], A. Zadvornaya [a]

[a] KU Leuven, Instituut voor Kern- en Stralingsfysica, Celestijnenlaan 200D, B-3001 Leuven, Belgium
[b] Helmholtz-Institut Mainz, 55128 Mainz, Germany
[c] GSI Helmholtzzentrum für Schwerionenforschung GmbH, Planckstraße 1, 64291 Darmstadt, Germany
[d] GANIL, CEA/DSM-CNRS/IN2P3, B.P. 55027, 14076 Caen, France
[e] LPC Caen, ENSICAEN, Université de Caen, CNRS/IN2P3, Caen, France
[f] Institut für Kernchemie, Johannes Gutenberg Universität, 55128 Mainz, Germany
[g] Institute de Physique Nucléaire (IPN) d'Orsay, 91406 Orsay, Cedex, France
[h] Institut für Physik, Johannes Gutenberg Universität, 55128 Mainz, Germany
[i] Department of Physics, University of Jyväskylä, P.O. Box 35 (YFL), Jyväskylä, FI40014, Finland
[j] Faculty of Mechanics and Mathematics, Lomonosov Moscow State University, Leninskie gory, 1, 119992 Moscow, Russia
[k] CERN, CH-1211 Genève, Switzerland
[l] SCK-CEN, Belgian Nuclear Research Center, Boeretang 200, 2400 Mol, Belgium

ARTICLE INFO

Article history:
Received 6 September 2015
Received in revised form 20 November 2015
Accepted 10 December 2015
Available online 4 February 2016

Keywords:
Resonance ionization spectroscopy
Gas cell
Gas jet
Actinium

ABSTRACT

To study exotic nuclides at the borders of stability with laser ionization and spectroscopy techniques, highest efficiencies in combination with a high spectral resolution are required. These usually opposing requirements are reconciled by applying the in-gas-laser ionization and spectroscopy (IGLIS) technique in the supersonic gas jet produced by a de Laval nozzle installed at the exit of the stopping gas cell. Carrying out laser ionization in the low-temperature and low density supersonic gas jet eliminates pressure broadening, which will significantly improve the spectral resolution. This article presents the required modifications at the Leuven Isotope Separator On-Line (LISOL) facility that are needed for the first on-line studies of in-gas-jet laser spectroscopy. Different geometries for the gas outlet and extraction ion guides have been tested for their performance regarding the acceptance of laser ionized species as well as for their differential pumping capacities. The specifications and performance of the temporarily installed high repetition rate laser system, including a narrow bandwidth injection-locked Ti:sapphire laser, are discussed and first preliminary results on neutron-deficient actinium isotopes are presented indicating the high capability of this novel technique.

1. Introduction

At the Leuven Isotope Separator On-Line (LISOL) facility the in-gas laser ionization and spectroscopy (IGLIS) technique is used to study short-lived nuclides produced in heavy-ion fusion reactions where highly energetic projectiles impinge on thin solid targets. This technique was previously employed within the high-pressure environment of the stopping gas cell to study ground and isomeric state properties of neutron-deficient $^{57-59}$Cu [1] and $^{97-101}$Ag [2] isotopes by resonant laser excitation and ionization. To improve the spectral resolution (typically 4–10 GHz due to pressure broadening) and the selectivity of this technique, off-line studies on resonant ionization in the low-temperature and low-density regime of the supersonic free jet formed at the gas cell exit hole were successfully performed using stable Cu isotopes [3].

* Corresponding author at: GSI Helmholtzzentrum für Schwerionenforschung GmbH, Planckstraße 1, 64291 Darmstadt, Germany.
E-mail address: s.raeder@gsi.de (S. Raeder).
[1] Present address: School of Engineering, University of the West of Scotland, Paisley PA1 2BE, United Kingdom.

http://dx.doi.org/10.1016/j.nimb.2015.12.014
0168-583X/

Here a resolution down to 450 MHz for the 327 nm optical ground state transition in Cu could be demonstrated using pulsed amplification of a cw diode laser an improvement of one order of magnitude compared to in-gas-cell spectroscopy. To explore the full capability of the in-gas-jet ionization technique a new off-line laboratory is being commissioned at KU Leuven [4]. Finally, this technique will be used at the low energy front-end of the S^3 in-flight separator at GANIL [5] to study rare isotopes at the extremes of existence. This technique was now applied for the first time on-line at the LISOL facility to study neutron-deficient actinium isotopes including the semi-magic ^{215}Ac nucleus.

The first attempt to perform resonant laser ionization in the gas cell on actinium isotopes was reported in [5]. This research was motivated by studying the evolution of the $N = 126$ shell closure towards heavier Z systems by investigating electrical quadrupole and magnetic dipole moments, as well as by the investigation on shape effects occurring in this region of the nuclear chart through the observation of changes in charge radii. Complementary, neutron-rich actinium isotopes, located in a region with expected octupole deformation [6], are accessible at ISOL facilities [7]. Atomic levels of actinium for resonant excitation are known from the measurements of arc and hollow-cathode spectra using long-lived ^{227}Ac [8,9], while investigations on the first ionization potential (IP) as well as on auto-ionizing (AI) resonance above the first IP have been carried out in a previous work within the collaboration [10]. Additional spectroscopic off-line studies focused on the identification of levels featuring a wide hyperfine structure (HFS) splitting with a suitable transition at 438 nm [11]. Using this transition, the HFS splitting of the neutron deficient actinium isotopes $^{212-215}$Ac was partly resolved in in-gas-cell laser spectroscopic studies at LISOL [12]. Nevertheless, the spectral resolution of about 6 GHz did not allow the extraction of all required parameters with an adequate precision. Especially the information on the spectroscopic quadrupole moment and therefore the nuclear deformation could not be determined.

The in-gas-jet ionization technique overcomes these restrictions and the production rates of actinium isotopes made an on-line application at LISOL feasible. For the investigations on rare isotopes the total efficiency of the method is crucial as the production rates are small. During the previous off-line tests on copper reported in [3] the total efficiency could not be estimated due to the unknown evaporation rate of stable Cu from the filament. However, the duty cycle when using the existing 200 Hz Excimer-pumped dye laser system for ionization in the fast propagating gas jet as well as the large divergence angle of the freely expanding jet limit the potential efficiency. The existing front-end at LISOL furthermore constrained the implementation of this technique limiting the final performance.

This article summarizes the preparation work for the on-line application of the in-gas-jet ionization involving the gas-jet formation, the ion extraction as well as the performance and characteristics of the high-repetition laser system that was installed at the LISOL facility to improve the total performance. The first preliminary results will also be summarized here.

2. Production, ion extraction and interaction region

At LISOL the radioactive isotopes are produced using the fusion reaction from ^{20,22}Ne projectiles (0.16 pμA, 145 MeV) onto a 1 μm thick ^{197}Au target, with production cross sections as low as 1.6 mbarn for ^{212}Ac [5,13]. The target is located inside a gas cell filled with about 500 mbar of argon for thermalization and neutralization of the reaction products. The neutralized products are guided by the gas flow towards the exit nozzle of the gas cell. Remaining charged particles are removed by an electrostatic ion

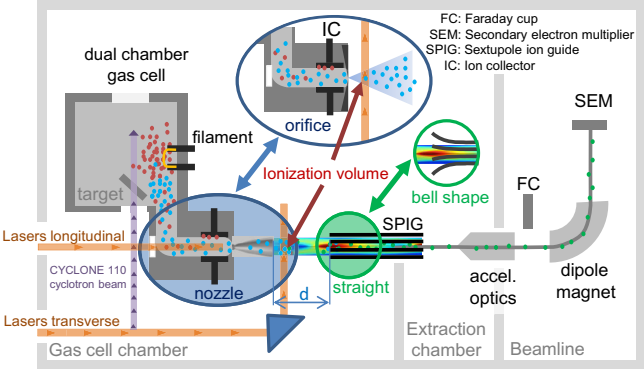

Fig. 1. Schematic diagram of the experimental set-up at LISOL illustrating different options investigated in preparation for the on-line studies. In-gas-cell (longitudinal) and in-gas-jet (transverse) ionization for the off-line (filament) and on-line measurements are indicated. The two options under investigation for the gas cell exit, a free jet from an orifice and a shaped gas jet from a de Laval nozzle are depicted in the blue circled areas. The green circled area indicates the tested SPIG configurations for an enhanced ion capture efficiency. (For interpretation of the references to color in this figure legend, the reader is referred to the web version of this article.)

collector. The neutralized atoms are ionized using resonant laser ionization in a two-step ionization scheme [14] allowing for an improved selectivity in radioactive ion beam (RIB) production [15] as well as for laser spectroscopic investigations.

For the laser ionization in the gas jet a high repetition rate laser system as well as an extended laser-atom ionization region are required for highest efficiencies [3,4]. As the argon jet velocity is about 550 m/s an ionization region of 55 mm length is needed assuming a laser repetition rate of 10 kHz. The schematic setup for the experiment in combination with investigated options is depicted in Fig. 1. Using the dual-chamber gas cell [16] the gas cell chamber and the position of the primary cyclotron beam restrict the distance between gas cell exit and the beginning of the sextupole ion guide (SPIG) to about 22 mm. The SPIG is required for ion extraction and differential pumping between the gas cell chamber and the extraction chamber. To test the capturing efficiency of the photo ions in the gas jet by the SPIG two different options for the gas outlet at the gas cell exit were tested. The standard configuration is a simple orifice with a hole diameter of 0.8 mm, leading to a free expanding gas jet. For in-gas-cell ionization the SPIG is located within a few mm after the orifice to ensure an efficient capturing while a DC gradient is applied to dissociate molecules formed during the ion transport in the gas cell. The second option is a de Laval nozzle with a throat diameter of 1 mm as indicated in the blue encircled areas in Fig. 1. The gas dynamic calculations indicate that the argon boundary layer inside the nozzle limits the effective Mach number of $M \approx 5.5$ and a jet diameter of about 3.5 mm.

Fig. 2 shows the measured extraction efficiency for ions created inside the gas cell and transported to the first Faraday cup (FC) after acceleration as a function of the distance for both options. For these measurements stable Cu isotopes were evaporated from a filament and were ionized inside the gas cell using an Excimer-pumped (LPX 240i, Lambda Physik) dye laser system (Scanmate, Lambda Physik) at a repetition rate of 50 Hz [17]. The extraction efficiency for the free jet clearly drops when the distance d (see Fig. 1) between orifice and SPIG is increased, limiting the effective distance to values below 10 mm. The extraction efficiency for the de Laval nozzle shows a better performance and is constant at the level of about 80% within the range of the possible nozzle – SPIG distance, indicating that the gas jet is more forward directed compared to the free-expanding gas jet from the orifice. In contrast to the low divergence shape of the jet from the de Laval nozzle an

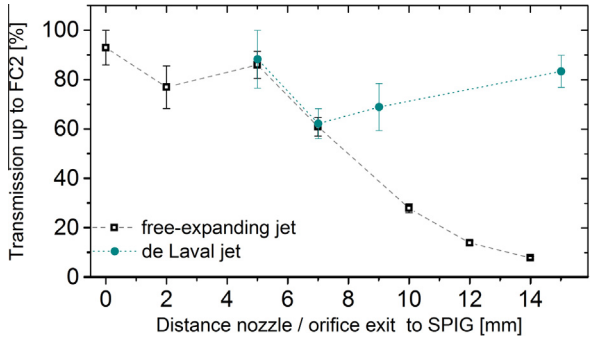

Fig. 2. Dependence of the transmission of in-gas-cell ionized stable Cu isotopes on the distance *d* for the two options of gas jets. The FC signal is referenced to the ion current captured directly onto the SPIG rods. The points are connected to guide the eyes.

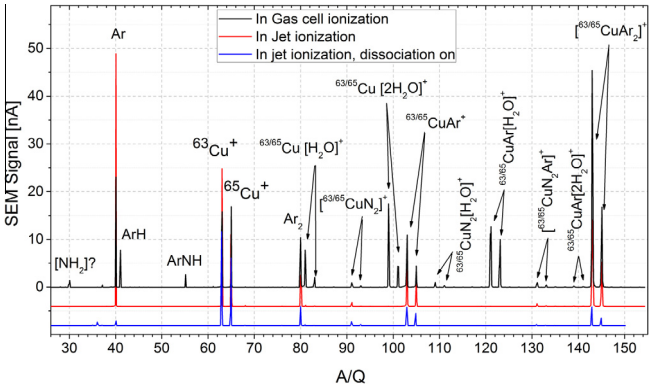

Fig. 3. Mass spectra obtained from in-gas-cell (black curve) and in-gas-jet ionization (red curve) show the molecular formation of Cu ions. The blue curve represents the case of in-gas-jet ionization in combination with a SPIG offset voltage of 300 V for CID. The red and blue curves are shifted for visibility. (For interpretation of the references to color in this figure legend, the reader is referred to the web version of this article.)

opening angle of about 30° was estimated for the free jet in off-line experiments [3]. This conclusion is supported by the observations from the differential pumping capability of the SPIG. In contrast to the orifice, a larger gas cell-SPIG distance is required for the de Laval nozzle in order to maintain a working pressure below $1 \cdot 10^{-4}$ mbar in the extraction chamber when operating the gas cell at the nominal pressure of 350 mbar, which is required to efficiently stop the actinium fusion products. Additionally, the ratio of in-gas-cell to in-gas-jet ionized Cu was determined to estimate the efficiency performance. For a laser beam diameter of 5 mm irradiating the gas jet in a transversal arrangement for both laser beams and laser repetition rate of 100 Hz a ratio of about 1000 is roughly expected from duty cycle and geometrical considerations. For the orifice a ratio of 500 was observed while for the de Laval nozzle a ratio below 200 was repeatedly measured. This exceeds the expectations by a factor of 4–5 which could be explained by a reduction of collisional de-excitation compared to the high pressure environment inside the gas cell. In summary the available de Laval nozzle, although not fully characterized and optimized, showed a superior performance in comparison to the orifice. The length of the diverging part of the de Laval nozzle is 10.5 mm. This limits the effective length of the gas jet determined by the nozzle – SPIG distance to 12 mm in on-line operation, which is still larger than the laser beam diameter of 5 mm realized at the experiment.

A second test was performed in which we investigated the replacement of the straight SPIG with an inner diameter of 3 mm, a rod diameter of 1.5 mm and a length of 126 mm [18] by a bell-shaped SPIG. Here the inner diameter towards the gas cell is increased to about 6 mm which then smoothly reduces to the normal inner diameter of 3 mm. This geometry is sketched in the green encircled area in Fig. 1 and was intended to improve the ion extraction. Due to the larger acceptance area of the SPIG this geometry was found to be less sensitive to the alignment of the gas cell with the de Laval nozzle, while the total performance in extraction efficiency and in-gas-cell to in-gas-jet ionization was comparable to a well aligned normal SPIG geometry. A clear disadvantage precluding the bell-shaped SPIG from further considerations was the reduced differential pumping capability. The pressure exceeded $1 \cdot 10^{-4}$ mbar in the extraction chamber at the nominal gas cell pressure of 350 mbar for all distances, indicating that the gas jet is well captured.

Another study during these tests was to investigate the formation of molecular ions after the laser ionization of copper atoms in the gas jet environment. It is known that the atomic ions created in the gas cell can form molecular ions with impurity molecules present in the buffer gas. Most of these ions can be cracked by collision-induced-dissociation (CID) when applying a sufficient voltage between the gas cell and the SPIG [19]. Fig. 3 shows the mass spectra obtained for in-gas-cell ionization and in-gas-jet ionization and the additional effect of a dissociation voltage for the latter. It is clearly visible that argon clusters and nitrogen compounds are still formed in the gas jet while in the gas cell significant amounts of water compounds can be additionally found. This observation can be explained by the difference in gas pressure and thus in the change in total ion-neutral collision rate which is orders of magnitude reduced in the gas jet environment and will therefore decrease the number of molecular loss channels in comparison to the gas cell. This observation is in agreement with earlier measurements on the time structure of different molecular compounds indicating that the formation of argon clusters has the fastest time scale [20]. Nevertheless the formation of clusters between argon (and possibly nitrogen) and the photo-ions in the low density region of the gas jet is somewhat unexpected and has to be considered in further investigations on the in-gas-jet ionization technique. Applying a voltage of 300 V for the in-jet ionization, most but not all clusters can be dissociated and the abundance of copper ions bound in molecular sidebands is reduced from 46% to 19%. In addition, the time structures of the ions from the different ionization regions have been measured and conform with the results from previous investigations considering in-SPIG ionization [21].

3. Laser system

Efficient and selective laser ionization of short-lived species in the gas jet requires a high-repetition rate laser system, which in addition must include one laser with a narrow bandwidth matching the reduced Doppler broadening in the gas jet to gain in spectral resolution. A high-repetition rate Titanium:sapphire (Ti:Sa) laser system with a broad bandwidth has been installed temporarily at LISOL in 2011 to test the performance for in-gas-cell laser ionization [22]. It was shown that at repetition rates of 10 kHz a similar in-gas-cell ionization efficiency was obtained compared to the Excimer pumped dye laser system operated at 200 Hz but at higher pulse energies.

For the in-gas-jet laser ionization and spectroscopy of the neutron-deficient actinium isotopes a similar solid-state laser system was commissioned at LISOL in a joint collaboration between GANIL [23], Mainz University [24] and University of Jyväskylä [25]. The layout of the laser system is schematically shown in Fig. 4. It consists of a Nd:YAG pump laser (DM-YAG 60-532, Pho-

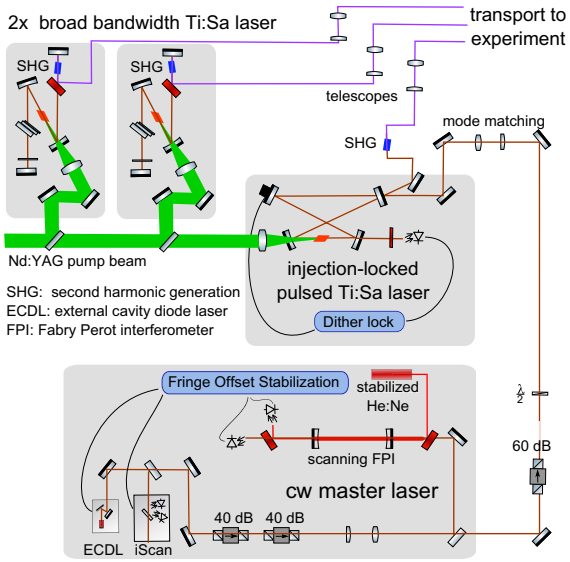

Fig. 4. Schematic setup of the laser system consisting of two broad bandwidth pulsed Ti:Sa lasers and a narrow bandwidth injection-locked Ti:Sa laser. The narrow bandwidth laser is seeded by a cw ECDL as master laser. Additionally, the components for the active stabilization with a He:Ne are shown, see text for details.

tonics Industries Inc.) with an average output power up to 60 W at 532 mn operated at a repetition rate of 10 kHz. This light was used to simultaneously pump three tunable Ti:Sa lasers of which two have a *Z*-shaped resonator featuring a broad bandwidth of about 4 GHz and a pulse length of 35 ns as used for resonant ionization laser ion sources [24]. They can be tuned in the range of 690–990 nm (fundamental output) with extension to shorter wavelength by generation of higher harmonics. One of the lasers is used to excite the 424 nm transition into an AI resonance as shown in the ionization scheme in Fig. 5. The other laser is operated at 438 nm for a broadband first step excitation but also can be operated at 434 nm to increase the ionization efficiency by exciting a second AI transition. As the required laser light is in the blue wavelength region around 430 nm, the broad bandwidth lasers have been operated with intra-cavity second harmonic generation (SHG) [26]. In this method all resonator mirrors are highly reflective for the fundamental laser radiation and the optical nonlinear beta barium borate (BBO) crystal used for SHG is installed inside the cavity. This allows an increase of the conversion efficiency as the cavity enhancement of the fundamental radiation can be efficiently used. The second harmonic is coupled out using a dichroic mirror inside the cavity. This configuration generated up to 1.8 W of laser light in the 430 nm region using a pump power of about 14.5 W.

The third laser, pumped by the same Nd:YAG laser, was a pulsed narrow bandwidth Ti:Sa laser with a bow-tie geometry. This laser was developed and operated off-line [27,11] but so far never used for on-line operation. The cavity was injection-locked by narrow bandwidth light from a cw external cavity diode laser (ECDL) seeding the pulsed laser radiation at 877 nm. A home-built ECDL in Littrow geometry was used with an anti-reflection (AR) coated laser diode (EYP-RWE-0860, Eagleyard Photonics) for an extended scanning range. Frequency stabilization and control was achieved using a fringe-off-set lock technique. A homemade scanning Fabry–Perot Interferometer (sFPI) with a free spectral range (FSR) of 299.979 MHz – referenced to a stabilized He:Ne laser (SL03, SIOS Messtechnik) for relative and stable frequency control – was used in combination with a commercial quadrature interferometer stabilization (iScan, TEM Messtechnik) for short-term stabilization. This provided laser light with a bandwidth of a few MHz which could be scanned over several GHz [28]. To protect the diode laser from back reflections, as well as from the pulsed laser radiation, a total of 140 dB of optical isolation was installed using three optical Faraday isolators. Due to the stabilization, monitoring and protection measures a laser power of only 6 mW, from the original 26 mW measured directly after the diode laser, was available for seeding the pulsed Ti:Sa laser. Nevertheless, this power was sufficient to stabilize the cavity and seed the wavelength of the pulsed Ti:Sa laser. After mode matching, the cw laser light was injected into the bow-tie Ti:Sa ring resonator which itself was stabilized onto the diode laser radiation using a dither lock (LaseLock, TEM Messtechnik). As the fundamental wavelength of 877 nm is relatively far off the Ti:Sa gain maximum around 800 nm, an appropriate mirror set with high reflectivity (HR) coating from 850 to 950 nm was used to suppress self stimulated lasing at wavelengths possessing a higher gain. In total about 1.5 W of fundamental laser radiation with a spectral band width of about 10–20 MHz, which is a typical value for this laser [11], was available resulting in about 80–100 mW at 438 nm after external single pass SHG.

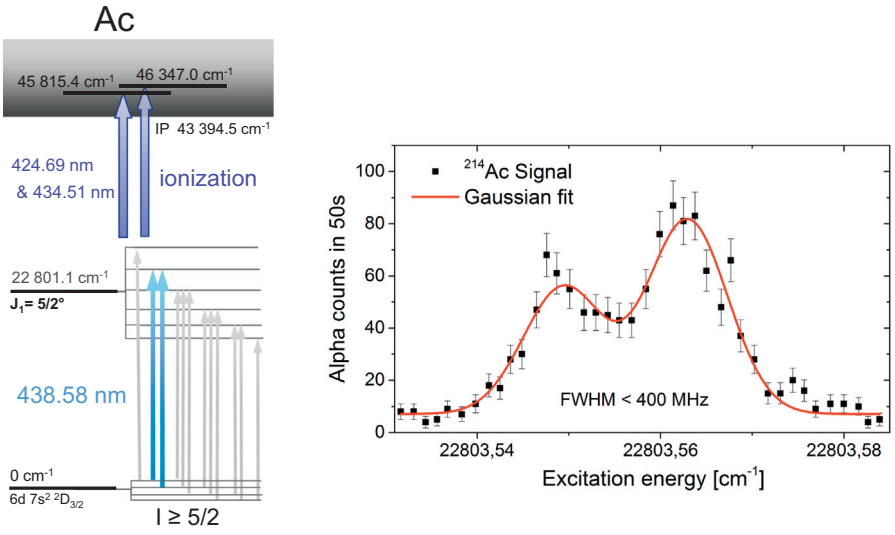

Fig. 5. Left: ionization scheme with a schematic HFS splitting for a nuclear spin $I > 5/2$ as it is the case for ^{214,215}Ac. The transition wavelengths are given in vacuum and the AI states have been identified in a previous work [7]. Right: Observed signal for two partially resolved HFS transitions as indicated in the ionization scheme in ^{214}Ac.

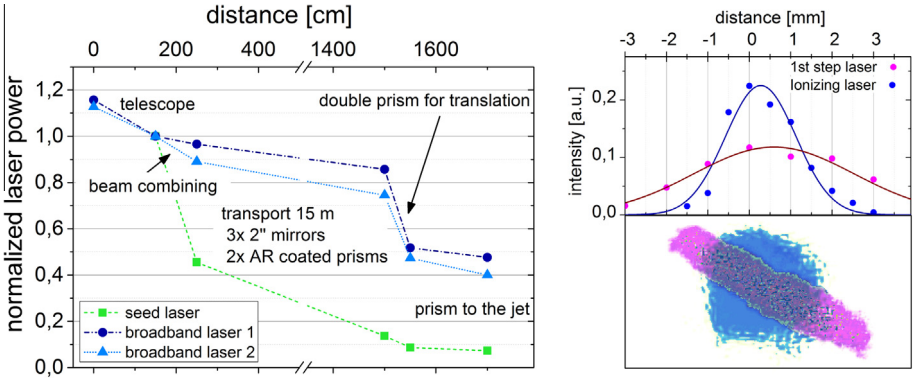

Fig. 6. Left: transmission of the laser radiation through the optical elements up to the ionization volume in dependence of the distance to the front of the focusing telescopes. Right: spot size, shape and orientation of the laser beams at the location of the ionization volume. The ellipticity of the first step is caused by an imperfectly compensated astigmatism from the external SHG, while the orientation is due to the beam transport.

The laser radiation of all three lasers was then shaped using telescopes and guided towards the gas cell located 17 m away from the laser table. For transport 2" high-reflecting dielectric mirrors and anti-reflection coated quartz prisms were used. After the experiment and all corresponding optimization procedures, the transmission of the laser radiation was measured as shown in the left part of Fig. 6. The ionization lasers show a rather steep drop in transmitted power at a distance of around 15 m where a pair of prisms was mounted on a translation stage allowing a remote horizontal tuning of all three lasers simultaneously. Unfortunately, it was set up close to the limit of total internal reflection and optimization during the experiment resulted in additional losses, which have to be taken into account when estimating the efficiency and saturation powers. The first step shows significant losses during laser beam transport which is attributed to the imperfectly compensated astigmatism introduced by the external SHG. As the laser power was more than sufficient for spectroscopy and even additional attenuation of a factor of ten was required, this loss in laser power was not further optimized but the quantification is important for reporting the applied laser pulse energies. The right part of Fig. 6 shows the final laser beam size of the first and second step at the gas jet position, thus defining the ionization volume. The upper graph shows the measured profiles projected in one dimension. The lower picture shows the colored and superimposed photographs of each step, but due to saturation of the camera the pictures serves only as a guide to estimate the size and the shape of the laser beam. The elliptical shape of the first step is due to the insufficient astigmatic compensation and will reduce the effective ionization region further. The beam spot width of about 4 mm is much smaller than the 55 mm required for the illumination of all atoms in the gas jet at a laser repetition rate of 10 kHz. Therefore, a geometrical factor of about 7% has to be considered for the total efficiency.

4. Results and outlook

With the discussed improvements at the gas cell setup and the high-repetition rate laser system it was possible to resonantly ionize on-line produced neutron-deficient actinium isotopes in the gas jet for the first time. Fig. 5 shows a partially resolved spectrum of two HFS transitions observed in ^{214}Ac as indicated in the depicted ionization scheme. The resonances feature a full width half maximum below 400 MHz and the shape is dominated by a Gaussian distribution, which shows that the pressure broadening becomes negligible. In this frequency scan the power of the first step laser was attenuated to 8 mW on the laser table to avoid saturation broadening and corresponds to about 80 nJ pulse energy in the ionization region. The total efficiency of this first on-line use of the in-gas-jet technique seems to follow the trend observed in the off-line tests. An evaluation of the efficiency as well as of the spectroscopic results is ongoing.

Acknowledgments

This work was supported by FWO-Vlaanderen (Belgium), by GOA/2010/010 (BOF KU Leuven), by the IAP Belgian Science Policy (BriX network P7/12) and by a Grant from the European Research Council (ERC-2011-AdG-291561-HELIOS). S.S acknowledges a Ph. D. Grant of the belgian Agency for Innovation by Science and Technology (IWT). L.P.G. acknowledges FWO-Vlaanderen (Belgium) as an FWO Pegasus Marie Curie Fellow.

References

[1] T. Cocolios, A. Andreyev, B. Bastin, N. Bree, J. Büscher, J. Elseviers, J. Gentens, M. Huyse, Yu. Kudryavtsev, D. Pauwels, et al., Phys. Rev. Lett. 103 (2009) 102501, http://dx.doi.org/10.1103/PhysRevLett. 103.102501.
[2] R. Ferrer, N. Bree, T. Cocolios, I. Darby, H. De Witte, W. Dexters, J. Diriken, J. Elseviers, S. Franchoo, M. Huyse, et al., Phys. Lett. B 728 (2014) 191–197, http://dx.doi.org/10.1016/j.physletb.2013.11.055.
[3] Yu. Kudryavtsev, R. Ferrer, M. Huyse, P. Van den Bergh, P. Van Duppen, Nucl. Instr. Meth. B 297 (2012) 7–22, http://dx.doi.org/10.1016/j.nimb.2012.12.008.
[4] Yu. Kudryavtsev, P. Creemers, R. Ferrer, C. Granados, L. Gaffney, M. Huyse, E. Mogilevskiy, S. Raeder, S. Sels, P. Van den Bergh, P. Van Duppen, A. Zadvornaya, Nucl. Instr. Meth. B 376 (2016) 345–352.
[5] R. Ferrer, B. Bastin, D. Boilley, P. Creemers, P. Delahaye, E. Liénard, X. Fléchard, S. Franchoo, L. Ghys, M. Huyse, et al., Nucl. Instr. Meth. B 317 (2013) 570–581, http://dx.doi.org/10.1016/j.nimb.2013.07.028.
[6] I. Ahmad, P. Butler, Annu. Rev. Nucl. Part. Sci. 43 (1993) 71–116, http://dx.doi.org/10.1146/annurev.ns.43.120193.000443.
[7] S. Raeder, M. Dombsky, H. Heggen, J. Lassen, T. Quenzel, M. Södin, A. Teigelhöfer, K. Wendt, Hyperfine Interact. 216 (2013) 33–39, http://dx.doi.org/10.1007/s10751-013-0832-7.
[8] W. Meggers, Spectrochim. Acta 10 (1957) 195–200, http://dx.doi.org/10.1016/0371-1951(57)80186-6.
[9] W. Meggers, M. Fred, F. Tomkins, J. Res. Natl. Bur. Stand. 58 (1957) 297–315, http://dx.doi.org/10.6028/jres.058.037.
[10] J. Roßnagel, S. Raeder, A. Hakimi, R. Ferrer, N. Trautmann, K. Wendt, Phys. Rev. A 85 (2012) 012525, http://dx.doi.org/10.1103/PhysRevA.85.012525.
[11] V. Sonnenschein, Laser developments and high resolution resonance ionization spectroscopy of actinide elements (Ph.d. thesis), Jyväskylä, 2014. ISBN 978-951-39-6050-6.
[12] C. Granados, et al. (2015), in preparation.
[13] A. Andreyev, D. Bogdanov, V. Chepigin, A. Kabachenko, O. Malyshev, Y.A. Muzychka, B. Pustylnik, G. Ter-Akopian, A. Yeremin, Nucl. Phys. A 568 (1994) 323–332, http://dx.doi.org/10.1016/0375-9474(94)90205-4.
[14] Yu. Kudryavtsev, R. Ferrer, M. Huyse, P. Van den Bergh, P. Van Duppen, L. Vermeeren, Rev. Sci. Instrum. 85 (2013) 02B915, http://dx.doi.org/10.1063/1.4850695.
[15] L. Vermeeren, N. Bijnens, M. Huyse, Yu. Kudryavtsev, P. Van Duppen, J. Wauters, Z. Qamhieh, P. Thoen, E. Vandeweert, R. Silverans, Phys. Rev. Lett. 73 (1994) 1935, http://dx.doi.org/10.1103/PhysRevLett. 73.1935.

[16] Yu. Kudryavtsev, T.E. Cocolios, J. Gentens, M. Huyse, O. Ivanov, D. Pauwels, T. Sonoda, P. Van den Bergh, P. Van Duppen, Nucl. Instr. Meth. B 267 (2009) 2908–2917, http://dx.doi.org/10.1016/j.nimb.2009.06.013.
[17] Yu. Kudryavtsev, B. Bruyneel, S. Franchoo, M. Huyse, J. Gentens, K. Kruglov, W. Mueller, N. Prasad, R. Raabe, I. Reusen, et al., Nucl. Phys. A 701 (2002) 465–469, http://dx.doi.org/10.1016/S0375-9474(01)01628-1.
[18] P. Van den Bergh, S. Franchoo, J. Gentens, M. Huyse, Yu. Kudryavtsev, A. Piechaczek, R. Raabe, I. Reusen, P. Van Duppen, L. Vermeeren, A. Wöhr, Nucl. Instr. Meth. B 126 (1997) 194–197, http://dx.doi.org/10.1016/S0168-583X(96)01011-7.
[19] Yu. Kudryavtsev, B. Bruyneel, M. Huyse, J. Gentens, P. Van den Bergh, P. Van Duppen, L. Vermeeren, Nucl. Instr. Meth. B 179 (2001) 412–435, http://dx.doi.org/10.1016/S0168-583X(01)00575-4.
[20] Yu. Kudryavtsev, M. Facina, M. Huyse, J. Gentens, P. Van den Bergh, P. Van Duppen, Nucl. Instr. Meth. B 204 (2003) 336–342, http://dx.doi.org/10.1016/S0168-583X(02)01946-8.
[21] T. Sonoda, T. Cocolios, J. Gentens, M. Huyse, O. Ivanov, Yu. Kudryavtsev, D. Pauwels, P. Van den Bergh, P. Van Duppen, Nucl. Instr. Meth. B 267 (2009) 2918–2926, http://dx.doi.org/10.1016/j.nimb.2009.06.085.
[22] R. Ferrer, V. Sonnenschein, B. Bastin, S. Franchoo, M. Huyse, Yu. Kudryavtsev, T. Kron, N. Lecesne, I. Moore, B. Osmond, et al., Nucl. Instr. Meth. B 291 (2012) 29–37, http://dx.doi.org/10.1016/j.nimb.2012.08.023.
[23] N. Lecesne, R. Alves-Conde, E. Coterreau, F. De Oliveira, M. Dubois, J.L. Flambard, H. Franberg, T. Gottwald, P. Jardin, J. Lassen, F. Le Blanc, R. Leroy, C. Mattolat, A. Olivier, J.Y. Pacquet, A. Pichard, S. Rothe, M.G. Saint-Laurent, K. Wendt, Rev. Sci. Instrum. 81 (2010), http://dx.doi.org/10.1063/1.3279301.
[24] C. Mattolat, S. Rothe, F. Schwellnus, T. Gottwald, S. Raeder, K. Wendt, A.I.P. Conf. Proc. 1104 (2009) 114, http://dx.doi.org/10.1063/1.3115586.
[25] M. Reponen, I.D. Moore, T. Kessler, I. Pohjalainen, S. Rothe, V. Sonnenschein, Eur. Phys. J. A 48 (2012), http://dx.doi.org/10.1140/epja/i2012-12045-2.
[26] V. Sonnenschein, I.D. Moore, I. Pohjalainen, M. Reponen, S. Rothe, K. Wendt, J.P. S. Conf. Proc. 6 (2015) 030126, http://dx.doi.org/10.7566/JPSCP.6.030126.
[27] T. Kessler, H. Tomita, C. Mattolat, S. Raeder, K. Wendt, Laser Phys. 18 (2008) 842–849, http://dx.doi.org/10.1134/S1054660X08070074.
[28] A. Hakimi, Diodenlaserbasierte Resonanzionisations-Massenspektrometrie zur Spektroskopie und Ultraspurenanalyse an Uranisotopen (Ph.d. thesis), Mainz, 2014. URN: urn:nbn:de:hebis:77–35106.

Chapter 3

Spectroscopy of the protactinium atom

As central research topic and experimentally as well as theoretically very challenging main objective of this work, resonance ionization of the protactinium atom was addressed. The spectroscopy forms the basis for all following analytic chapters within this work. A lot of preparatory work as exemplarily presented in the previous publications was needed to cope with this task. To become familiar with the in many regards very specific element ^{91}Pa, the next section introduces the element including the history of its discovery, some of its properties, the efforts needed for its extraction and chemical separation and the first attempts for laser spectroscopic investigation in general as well as to measure the first ionization potential. The publication *Excited atomic energy levels in protactinium by resonance ionization spectroscopy* at the end of this chapter provides a detailed view on the spectroscopic work on protactinium in the frame of the present work, including the extraction of many hundreds of high-lying energy levels and tedious approaches for their identification and separation.

3.1 The element 91

The knowledge today on protactinium is comprised in a chapter within a book on the actinide and transactinide elements, from which the following quotation sums it up in a nutshell:

"Protactinium, element 91, is one of the most rare of the naturally occurring elements and may well be the most difficult of all to extract from natural sources. Protactinium is, formally, the third element of the actinide series and the first having a $5f$ electron. The superconducting properties of protactinium metal provide clear evidence that Pa is a true actinide element [...].
Its chemical behavior in aqueous solution, however, would seem to place it in group VB of the Mendeleev's table, below Ta and Nb.
The predominant oxidation state is $5+$. Pa(V) forms no simple cations in

aqueous solution and, like Ta, it exhibits an extraordinarily high tendency to undergo hydrolysis, to form polymers, and to be adsorbed on almost any available surface. These tendencies undoubtedly account for the many reports of erratic and irreproducible behavior of protactinium as well as for its frustrating habit of disappearing in the hands of inexperienced or unwary investigators."

From: *The Chemistry of the Actinides and Transactinide Elements* [34].

These paragraphs illustrate in a perfect manner, which difficulties a researcher will face when trying to spectroscopically investigate the protactinium atom:

- small sample size due to the difficult production of protactinium and, of course, due to its radioactivity
- occurrence of extremely complex atomic spectra due to several open shells and up to five valence electrons
- refractory element behavior leading to a high melting point and therewith preventing easy vaporization as necessary in RIS
- formation of complex polymers hindering the reduction to atomic protactinium
- absorption on almost every surface preventing formation of a dense atomic vapor as prerequisite for a stable atomic/ion beam

Due to these complications and its general chemical behavior [34, 35], there is not much knowledge on the atomic or nuclear properties of protactinium. Thus, the absence of a value for the IP of protactinium is not surprising anymore. Even though a theoretically extrapolated value was predicted in the 1970's [36], a direct measurement of the IP is still pending. Just a very rough value could be extracted from systematics along the series of actinides [22, 37].

Already the discovery process of Pa was comparatively tedious. In 1872 Mendeleev proposed a chemical element 91 named "eka-tantalum" with an atomic mass around 235 and chemical properties similar to Nb and Ta [34]. From the radioactive displacement rules proposed 1913 [38, 39] as well as from the missing mother nuclide of Ac in its decay chain [40] it was clear, that an actinide element between thorium and uranium had yet to be discovered. In 1913 Göhring & Fajans discovered a short-lived radio-isotope in the U–Ra decay chain (it was ^{234m}Pa) which they associated correctly with the element 91, and named it "brevium" (Latin *brevis*: short, brief) because of its short lifetime [34]. In 1918 Meitner & Hahn discovered the natural and thus more relevant isotope ^{231}Pa and determined a lifetime between 1200 and 180000 years, which is not assigned as very *"brevis"* anymore. Thus, they suggested

to name it "protactinium" from greek *protos* (first) and "actinium" meaning "predecessor of actinium" in the U–Ac decay chain [41, 42]. The name "protoactinium" is wrongly claimed in tertiary literature [43]: It was givens later by linguists, because it was "better greek" [34, 42], but was officially restored in 1949.

As already mentioned, the production of atomic protactinium is rather sophisticated, expensive and work consuming. Extracting it from natural pitchblende for example is not economically viable at all. Luckily, the United Kingdom Atomic Energy Authority (UKAEA) decided in the late 50's to extract the remaining uranium from a huge amount of around 60 t of radioactive waste. This "sludge" contained aside from around 12 t of high grade uranium also some ppm pf Pa, what is more than ten times the percentage contained in natural pitchblende. Since the costs of US$ 500 000 were covered by the U recovery it was economically worthwhile to extract both, U and Pa. This effort leads to 127 g of ^{231}Pa – showing an remarkable activity of 229 GBq despite the long lifetime – with a high purity of 99.9 % [34]. The material was generously distributed between research facilities around the world. The Pa samples for the spectroscopy described in the following, were kindly provided by the Mainz institute of nuclear chemistry. It is plausible and highly likely, that the Mainz institute of nuclear chemistry, with its founder and first head Fritz Straßmann, also received a fraction of the Pa from UKAEA.

In spite of the expected difficulties, extensive spectroscopic studies were conducted. Objectives were a precise determination of the IP in first place and secondly a gain of information on the overall atomic structure of this extraordinary complex atomic system. The following publication *Excited atomic energy levels in protactinium by resonance ionization spectroscopy* comprises the experimental data of several measurement campaigns, while the analysis on the determination of the IP and the investigation on the atomic structure regarding quantum chaos are treated separately, namely in Sec. 4 and Sec. 5 of this thesis.

3.2 Publication: Excited atomic energy levels in protactinium by resonance ionization spectroscopy

The article was published in August 2018 in *Physical Review A* as an ex-ante presentation of the experimental method, the apparatus used and not at least to make available the vast amount of atomic physics data as basis for a final conclusive analysis of the atomic structure presented separately. The data was gathered within three independent measurement campaigns, which all were held in the LARISSA laboratory in Mainz during the years 2016 and 2017 and also earlier data from T. Gottwald was inspected. In the article a special focus lies on the correct assignment of energy levels, since individual resonances in a spectrum could very well result from different initial states. The final energy values extracted for individual levels are listed in the supplemental material of the article and can be found under https://journals.aps.org/pra/supplemental/10.1103/ PhysRevA.98.022505.

The extensive work load in the experimental spectroscopy was carried out by the thesis author and first author of the publication with strong assistance from Dominik Studer. The entire analysis of the spectra as well as the preparation of the manuscript was done by the doctoral candidate.

Excited atomic energy levels in protactinium by resonance ionization spectroscopy

Pascal Naubereit,* Tina Gottwald, Dominik Studer, and Klaus Wendt
Institute of Physics, University of Mainz, 55128 Mainz, Germany

(Received 18 May 2018; published 10 August 2018)

We present high-resolution data of the single-excitation spectrum of protactinium, reaching slightly beyond the first-ionization threshold. Within this work, more than 1500 energy levels are recorded in different excitation energy ranges below 50 000 cm^{-1}. Our experimental results show that the tabulated data in the literature severely underestimate the density of states particularly regarding the highly excited spectral range.

DOI: 10.1103/PhysRevA.98.022505

I. INTRODUCTION

Laser resonance ionization spectroscopy is an utterly versatile technique for investigations on the atomic shell [1] as well as for gaining knowledge of the characteristics of the nuclear structure and properties of rare species [2,3]. It has been used throughout the Periodic Table of elements for high-precision studies up to fermium; therefore, it is denotable that protactinium ($Z = 91$) is the only actinide below element number 100, the actinide element fermium, for which no spectroscopic measurements were performed until today [4]. To be more precise, it is, besides a few chalcogenic, halogenic, and refractory elements, which are known to be rather difficult to investigate with laser spectroscopic methods, the only element at all [4]. The only ever laser-ionized protactinium beam, without advanced spectroscopy, was demonstrated in [5]. In order to prepare comprehensive studies on the atomic system as well as for nuclear structure research via resonance ionization spectroscopy it is necessary to identify and investigate efficient optical excitation schemes to provide highly resolved spectra.

Here we present high-resolution spectroscopic data of the excitation spectrum of protactinium. Protactinium is also one of the very few remaining elements in the Periodic Table for which the fundamental atomic quantity of the first-ionization potential has not yet been precisely measured [6]; a value of $E_{IP} = 49\,000(110)$ cm^{-1} [6.075(14) eV] has been inferred from systematic comparison to the other actinides and isoelectronic lanthanides [5]. This shortcoming is not only due to the unpleasant radiological and chemical properties of protactinium, which make sample preparation and the production of a stable atomic beam, as required in such experiments, very complicated. Also the complexity of its atomic spectrum has so far prevented a conclusive analysis towards a determination of the ionization potential via Rydberg convergences: Rydberg series could not be identified due to the exceptionally high level density of other excited states below the ionization potential. The level density in the protactinium spectrum even exceeds that of most other actinide and the isoelectronic lanthanide elements. Both groups exhibit several open shells and numerous "active" electrons. The electronic structure of Pa with an even-parity ground-state configuration $7s^2 5f^2 6d$ involves in relativistic notation $7s_{1/2}$, $5f_{5/2,7/2}$, $6d_{3/2,5/2}$, and additionally $7p_{1/2,3/2}$ orbitals. These $N = 32$ possible single-electron states for each individual of the $n = 5$ active valence electrons in Pa lead to $\sim(N)^n/n! \approx 2.8 \times 10^5$ possible electron configurations [7,8]. Given this rough estimate, we note that the 156 even and 494 odd energy levels available in the literature [9] are by far not complete but strongly suggest unobserved levels particularly situated at increasing excitation energies. Furthermore, no level at all has been tabulated so far for excitation energies above 34 500 cm^{-1} (38 500 cm^{-1}) for even (odd) parity [9].

In the measurements presented here, we studied far more than 2000 resonances in the bound spectrum of the Pa atom, covering selected energy ranges and states of different total angular momentum and parity. Making use of multistep laser resonance ionization spectroscopy [10,11] with wide-range tunable Ti:sapphire lasers, extensive scans on resonances and level positions in different energy ranges of the spectrum were recorded.

II. EXPERIMENTAL SETUP

For a fully resonant two-step (three-step) excitation, two (three) lasers of the Mainz titanium:sapphire laser system, involving second-harmonic generation (SHG) and third-harmonic generation (THG), were used. The standard Z-shaped cavity lasers according to [12] have a typical linewidth of 4(1) GHz (fundamental) to 6(1) GHz (SHG) and 7(2) GHz (THG), respectively, and provide an average output power of tunable laser light between 2 and 4 W. The power output for frequency-doubled and -tripled lasers is somewhat lower, depending on wavelength and adjustment, lying somewhat below 500 mW. A Ti:sapphire laser with a grating-assisted resonator served as the scanning laser for spectroscopy. This laser type, a modified development of [13], allows continuous scanning without mode-hop covering almost the complete Ti:sapphire gain range from 650 to 1000 nm. Due to wavelength selection via a refraction grating, a linewidth below 2(1) GHz, with a slightly reduced output power of approximately 2 W, can be achieved. All lasers have a typical pulse length between 30 and 90 ns. A commercially available frequency-doubled diode-pumped solid-state Nd:YAG laser (Photonics Industries

*naubereit@uni-mainz.de

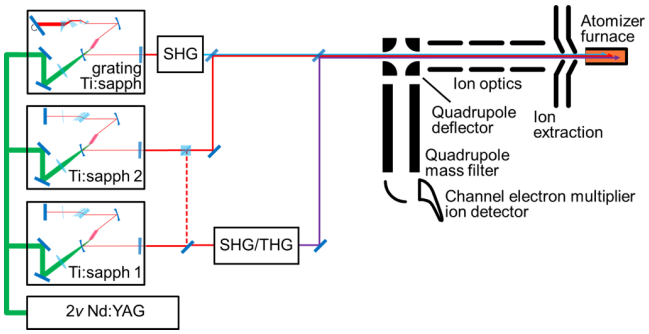

FIG. 1. Sketch of the experimental setup including the Ti:sapphire laser system on the left-hand side and the mass spectrometer system on the right-hand side. For details, see the text.

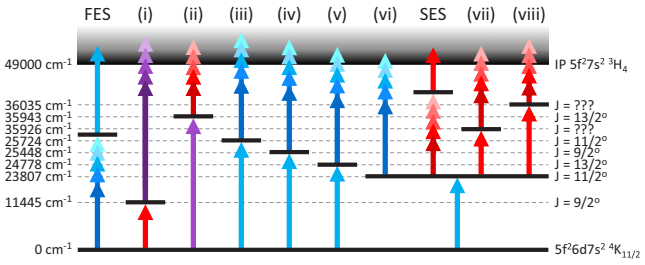

FIG. 2. Compilation of excitation schemes for resonance ionization spectroscopy used for protactinium within this work. For further details see the text.

DM 100-532) at 10-kHz repetition rate delivers the necessary pump power of 10–15 W for each Ti:sapphire laser. For more detailed information on the laser system used, see, for example, [14] and references therein.

Figure 1 gives an overview of the apparatus; the laser system is depicted schematically on the left-hand side. The right-hand side shows a sketch of the low-energy mass spectrometer system, the Mainz Atomic Beam Unit. The lasers are guided inside, anticollinearly overlapped to the atomic beam into the atomizer furnace. Samples of typically 10^{14} atoms of ^{231}Pa dissolved in nitric acid are crystallized on a zirconium foil acting as reduction agent, which is afterward placed in the atomizer furnace. The resistively heated graphite furnace with an inner diameter of 2.2 mm and a length of 50 mm is internally fully lined by tantalum to prevent formation of PaC on the walls [15]. After vaporization at temperatures above the melting point of protactinium at 1568 °C and reduction of PaO, PaO_2, and especially the high-stable Pa_2O_5 molecules, the Pa atoms are ionized via stepwise excitation by the laser radiation, drift towards the exit hole of the furnace, and are extracted and accelerated with low electric fields on the order of 10 V/mm. After passing ion optics for beam shaping, the ions are separated from evaporated neutral species by bending the ion beam in a 90° electrostatic quadrupole deflector. Subsequent mass separation with a radio-frequency quadrupole mass filter separates the ^{231}Pa ions from other ionic species before the ions are detected by a channel electron multiplier in single-ion counting mode.

Several effects, e.g., Doppler broadening and broadening due to the laser linewidth, increase the width of measured resonances compared to their natural linewidth, but an achieved resolution in the range below 20 GHz (FWHM) for most transitions is still well suited for resolving individual states with high precision. However, we have to mention that some transitions into autoionizing resonances may exceed this value by far.

III. WIDE-RANGE HIGH-RESOLUTION LASER RESONANCE IONIZATION SPECTROSCOPY

The overall scanning range of the Ti:sapphire laser system is spanning only 1500 cm^{-1}. Thus, we have probed the spectrum of Pa I in several ranges, from 23 600 cm^{-1} up to the first-ionization potential and slightly above. We used several excitation schemes in order to investigate different total angular momenta of both parities. Figure 2 gives an overview on all investigated excitation schemes. Herein, the arrows in out-fading colors depict the scanned step and the color itself gives a hint to the laser wavelength range in each step. Levels where the configuration or a J value is indicated can also be found in the literature [9]. All schemes where the ionization step was scanned are labeled in roman numerals, while FES (SES) describes the search for a first (second) excitation step using a nonresonant ionization step. All schemes start from the even-parity atomic ground-state configuration $7s^2 5f^2 6d\ ^4K_{11/2}$ located at zero energy (0 cm^{-1}). To ensure that the excitation does not start from a thermally populated fine-structure component slightly above the lowest ground state, found at 825.42, 1618.3, or 1978.2 cm^{-1} (odd parity), we choose transitions into energy levels, listed in the literature with an unambiguously assigned value for the total angular momentum [9]. Based on the selection rule $\Delta J = \pm 1, 0$, fulfilled for every optically allowed dipole transition, and the known J value of the initial state, a range of just three [five for the three-step schemes (vii) and (viii)] neighboring J values can be inferred for our measured resonances. Beyond that, some total angular momenta of resonances could be assigned by comparing several scans of excitation schemes with different J values (see the Supplemental Material [16]).

The uncertainties of all energy levels measured in this work are calculated in a similar way. The statistical error accounts for fitting errors in the first place. A smaller contribution is ascribed to the data acquisition, which slightly shifts the spectra depending on scan direction and speed. The latter can be easily corrected, but result in a small contribution to the overall statistical uncertainty. The systematic uncertainty is produced by the wavelength measurement using a High Finesse WS6-600 wavelength meter. Fast statistical scattering is averaged out due to a rather low scanning speed and the fitting procedure. Long-term drifts and absolute measurement uncertainties are covered within the specified 1σ absolute accuracy. Thus it must be applied for every measured wavelength contributing to the total excitation energy of each level.

In the following sections level energies are compared to the levels available in the literature [9]. According to [17–19], i.e., the primary resources of [9], the resonance energies might be slightly shifted due to variations in excitation probability of the underlying hyperfine-structure components. As a consequence, we added half of the hyperfine-structure width given in [9] as additional uncertainty of the literature values for

TABLE I. Compilation of energy ranges, parity, total angular momenta, and number of atomic transitions in protactinium as identified in the different excitation schemes: FES, SES, and (i)–(viii). Energy levels available in literature [9] are given for comparison.

Scheme	Energy range (cm^{-1})	Parity	Range of J	Transitions
FES	23600, . . . , 26000	odd	$\frac{9}{2}, \ldots, \frac{13}{2}$	88
SES	35800, . . . , 36400	even	$\frac{9}{2}, \ldots, \frac{13}{2}$	32
(i)	48600, . . . , 49100	even	$\frac{7}{2}, \ldots, \frac{11}{2}$	215
(ii)	48900, . . . , 49500	even	$\frac{11}{2}, \ldots, \frac{15}{2}$	67
(iii)	48100, . . . , 49500	even	$\frac{9}{2}, \ldots, \frac{13}{2}$	424
(iv)	49200, . . . , 50000	even	$\frac{7}{2}, \ldots, \frac{11}{2}$	159
(v)	48600, . . . , 49500	even	$\frac{11}{2}, \ldots, \frac{15}{2}$	119
(vi)	48100, . . . , 49400	even	$\frac{9}{2}, \ldots, \frac{13}{2}$	432
(vii)	47900, . . . , 49100	odd	$\frac{7}{2}, \ldots, \frac{15}{2}$	472
(viii)	48500, . . . , 49700	odd	$\frac{7}{2}, \ldots, \frac{15}{2}$	316
[9]	0, . . . , 34500	even	$\frac{3}{2}, \ldots, \frac{17}{2}$	156
[9]	2000, . . . , 38500	odd	$\frac{3}{2}, \ldots, \frac{17}{2}$	494

comparison. In cases where no width was indicated, we took the half mean of all given widths as the uncertainty.

Table I gives a compilation of the number of individual resonances which were determined in the ten different two- and three-step excitation schemes given in Fig. 2. We have to mention that in this compilation several schemes contain a number of identical energy levels. For a complete list of levels observed in this work we refer to the Supplemental Material [16]. For comparison, the numbers of hitherto tabulated levels in the literature [9] are included in Table I, covering a range about half of the excitation energies up to the first-ionization potential. For most of these levels, parity and total angular momentum have been assigned.

A. Search for first and second excitation steps

There is no simple procedure to experimentally distinguish between excitations starting from the ground state or, alternatively, from a thermally populated state located slightly above. Already at a moderate atomizer furnace temperature of 1500 °C, the state at 825.42 cm^{-1} has a population ratio of 20%. Another problem appears since for the two-step schemes (i)–(vi) the radiation of the first and the scanning laser could swap regarding the consecutive steps of the ladder of excitation. Correspondingly, the scanning laser might excite the atoms into a first excited state and the actual first-step laser serves for nonresonant ionization. The following procedure is used to circumvent these difficulties during data analysis: At first, for every detected resonance, two energies are calculated, one expecting the transition to start from the ground state and the other expecting the transition to start from the thermally populated state at 825.42 cm^{-1}. To the energies obtained (note that every transition is now doubly existent), a set of five rules is applied.

(a) The available literature data found in [9] are correct. That means matching energies in any scan for either value, starting from the ground state or from the thermally excited state, are considered as first excited states, as long as the total angular momentum is suitable.

(b) All transitions that appear in more than one scan are considered as leading into a first excited state; again this is valid for both excitations considered as starting from the ground state or from the thermally populated state.

(c) If for one resonance neither the transition starting from the ground state nor from the thermally populated state fulfills rule (a) or (b), this resonance line is considered as leading into a second excited state. In contrast, the remaining transitions in the FES scheme are considered to lead into first excited states.

(d) For any transition matching one of the rules above, the corresponding "other" transition, i.e., starting either from the ground state or from the thermally populated state, is discarded. This ensures that for each resonance in a spectrum only one energy level remains in the end.

(e) The few remaining resonances that fulfill more than one of the rules above and resonances where transitions starting both from the ground state and from the thermally populated state match a rule are treated as special cases, which are analyzed separately.

After this separation procedure the total excitation energy for every transition was calculated. In total 239 first excited states were found and are displayed in Table III in the Supplemental Material [16]. Obeying rule (a), 72 of them can directly be found in [9] and thus a total angular momentum can be assigned. For two of them, numbers 145 and 159 in Table III in the Supplemental Material [16], the range of possible total angular momenta given in [9] could be limited to the value $\frac{11}{2}$. Rule (b) can be applied to 167 levels, while for 67 of them the energies appear only in scans starting from the ground state *or* from the thermally populated state. These 67 level energies are somewhat unreliable as we cannot state explicitly from which state the excitation starts; they are thus labeled with a question mark in the Supplemental Material [16]. For these presently detected energy levels, there is a chance between 47% (at 1500 °C) and 35% (at 2000 °C) for excitation from the ground state, depending on the temperature in the source region, and between about 20% (at 1500 °C) and 18% (at 2000 °C) from the state at 825.42 cm^{-1}. For the other 100 levels it was possible to restrict the range for the total angular momentum. One transition with an energy of $27\,812.68(19)_{stat}(1)_{sys}$ cm^{-1} is supposed to start from the thermally populated odd state at 1978.22 cm^{-1} leading to an even-parity level, while all other transitions lead to odd-parity levels. Level number 119 in the table for odd levels (Table III of the Supplemental Material [16]), would match a level at $25\,891.71(1)_{stat}(1)_{sys}$ cm^{-1} from [9] if we consider an excitation from the state at 825.42 cm^{-1}, but should not be accessible due to the assigned total angular momentum of $\frac{15}{2}$ [9]. Despite our confidence in the correctness of the energy level assignments, there is still a non-negligible possibility that a second-step transition coincidentally matches the energy of a first excited state.

Figure 3 shows the scan of the search for a first excitation step in the lower trace. The poor statistics especially at lower excitation energies in this scan are caused by low laser powers and an almost depleted sample.

In a further step of the excitation scheme development we scanned with an infrared laser to reach an energy range around 36 000 cm^{-1} by a two-step excitation. Therefore, we

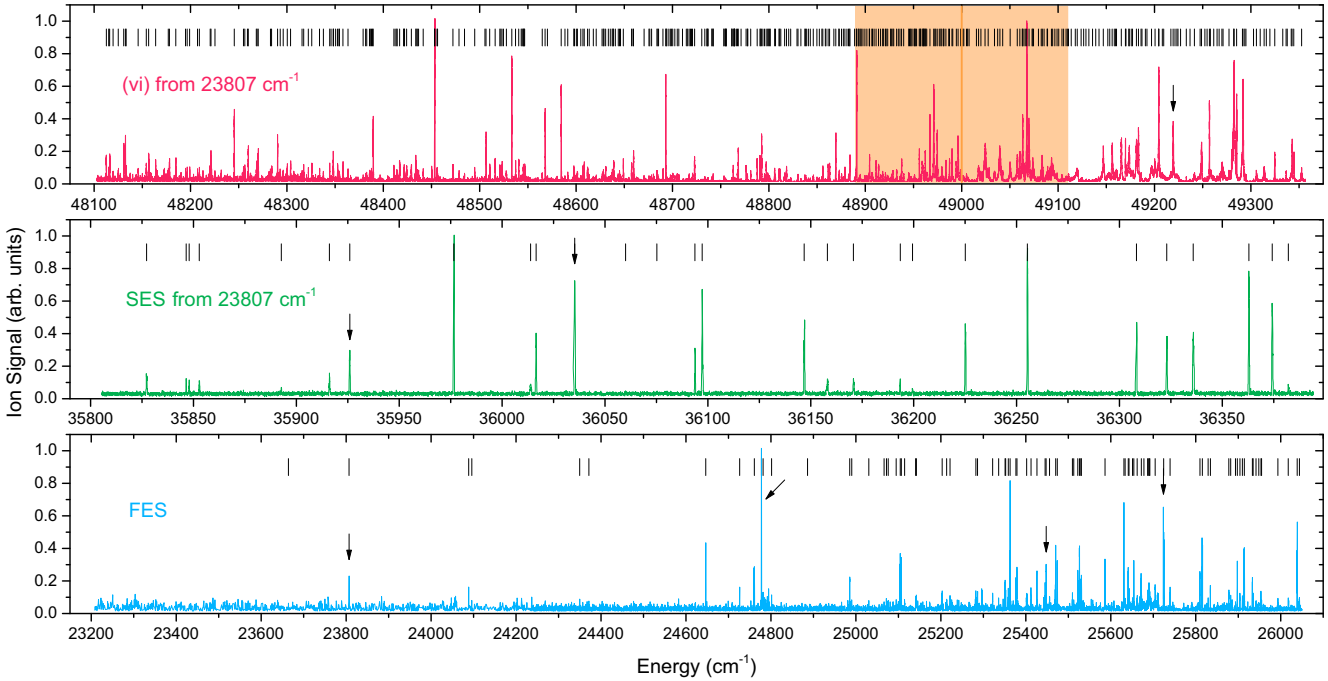

FIG. 3. Different wide-range scans with normalized count rates. The energy scale shows the calculated total excitation energy. Every resonance is indicated by a black bar above the spectra, while arrows indicate resonances used in the various excitation schemes of Fig. 2 or for the frequency scans of Fig. 4. The bottom graph shows the search for a first excitation step, the middle the search for a second excitation step, and the top the scan of scheme (vi). In this scan, the orange line represents the value for the expected ionization potential of $E_{\mathrm{IP}} = 49\,000(110)\ \mathrm{cm}^{-1}$ with its uncertainty range visualized as the light orange area.

used the odd-parity energy level at 23 807 cm^{-1} with a total angular momentum of $J = \frac{11}{2}$ as the first excited state. Of all the levels with sufficient excitation probability and assigned J value detected in the FES scheme, this state has one of the lowest energies [9]. A nonresonant one-color two-photon ionization above an estimated ionization potential of $E_{\mathrm{IP}} = 49\,000(110)\ \mathrm{cm}^{-1}$ is not possible. A range of $J = \frac{9}{2}, \ldots, \frac{13}{2}$ for the second excited states is accessible. Additional to the laser for excitation into the first excited state and the scanning laser, a third laser, also operating in the infrared range, was utilized to ionize from the second excited states nonresonantly. To ensure that the measured resonances represent second excited states, and do not accidentally coincide with alternative first excited states, the scan was repeated with three different nonresonant ionization steps. Consequently, only levels appearing in at least two scans were accepted as second excited states. Those 28, out of 32 in total, energy levels are listed in the compilation for even-parity energy levels in Table I of the Supplemental Material [16]. The middle trace of Fig. 3 shows a typical scan of the SES scheme.

B. Two-step excitation schemes

In addition to the previously described schemes, we investigated highly excited energy levels of protactinium via the six different two-step excitation schemes (i)–(vi) in energy ranges around 49 000 cm^{-1} situated below to slightly beyond the expectation for the first-ionization potential. The first excited states for schemes (i) and (ii) are taken from the literature [9], while for the others a state found via the FES scheme was used. All of the first excited states can additionally be found in [9] and have a clearly assigned value for the total angular momentum, which once again results in a range of three consecutive J values for the measured resonances within the second step. The upper trace of Fig. 3 shows the very dense scan of scheme (vi) as an example for the highly excited spectra.

Schemes (i) and (ii) use laser light in the ultraviolet range for either the scanning or the first-step excitation, respectively. In both cases the sum frequency generation technique was applied [20]. For the scanning uv laser two individual lasers are needed. One intracavity frequency-doubled laser [21] at a fixed wavelength is sum frequency mixed with the scanning laser running in fundamental wavelength operation. The uv laser with fixed wavelength, as needed for scheme (ii), is a frequency-tripled laser, where only one laser is frequency doubled and then again mixed with its own fundamental wavelength output. Unfortunately, for scheme (i) we cannot check if the resonances found are first-step transitions, because we did not perform first-step searches in that energy range due to the experimental challenge for the further excitation steps nor did the literature cover this energy range. In addition, the number of detected energy levels is very low compared to other schemes of the same parity and energy range, as depicted in Table I. Due to this fact, a presumably low transition strength for the first excitation step may cause many resonances of scheme (ii) to remain undetected. Nevertheless, none of the detected transitions of scheme (ii) seems to belong to first excited states comparing the fundamental energies of the scanning laser to the literature data [9].

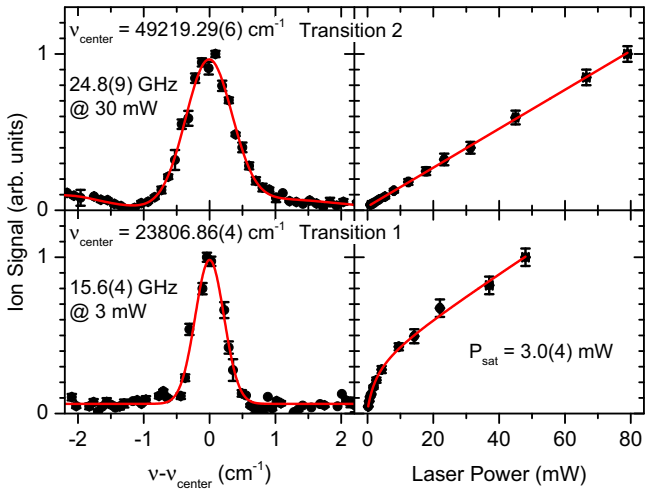

FIG. 4. Frequency scans and saturation curves for the two-step excitation scheme (vi). Here the second transition yields for an autoionizing state at 49 219 cm^{-1}, hence the saturation shows linear behavior. Both linewidths and the saturation power of the first transition are noted in the graph. See the text for further details.

Applying the rules described in Sec. III A, the entirety of second excited even-parity energy levels with their own range of J values found via the two-step schemes (i)–(vi) was finally compared after calculating their total excitation energy. They are given in Table II in the Supplemental Material [16] for even-parity energy levels. For levels matching each other within their uncertainties, the weighted averages are given as the final level energy. Wherever possible, the values of the total angular momenta were limited due to a procedure of exclusion.

Figure 4 shows frequency scans and saturation curves of one exemplary pair of transitions measured along scheme (vi), where the second step populates an autoionizing state at an excitation energy of 49 219 cm^{-1}. On the left-hand side of this resonance, the tailing from a neighboring resonance is visible. In order to optimize the ionization efficiency, the saturation behavior was investigated for every transition [14]. The resulting saturation curve of the first transition shows a clear saturation behavior followed by a somewhat unexpected linear slope. Due to the high level density in protactinium, a second-step transition might lead nearly resonantly to an energy level located around $2 \times 23\,807$ cm^{-1} followed by nonresonant ionization. The second transition exhibits a linearly increasing count rate with laser power due to a nonsaturated autoionizing resonance. The resonance scans on the left show nonsaturated peak shapes, namely, a Gaussian profile for transition 1 and a rather symmetric Fano profile for transition 2, respectively. Note that the linewidth for the first transition with a width of 15.6 GHz is much broader than most of the other transitions measured below the expected first-ionization potential. This fact is ascribed to the relatively broad hyperfine structure involved: A width of 11.5 GHz is given in [9].

C. Three-step excitation schemes

Schemes (vii) and (viii) are three-step excitation schemes, where the transition from the ground state into the $J = \frac{11}{2}$ state at 23 807 cm^{-1} was used as the first excitation step. The second excited state for both schemes was initially detected via scans using the SES scheme, as shown in the center trace of Fig. 3. For these states with energies of 35 926 and 36 035 cm^{-1}, respectively, a range for the total angular momentum of $J = \frac{9}{2}, \ldots, \frac{13}{2}$ is suitable. Consequently, this results in a range of $J = \frac{7}{2}, \ldots, \frac{15}{2}$, which is permitted for energy levels detected by the scanned third excitation step. Note that the third excited states may also lead into one of three consecutive J values. Since we do not know the J value of the intermediate second excited state, the range of these three values is comprised within the interval of five consecutive J values given. First and second excited states are chosen in such a way that direct nonresonant ionization from the first excited state with photons of the third laser is very unlikely to occur without a necessary intermediate resonant laser step. Nonetheless, other combinations could be possible, but are not expected to be strong. To verify this statement, we performed an exclusion scan, where the intermediate second-step laser was blocked. The remaining resonances in this scan were compared with schemes (vii) and (viii), here with a 3σ systematic uncertainty, and matching levels were directly sorted out from the scans for schemes (vii) and (viii). Similar to the two-step scans, also a comparison of possible transitions from the ground state with the literature levels [9] was performed during which further matching transitions were again sorted out. After these procedures, we are confident that the energies of the levels given for schemes (vii) and (viii) in the table for odd-parity energy levels in the Supplemental Material [16] are correct. The odd-parity levels in this list were also compared with their total energy and if two levels matching each other within their uncertainties were found, the weighted averages were calculated.

IV. CONCLUSION AND OUTLOOK

An extensive search for resonance ionization schemes was performed in protactinium. We identified far more than 2000 resonances and found about 1500 so far undocumented energy levels. Most of these levels are located around the expected value for the first-ionization potential at 49 000(110) cm^{-1} and cover both parities and several different total angular momenta. The achieved resolution is limited by the experimental linewidth of typically below 20 GHz for levels below the first-ionization potential with significantly broader autoionizing resonances above. Some of the detected levels indicate signs of broad hyperfine splittings which need to be investigated more thoroughly. In this work every resolved peak was fitted separately, because it was not possible to define whether it is an individual level or a hyperfine component. Since we have not found clear Rydberg series in any of the spectra, we have investigated the level structure more deeply in order to nevertheless extract a reasonably precise value for the first-ionization potential applying different analytical approaches. In parallel, we evaluated this extraordinary complex atomic structure concerning indications of intrinsic quantum chaos through analyzing the measures of spectral fluctuations (cf. [22,23]) and compared our findings to recently published simulated data [24] and theoretical predictions as given by the random matrix theory.

ACKNOWLEDGMENTS

The authors want to thank N. Trautmann and P. Thörle-Pospiech from the Mainz Institute of Nuclear Chemistry for preparation of the protactinium samples. P.N. gratefully acknowledges the Carl-Zeiss-Stiftung and D.S. the EU through ENSAR2 RESIST (Grant No. 654002) for financial support.

[1] M. Laatiaoui *et al.*, Nature (London) **538**, 495 (2016).
[2] K. M. Lynch *et al.*, Phys. Rev. C **97**, 024309 (2018).
[3] C. Granados *et al.*, Phys. Rev. C **96**, 054331 (2017).
[4] P. Campbell, I. D. Moore, and M. R. Pearson, Prog. Part. Nucl. Phys. **86**, 127 (2016).
[5] K. Wendt, T. Gottwald, C. Mattolat, and S. Raeder, Hyperfine Interact. **227**, 55 (2014).
[6] A. Kramida, Y. Ralchenko, J. Reader, and NIST ASD Team (2015), NIST Atomic Spectra Database, version 5.3, available at http://physics.nist.gov/asd (accessed 29 September 2016) (National Institute of Standards and Technology, Gaithersburg, 2015).
[7] V. V. Flambaum, A. A. Gribakina, G. F. Gribakin, and M. G. Kozlov, Phys. Rev. A **50**, 267 (1994).
[8] V. A. Dzuba and V. V. Flambaum, Phys. Rev. Lett. **104**, 213002 (2010).
[9] J. Blaise and J.-F. Wyart, Energy Levels and Atomic Spectra of Actinides, available at http://web2.lac.u-psud.fr/lac/Database/Contents.html (accessed 29 September 2016) (TIC, Paris, 1992).
[10] R. V. Ambartzumian and V. S. Letokhov, Appl. Opt. **11**, 354 (1972).
[11] V. S. Letokhov and V. I. Mishin, Opt. Commun. **29**, 168 (1979).
[12] S. Rothe, B. A. Marsh, C. Mattolat, V. N. Fedosseev, and K. Wendt, J. Phys.: Conf. Ser. **312**, 052020 (2011).
[13] A. Teigelhöfer, P. Bricault, O. Chachkova, M. Gillner, J. Lassen, J. P. Lavoie, R. Li, J. Meißner, W. Neu, and K. D. A. Wendt, Hyperfine Interact. **196**, 161 (2010).
[14] P. Naubereit, J. Marín-Sáez, F. Schneider, A. Hakimi, M. Franzmann, T. Kron, S. Richter, and K. Wendt, Phys. Rev. A **93**, 052518 (2016).
[15] C. Keller, Angew. Chem. Int. Edit. **5**, 23 (1966).
[16] See Supplemental Material at http://link.aps.org/supplemental/10.1103/PhysRevA.98.022505 for all energy levels found within this work. The Resonances detected via the various excitation schemes have been compared in order to extract the positions of the energy levels. They are grouped in four tables for even and odd as well as low and high energy. Where possible, J-values or ranges of J-values have been deduced. Levels with an uncertain energy position are marked with "?". For more information on the determination of energy positions, see full text of the article.
[17] A. Giacchetti, J. Opt. Soc. Am. **56**, 653 (1966).
[18] E. W. T. Richards, I. Stephen, and H. S. Wise, Spectrochim. Acta B **23**, 635 (1968).
[19] J. Blaise, A. Ginibre, and J. F. Wyart, Z. Phys. A **321**, 61 (1985).
[20] Y. B. Band, C. Radzewicz, and J. S. Krasinski, Phys. Rev. A **49**, 517 (1994).
[21] V. Sonnenschein, I. D. Moore, I. Pohjalainen, M. Reponen, S. Rothe, and K. Wendt, JPS Conf. Proc. **6**, 030126 (2015).
[22] F. Haake, *Quantum Signatures of Chaos*, Springer Series in Synergetics Vol. 54 (Springer, Berlin, 2013).
[23] T. Guhr, A. Müller-Groeling, and H. A. Weidenmüller, Phys. Rep. **299**, 189 (1998).
[24] A. V. Viatkina, M. G. Kozlov, and V. V. Flambaum, Phys. Rev. A **95**, 022503 (2017).

Chapter 4

Ionization potential of protactinium

Within the measurement campaigns of resonance ionization spectroscopy on protactinium, a direct extraction of the IP has unfortunately not been achieved due to the complexity and mutual intractability of any regularity in the observed spectrum. Hence, dedicated analytical methods providing the ability to extract the IP from dense atomic spectra were developed and are presented in this chapter. After determination of the functionality of the methods on less complex atomic systems, the extensive spectroscopic data pointed out in the previous chapter was analyzed to extract a value for the IP of protactinium. As qualitative measure for the complexity of an atomic system and as estimate for the expectable number of energy levels, the calculation of possible multi-electron states is used [44]. Discussed already in publication III, protactinium involves approximately 2.8×10^5 possible electron configurations. As system with intermediate complexity the lanthanide element holmium was chosen. It exhibits an electronic ground state configuration of $4f^{11}\,6s^2$ and involves in relativistic notation $4f_{5/2,7/2}$, $6s_{1/2}$ as well as $5d_{3/2,5/2}$ orbitals. These $N = 26$ single electron states for each of the $n = 5$ lesser bound "active" electrons – the three, which are not paired in the $4f$-shell, together with the two easily accessible $6s$ electrons – lead to approximately $(N)^n/n! \approx 9.9 \times 10^4$ possible electron configurations. Sodium serves as an atomic system with lower complexity. The calculation mentioned here is not necessary for Na with its only one single valence electron in its ground state configuration of $3s^1$, but it is a model case for IP extraction from Rydberg convergences as pointed out in publication I. To motivate and justify the new analytical methods that were developed and are tested here, the conventional spectroscopic procedures that could not be applied for the IP determination for Pa are introduced briefly. Afterwards the procedures for the work in complex atomic spectra are worked out and applied to protactinium. With that, the first ever precisely assigned value for its IP is extracted.

4.1 Direct measurement techniques for the IP

RIS is a most powerful tool also for the direct measurement of ionization potentials. Two very precise techniques have been used throughout the last decades, namely the determination via Rydberg convergences and application of the saddle point model, respectively. Both methods are discussed in full detail for example in [22] and are introduced briefly in this section.

4.1.1 Rydberg convergences and separation of Rydberg levels

The ideal case of Rydberg spectroscopy was presentend in the publication *Resonance ionization spectroscopy of sodium Rydberg levels using difference frequency generation of high-repetition-rate pulsed Ti:sapphire lasers*. There, sodium, as an element with only one valence electron, was excited into Rydberg levels. These weakly-bound states decay rapidly into an ion and an electron under the influence of black-body radiation, collisions or external fields. The ion is detected and appears as signal in the laser scan, if the laser wavelength hits a transition into a Rydberg level. With a continuous scan of the laser wavelength, a Rydberg series converging towards the IP can be recorded. According to the well-known Rydberg-Ritz formula, see publication I and [45], a value for IP can be extracted from such Rydberg convergences.

Regarding Rydberg spectra of most of the investigated elements, the unambiguous identification of a series of unperturbed Rydberg levels is not as clear as in the case of sodium or even not possible. If there are obvious series, they are often concealed by disturbers or other strong or stronger resonances. In some cases, the spectra are even that dense, that no clear Rydberg series at all can be identified, cf. the spectra of protactinium as presented in the publication *Excited atomic energy levels in protactinium by resonance ionization spectroscopy*. Hence, methods for separating Rydberg levels from other valence states need to be applied. Two powerful attempts are discussed here, while a detailed discussion on those techniques can be found e.g. in [22].

Delayed field ionization

The Delayed field ionization (DFI) takes advantage of the relatively long lifetime of Rydberg states reaching into the μs range. To prevent that an "undefined" ionization takes place to early, the atoms are excited within a well-shielded area without any external fields or heat radiation – in RIS, this is only achievable if the excitation takes place outside the atomizer furnace, cf. the experimental setup described in publications I or III. Once excited into states close to the ionization potential, the population in all other valence states starts to decay rather quickly while the one in Rydberg levels still remains in its high excitation. After a waiting time of up to the lifetime of Rydberg levels, an intense electric field pulse is applied to the excitation region ionizing the remaining highly excited atoms, which are now only

atoms in Rydberg states. With this procedure, the resulting spectra ideally contain only Rydberg levels and can thus be analyzed and further evaluated easily.

Isolated core excitation

The Isolated core excitation (ICE) is a second method for separating Rydberg levels from other states but must also be carried out in regions without fields or heat radiation to prevent ionization. Here, the basic idea is that the Rydberg electron is far away from the remaining atom, so that no shielding occurs and the remaining atom resembles a singly ionized ion. In addition to the lasers exciting the Rydberg – and unwanted other – levels, another laser induces a transition from the ionic ground stated into a known excited ionic state. This ionic transition can only be resonant if an "ion" is present, i.e. in case of an excited Rydberg atom. Thus, a Rydberg atom produces a signal on the ionic transition while this is not possible for other excited valence states. Scanning of the Rydberg excitation laser again delivers spectra ideally only containing Rydberg levels that can be easily analyzed and used for extracting a value for the ionization potential.

Saddle point model

In some specific cases, the IP determination via Rydberg convergences may not be possible at all due to the complexity of a spectrum – like in the case of protactinium – and even with the separation methods discussed so far, accidentally remaining levels could be falsely assigned to the Rydberg series. In these cases, a determination of the ionization potential by RIS can be attempted by applying the saddle point model (SPM). This method was used in Mainz for the first-time determination of the IP of ten actinides [46, 47] and most recently in a refined version for the IP determination of the also exceptional complex promethium atom [5], discussed in detail in the thesis of D. Studer [48].

Within the SPM an electric field with strength E applied to the excitation region lowers the ionization threshold proportional to $\sqrt{E}$. Thus, an excited energy level below the IP will not ionize and contribute to the detected signal until E is high enough. With a determination of the ionization threshold as function of the external electrical field, the IP can be extracted via extrapolation of the resulting curve along $\sqrt{E} \rightarrow 0$. Accordingly, a dense spectrum as e.g. in protactinium is an advantage regarding the precision of determination of the IP for the SPM.

4.2 Analytical extraction of the IP from complex atomic spectra

During the different measurement campaigns, for which the results are presented in the publication *Excited atomic energy levels in protactinium by resonance ionization spectroscopy*, all of the methods discussed above in Sec. 4.1 were applied in order

to directly measure the ionization potential of protactinium. Unfortunately, none of them worked out. Primarily due to the chemical properties of protactinium as discussed in Sec. 3.1, the formation of a stable atomic beam effusion from a surface failed. Thus, RIS was only possible with sufficient efficiency inside an atomizer furnace where the atom vapor density was high enough but not outside in a field-free region, as would be needed for all those measurement and spectroscopic line separation techniques.

Nevertheless, as a promising alternative, the numerous spectra of protactinium, obtained via RIS, cf. publication III, were approached by specific statistical and analytical methods for an extraction of the ionization potential as presented in the following sections.

4.2.1 Level density collapse

A first approach exploits the level density collapse (LDC) above the ionization potential. Regarding high-energy excitation spectra of protactinium – examples are given in publication III, Fig. 3, top panel or in publication IV, Fig. 1, top panel – a significant reduction, drop or collapse of the level density is expected and finely apparent above the ionization potential. One exemplary spectrum of protactinium is shown in Fig. 4.1. It visualizes the spectroscopic data obtained via excitation scheme (viii) as named in publication III. Note, that the peak heights are arbitrarily scaled to gain visibility especially of the smallest resonances. The gray line represents the value for the expected ionization potential of $E_{\mathrm{IP}}^{\mathrm{Pa}} = 49000(110)$ cm^{-1} [37] with its uncertainty range featured as light gray shaded area. Additionally, the peak positions, displayed as black bars above the spectrum, emphasize a LDC being located just slightly above the expected ionization potential well within its error range.

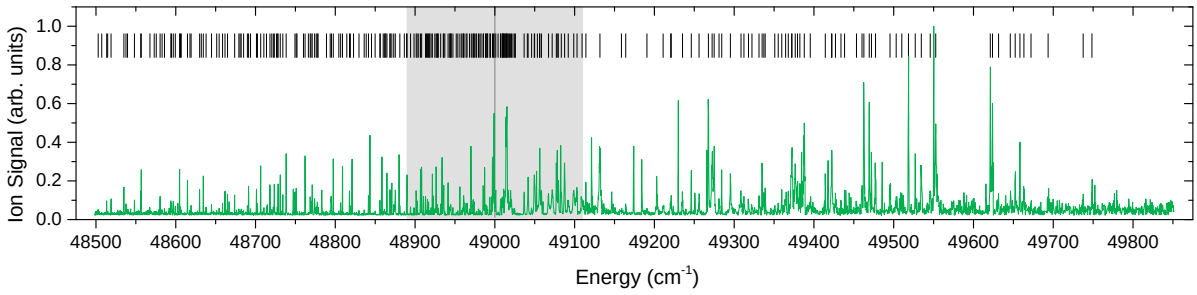

Figure 4.1: Exemplary high-energy excitation spectrum of protactinium via excitation scheme (viii) from publication III. The gray line represents the value for the expected ionization potential of $E_{\mathrm{IP}}^{\mathrm{Pa}} = 49000(110)$ cm^{-1} [37] with its uncertainty range visualized as light gray shaded area. The peak positions are indicated by a black bar above the spectrum.

This trend of a decreasing level density just above the IP is not unique for protac-

tinium but can be traced back and verified also in other complex atomic spectra. In the following analysis, three cases of different atomic complexity will be compared in order to prove the universality of the method. Protactinium constitutes the most complex system whereas sodium, as presented in publication I, provides the most simple system and the spectra of holmium, as discussed in detail in [15], represent an atomic system of intermediate complexity. In the case of sodium – the high-energy excitation spectrum is shown in Fig. 4.2 representing data of publication I – the LDC is not surprising since no resonance at all is expected above the IP until very high excitation energies are reached.

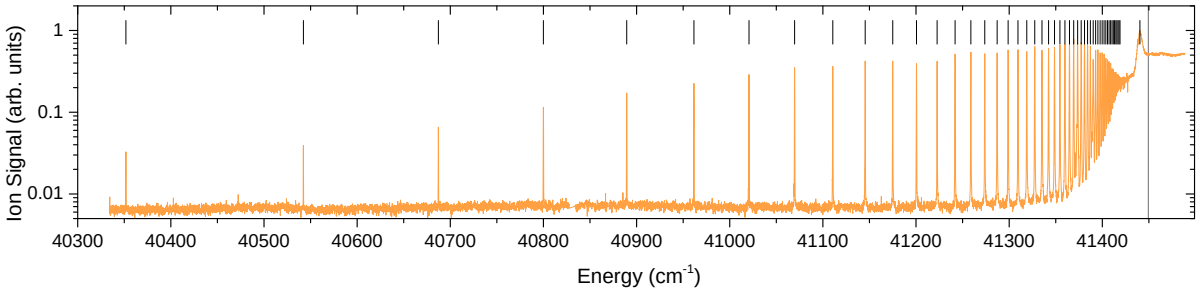

Figure 4.2: High-energy excitation spectrum of sodium. The graph shows a modified version of the upper panel in Fig 4 of publication I. The gray line represents the value for the ionization potential of $E_{\mathrm{IP}}^{\mathrm{Na}} = 41449.451(2)\ \mathrm{cm}^{-1}$ [50,51], whereas the uncertainty range as small as $0.002\ \mathrm{cm}^{-1}$ is not visible in this depiction. The peak positions are indicated by a black bar above the spectrum. For a detailed discussion on the graph, please see publication I.

Fig. 4.3 shows the RIS spectrum of holmium around the IP as obtained in [15]. Again, the peak heights are scaled to gain visibility. For holmium a LDC just above the IP appears as clear as for protactinium at first sight.

To quantitatively analyze the LDC regarding the value for the IP, the level density has to be plotted as function of the excitation energy. The typical approach yields to the so-called cumulative number of levels, a staircase-like function of the excitation energy, as often used for describing spectral statistical properties – this topic is specifically addressed in Sec. 5 and in publication IV. The cumulative number of levels $N_{\mathrm{c}}(E)$ is given as

$$N_{\mathrm{c}}(E) = \int_0^E \sum_i \delta\left(E' - E_i\right) \mathrm{d}E' \tag{4.1}$$

with E_i the energy of the i-th resonance. The level density is given by the derivative of the cumulative number of levels: $\rho(E) = \frac{\mathrm{d}}{\mathrm{d}E} N_{\mathrm{c}}(E)$.

Fig. 4.4(b) shows the cumulative number of levels for the holmium spectrum. The cumulative number of levels for the least complex atomic system of sodium is

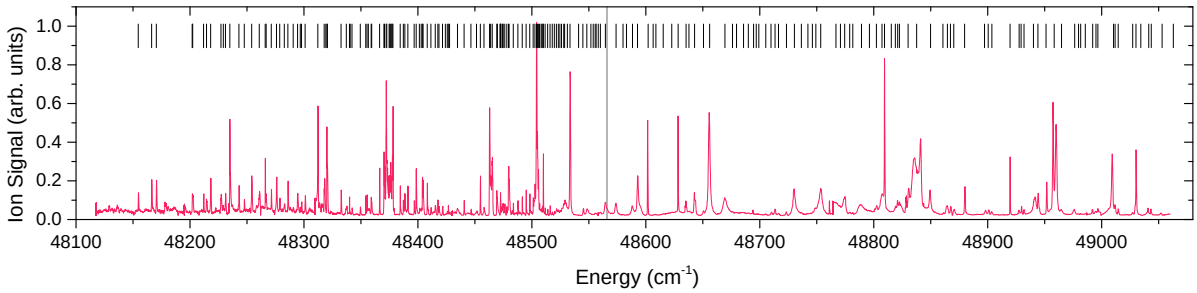

Figure 4.3: High-energy excitation spectrum of holmium as obtained in [15]. The gray line represents the value for the ionization potential of $E_{\mathrm{IP}}^{\mathrm{Ho}} = 48565.910(3)\ \mathrm{cm}^{-1}$ [49], whereas the uncertainty range as small as 0.003 cm^{-1} is not visible in this depiction. The peak positions are indicated by a black bar above the spectrum.

included in Fig. 4.4(a).

Since the level density collapses and thus the staircase plot for $N_{\mathrm{c}}(E)$ changes its shape by exhibiting a sharp kink at a certain energy, namely the IP, a stepwise defined function $N_{\mathrm{c}}^{\mathrm{LDC}}(E)$ serves as fitting function for the cumulative sum of levels. It is defined as

$$N_{\mathrm{c}}^{\mathrm{LDC}}(E) = \begin{cases} y_0 + aE + bE^2, & E \leq E_{\mathrm{LDC}} \\ y_0 + aE_{\mathrm{LDC}} + bE_{\mathrm{LDC}}^2 - c\ln(E_{\mathrm{LDC}}) + c\ln(E), & E > E_{\mathrm{LDC}} \end{cases}, \tag{4.2}$$

where y_0, a, b and c are free parameters. The additional fitting parameter E_{LDC} represents the energy, where the LDC sets in. Since the shape of the staircase plot above the IP is sometimes more logarithmic-like, this type of function was chosen in Eq. 4.2, even though the fits shown in this work look rather linear above E_{LDC}. For the lower part, a parabola fit was sufficient, except for the holmium case, where a hyperbola function was used. In Fig. 4.4(b) a value of $E_{\mathrm{LDC}}^{\mathrm{Ho}} = 48553.5(12)\ \mathrm{cm}^{-1}$ was extracted by fitting Eq. 4.2 to the data. This value is about 10 cm^{-1} below the IP of $E_{\mathrm{IP}}^{\mathrm{Ho}} = 48565.910(3)\ \mathrm{cm}^{-1}$ [49], which gives already a rough estimation of the error produced by the LDC method. Note, that it is expected to deduce a LDC value lying below the IP, which is caused by the detection method: With increasing excitation energy approaching the IP, the level density gets larger and larger, which causes the energy levels to be indistinguishable for RIS. The result is an onset of the LDC already at lower energies. Enhancing the effect, the electrical fields present in the ionization region are regarded as second reason: Electrical fields cause ionization of excited atoms already at excitation energies somewhat lower than the actual IP so that the expected peaks just below the IP "disappear" in a continuously raised background signal. For a deviation of LDC to the IP in the order of $\approx$ 10 cm^{-1}, voltages of around $\approx$ 100V would be necessary. As fields of this strength may be

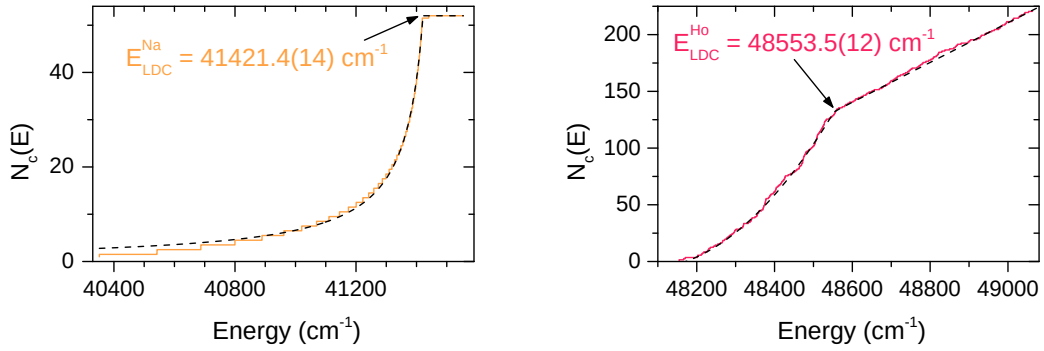

(a) Sodium. The data is fitted by a piecewise defined function (black curve), which leads to a value for the LDC onset in sodium of $E^{\mathrm{Na}}_{\mathrm{LDC}} = 41421.4(14)\ \mathrm{cm}^{-1}$.

(b) Holmium. The dashed black curve represents the piecewise defined funcion Eq. 4.2 fitted to the cumulative sum of levels depicted as red staircase-like plot. The fit leads to an energy of the LDC onset of $E^{\mathrm{Ho}}_{\mathrm{LDC}} = 48553.5(12)\ \mathrm{cm}^{-1}$.

Figure 4.4: Cumulative sum of levels for sodium and holmium as systems of least and intermediate complexity, respectively.

found in the ionization region of the RIS apparatus in use, this seems to be plausible.

The described effects are even more important in the case of sodium where no levels above the IP are present to improve the fit. The extracted value of $E^{\mathrm{Na}}_{\mathrm{LDC}} = 41421.4(14)\ \mathrm{cm}^{-1}$ is about 28 cm^{-1} below the actual IP of $E^{\mathrm{Na}}_{\mathrm{IP}} = 41449.451(2)\ \mathrm{cm}^{-1}$ [50,51].

The LDC method is applied to the system of protactinium in Sec. 4.3, but before that, a second analytical method for the extraction of the IP from dense atomic spectra is presented. With the combination of both methods, the extraction of a more precise value for the IP will be enabled.

4.2.2 Rydberg correlation

The second analytical method for an extraction of the IP from a dense atomic spectrum implies deeper knowledge on Rydberg levels, more precisely the correlation of Rydberg levels belonging to specific series. The existence of unperturbed Rydberg series forms the fundamental hypothesis of the Rydberg correlation (RC) method. Albeit Rydberg levels can not be distinguished from other excited valence states in the case of very dense spectra via the typical methods presented in Sec. 4.1.1, there is no reason to question their existence. Even if intrinsic quantum chaos is involved in the system – see Sec. 5 for details on this topic – Rydberg levels with higher principal quantum numbers n lying in the typical detection range for RIS with pulsed lasers in a hot cavity approach of $n \approx 20 - 60$ should not be affected by chaotic behavior [52].

The RC method is probably best explained by means of a very simple spectrum with a clearly identifiable Rydberg series – as in the case of sodium. Therefore the

spectrum given in the upper trace of Fig. 4 in publication I is used. In more complex systems it is necessary to unify the resonances in a spectrum concerning peak heights and widths to induce visibility. Fig. 4.5 shows the sodium Rydberg spectrum with this procedure applied.

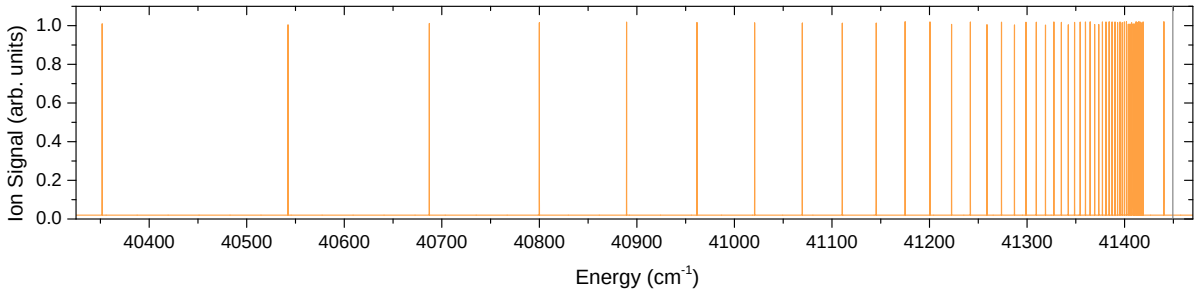

Figure 4.5: High-energy Rydberg spectrum of sodium as obtained in publication I, but with unified peak heights and widths. The gray line represents the value for the ionization potential of $E_{\mathrm{IP}}^{\mathrm{Na}} = 41449.451(2)\ \mathrm{cm}^{-1}$ [50, 51].

If the energy of the IP E_{IP} is known, the energetic positions of the Rydberg levels E_n with certain principal quantum number n are given by the Rydberg formula

$$E_n\,(n) = E_{\mathrm{IP}} - \frac{R_{\mathrm{M}}}{n^2}\,, \tag{4.3}$$

where R_{M} is the mass-reduced Rydberg constant for the requested element[1]. Using Eq. 4.3, the simple transformation

$$E \rightarrow \sqrt{\frac{R_{\mathrm{M}}}{E_{\mathrm{IP}} - E}} \tag{4.4}$$

enables the presentation of the Rydberg spectrum in dependency of n. In this visualization the Rydberg levels become equidistant, in the case that a correct and precise value of the IP is known. For sodium this requirement is fulfilled. Inserting the well-known value $E_{\mathrm{IP}}^{\mathrm{Na}} = 41449.451(2)\ \mathrm{cm}^{-1}$ [50, 51], the Rydberg spectrum of Fig. 4.5 can be plotted in dependency of the principal quantum number giving perfectly equidistant peaks as shown in Fig. 4.6.

As next step the autocorrelation (AC) function of the spectrum in Fig. 4.6 is calculated. For the AC, a point-by-point multiplication of the spectrum $I(n)$ with a shifted

[1] Usually, n in this formula has to be replaced by n^*, the *effective* principal quantum number, which also includes the n-dependent quantum defect $\delta\,(n)$. Since the error produced by omitting the quantum defect is much smaller than the uncertainty produced by the RC method itself, the usage of just n is acceptable.

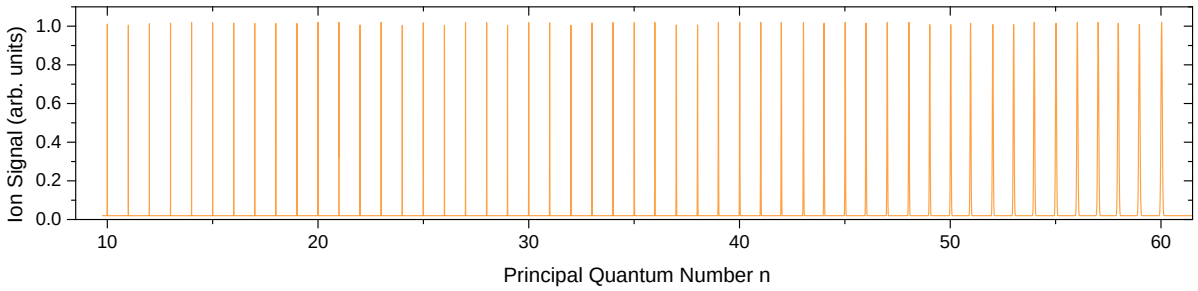

Figure 4.6: Presentation of the unified Rydberg spectrum of Fig. 4.5 in dependency from the principal quantum number n. In this visualization the Rydberg peaks appear equidistant.

version of itself $I(n+\delta n)$ is integrated over all n, or as mathematical expression

$$A(\delta n) = \int_0^\infty I(n) I(n+\delta n)\,\mathrm{d}n\,, \tag{4.5}$$

which gives the AC of the spectrum depending on the shift δn. This function has a maximum whenever the peaks of the shifted spectrum overlap with peaks from the original spectrum. Thus, for equidistant peaks with distance n a maximum appears for all shifts that fulfill

$$\delta n = m \cdot n\,, \quad m \in \mathbb{N}\,. \tag{4.6}$$

The AC function is visualized in Fig. 4.7. The AC function is normalized to the global maximum at $\delta n = 0$ and because the overlap of the spectra becomes smaller for larger shifts, also the local maximums of the AC function become smaller quite quickly. Therefore, in Fig. 4.7, a magnification of the relevant data range is shown.

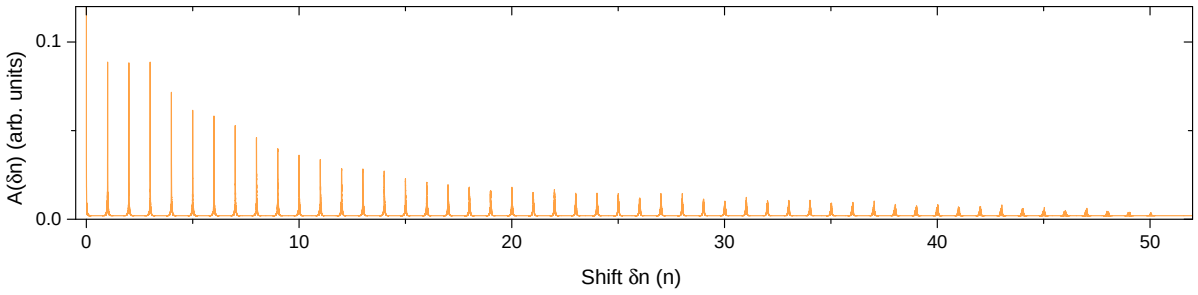

Figure 4.7: Autocorrelation function for sodium for different shifts δn. A magnification of the relevant data range is shown. See text for more information.

Note, that such a clear structure can only appear even for one single clear Rydberg series, if the peaks are really equidistant for which the IP has to be known rather

precisely. However, this method helps to *localize* the IP. For that, the AC function has to be calculated for a large number of different IP values. This results in a three dimensional graph, where a multitude of individual AC functions, as given in Fig. 4.7, are stacked next to each other depending in the second dimension on the value of the IP inserted in Eq. 4.4. As visualization, the resulting three dimensional correlation density plot for sodium is depicted in Fig. 4.8 while a two dimensional contour plot as projection is given above. As expected from the proper choice of the well known IP value, the AC functions show strong global maxima in the center corresponding to the IP of $E_{\mathrm{IP}}^{\mathrm{Na}} = 41449.451(2)\ \mathrm{cm}^{-1}$ [50,51].

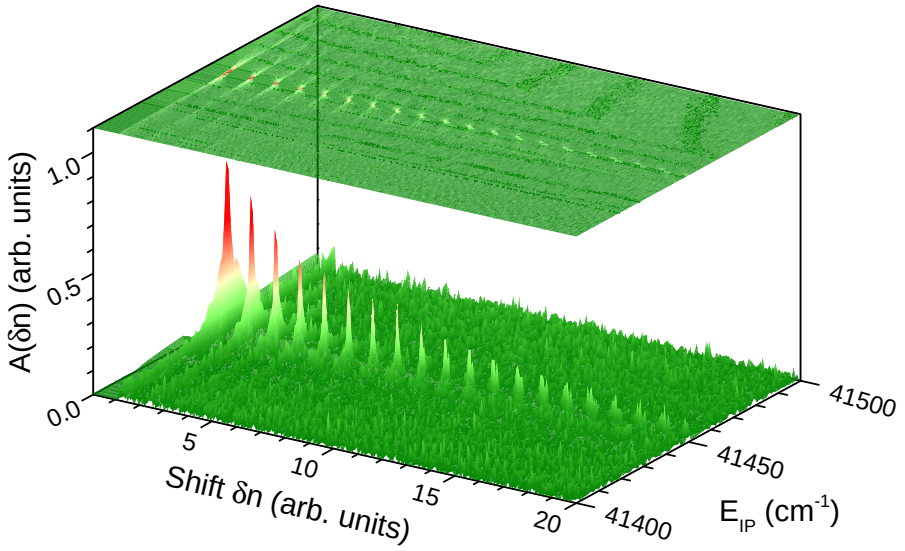

Figure 4.8: Three dimensional correlation density for sodium. Many AC functions for different inserted IP values are stacked next to each other forming the peak structure. Above this structure the two dimensional projection is shown. The correct value for the IP lies at $E_{\mathrm{IP}}^{\mathrm{Na}} = 41449.451(2)\ \mathrm{cm}^{-1}$, where all the AC functions reach their maximum values.

For the final IP evaluation a second projection is carried out by integrating the three dimensional peak structure of Fig. 4.8 over all shifts δn. The projection

$$A_{\mathrm{int}}(E_{\mathrm{IP}}) = \int_0^\infty A(\delta n, E_{\mathrm{IP}})\,\mathrm{d}\delta n \tag{4.7}$$

results. Of course, in the actual calculation, the infinite integral is replaced by a finite, point-wise sum over all shifts δn. Note, if the bins are all of same size like here, taking the total or the mean of each energy bin results in the same curve after normalization. Similarly, instead of the total of each energy bin, the root-mean-square in some cases may help to lower the background without shifting the peak

position. It slightly favors larger values of $A(\delta n)$. Fig. 4.9 shows the projection $A_{\text{int}}(E_{\text{IP}})$ for sodium for 100 different set values of E_{IP} in steps of 1 cm^{-1}. The error bars represent the standard deviation in each of the energy bins. Although contain-

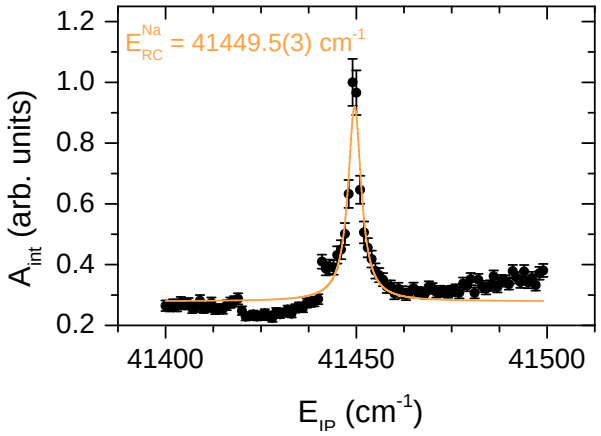

Figure 4.9: Projection of the three dimensional correlation density of Fig. 4.8. The error bars represent the standard deviation in each energy bin. A Lorentzian was fitted to the peak structure leading to a center value of $E_{\text{RC}}^{\text{Na}} = 41449.5(3)$ cm^{-1}, which agrees to the IP value for sodium as extracted with the RC method. See text for more details.

ing only few data points, a clear peak around an set energy of $E_{\text{IP}} \approx 41450$ cm^{-1} is visible. A Lorentzian was fitted to this structure, yielding a center energy of $E_{\text{RC}}^{\text{Na}} = 41449.5(3)$ cm^{-1}. Albeit in perfect agreement with the literature value for the IP of sodium $E_{\text{IP}}^{\text{Na}} = 41449.451(2)$ cm^{-1} [50, 51], the IP value obtained with the RC method is obviously less accurate compared to the literature value. The accuracy would be strongly enhanced, if more Rydberg levels would be available for the AC function and also if more and smaller steps for the IP variation would be chosen. Therewith, the number of data points, and the corresponding accuracy, may be increased, but in this case, it was actively limited due to the time-consuming calculation of the three dimensional correlation density as it was shown in Fig. 4.8.

Moving on to a more complex atomic spectrum, i.e. the one of holmium as exemplary candidate with intermediate complexity, the situation is somewhat different. Instead of having one structure of equidistant peaks for a correct value of the ionization potential, in a more dense spectrum, some peaks may be equidistant for almost every choice of the ionization potential. This results in the appearance of not only one single peak in the projection of the 3D Rydberg correlation, but in numerous or even broad structures with different intensities and widths. To further analyze these structures, a combination of both, the LDC and the RC method, has been employed as demonstrated in the upcoming section.

4.2.3 Combination of LDC & RC method

Fig. 4.10 visualizes the RC spectrum for holmium. The underlying spectroscopic data again stem from [15]. In Fig. 4.10(a), the RC spectrum is given for the entire

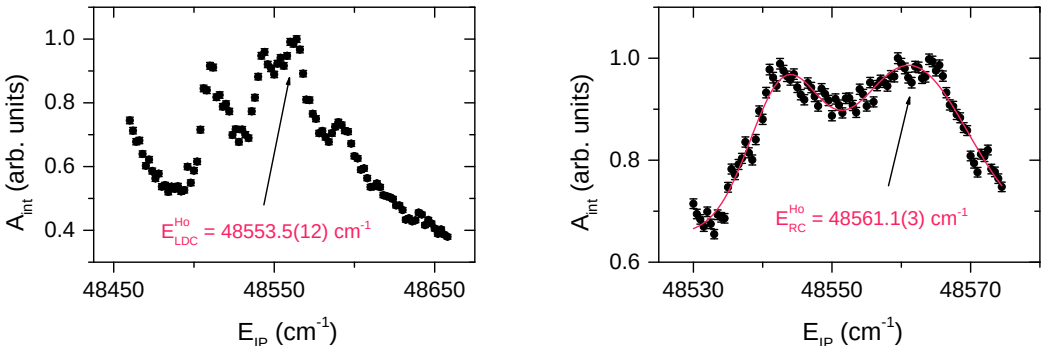

(a) Full view. The arrow indicates the value for the IP as extracted via the LDC method.

(b) Magnification of the area around $E^{\mathrm{Ho}}_{\mathrm{LDC}}$. The red line shows a double-Gaussian fit, from which the center position of the relevant second peak is indicated as $E^{\mathrm{Ho}}_{\mathrm{RC}} = 48561.1(3)\ \mathrm{cm}^{-1}$.

Figure 4.10: Rydberg correlation spectrum for holmium as obtained with the procedure described in Sec. 4.2.2. See text for more details.

IP range of relevance. In contrast to the sodium case many peaks, even approximately equal in height and width, are visible. Only with preceding application of the LDC method, one peak can be identified to yield the correct value for the ionization potential. In doing so, the energy range around the LDC value of Holmium, $E^{\mathrm{Ho}}_{\mathrm{LDC}} = 48553.5(12)\ \mathrm{cm}^{-1}$, is plotted in magnification in Fig. 4.10(b). The remaining double-peak structure was fitted by a sum of two Gaussians, where the second one is the most pronounced peak and the closest to $E^{\mathrm{Ho}}_{\mathrm{LDC}}$ and is thus assumed to be the peak resulting from the correct ionization potential. The fit yields a value of $E^{\mathrm{Ho}}_{\mathrm{RC}} = 48561.1(3)\ \mathrm{cm}^{-1}$ for the ionization potential of holmium. The indicated uncertainty only accounts for the fit error and not for total uncertainty as produced by the RC method. However, this value is very close to the literature value for the ionization potential for holmium of $E^{\mathrm{Ho}}_{\mathrm{IP}} = 48565.910(3)\ \mathrm{cm}^{-1}$ [49]. Because of that, for similar complex atomic structures as in the holmium case, the uncertainty produced by the combination of the LDC and RC method is assumed to be in the order of approximately 10 cm^{-1}. A prove is pending since many more spectra for different atomic systems would be needed to fully characterize the quality of this method. Nevertheless, protactinium with its exceptional atomic complexity maybe seen as perfect test candidate to prove, whether the analytic method is able to extract a value for the ionization potential or not.

4.3 Extracting the IP of protactinium

With the tools obtained in the preceding sections, the attempt was made to extract the ionization potential of protactinium from several dense RIS spectra as obtained in the measurement campaigns for publication III. As shown before, first the LDC method and thereafter the RC method is applied to each spectrum. With the combination of both methods, each spectrum leads to a specific, slightly different value for the expected ionization potential of protactinium. The graphs belonging to the LDC and the RC analysis are comprised for the tested schemes (i) - (iv) in Tab. 4.1 and for schemes (v) - (viii) in Tab. 4.2. The schemes (ii), (iv) and (v) cannot be used for an evaluation with the RC method. Even though for schemes (ii) and (v) a value could be assigned applying the LDC method, in both schemes the energy levels below the assigned values are too few to achieve a reliable analysis with the RC approach. The range of excitation energy covered by scheme (iv) is already above the expected value for the ionization potential of 49000(110) cm^{-1} [37] and thus, no result can be inferred via the methods of investigation. All results inferred via the LDC and the RC method for the ionization potential of protactinium are comprised in Tab. 4.3. For those excitation schemes, where more peaks could be fitted during the RC analysis, all relevant energies are given in this column. The values that match the inferred LDC values withing their uncertainties are marked in bold font. The uncertainties are given by the fit errors for the LDC values and the half width at half maximum (HWHM) of the fitted peaks for the RC values, respectively. For scheme (vii) two values lie within the uncertainty range of the relevant LDC energy, so that their average of 49027(2) cm^{-1} is considered for the further analysis.

Before calculating a final value for the IP, it must be mentioned that the results obtained in scheme (i) are not considered as appropriate. In this scheme, with the RC method a strongly pronounced peak was obtained. Unfortunately, the position of the peak is not coinciding with the energy inferred via the LDC method. The curve and the fit of the LDC, especially the collapse itself is not as clear as for the remaining schemes. Thus, it is believed, that the RC result is more trustable than the LDC result. However, for the sake of consistence, only the four remaining schemes (iii), (vi), (vii) and (viii) with a coincidence between LDC and RC are used for the IP calculation.

For the extraction of a final value for the ionization potential of protactinium the mean of the energies from the four different schemes is calculated. This leads to

$$E_{IP}^{Pa} = 49034(10)\ \text{cm}^{-1} \tag{4.8}$$

as value for IP of protactinium obtained with the analytical method as described in this work. The uncertainty of the IP is given as the standard deviation of the averaged energies. This extracted IP lies well within the uncertainty range of the expected IP value of 49000(110) cm^{-1} by Wendt et al. [37].

Table 4.1: Schemes (i) - (iv)

	Level Density Collaps	Rydberg Correlation	Rydberg Correlation (zoom)
Scheme (i)	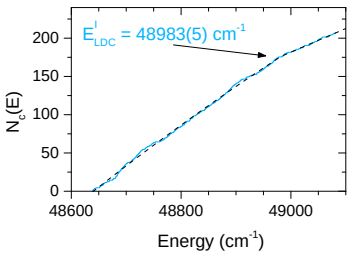	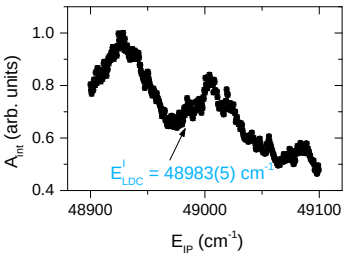	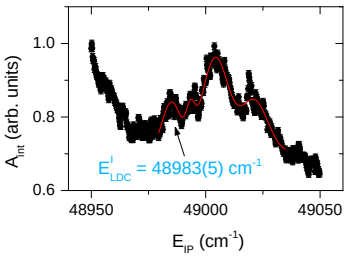
Scheme (ii)	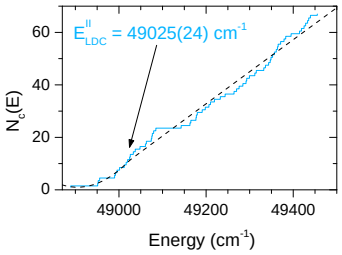	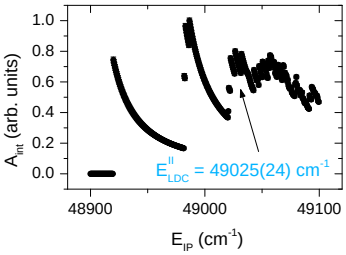	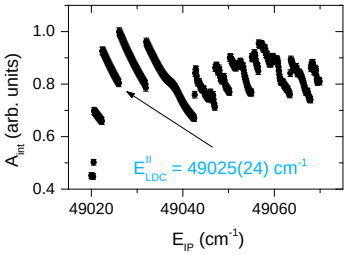
Scheme (iii)	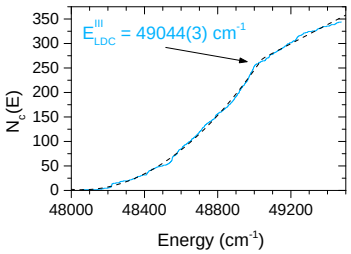	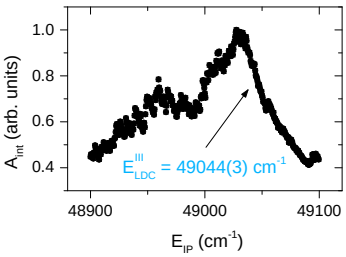	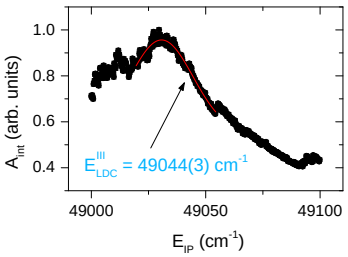
Scheme (iv)	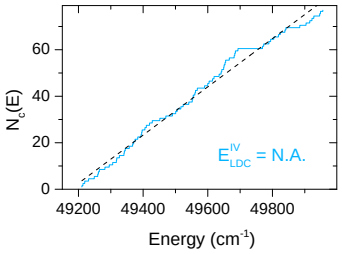	N.A.	N.A.

Table 4.2: Schemes (v) - (viii)

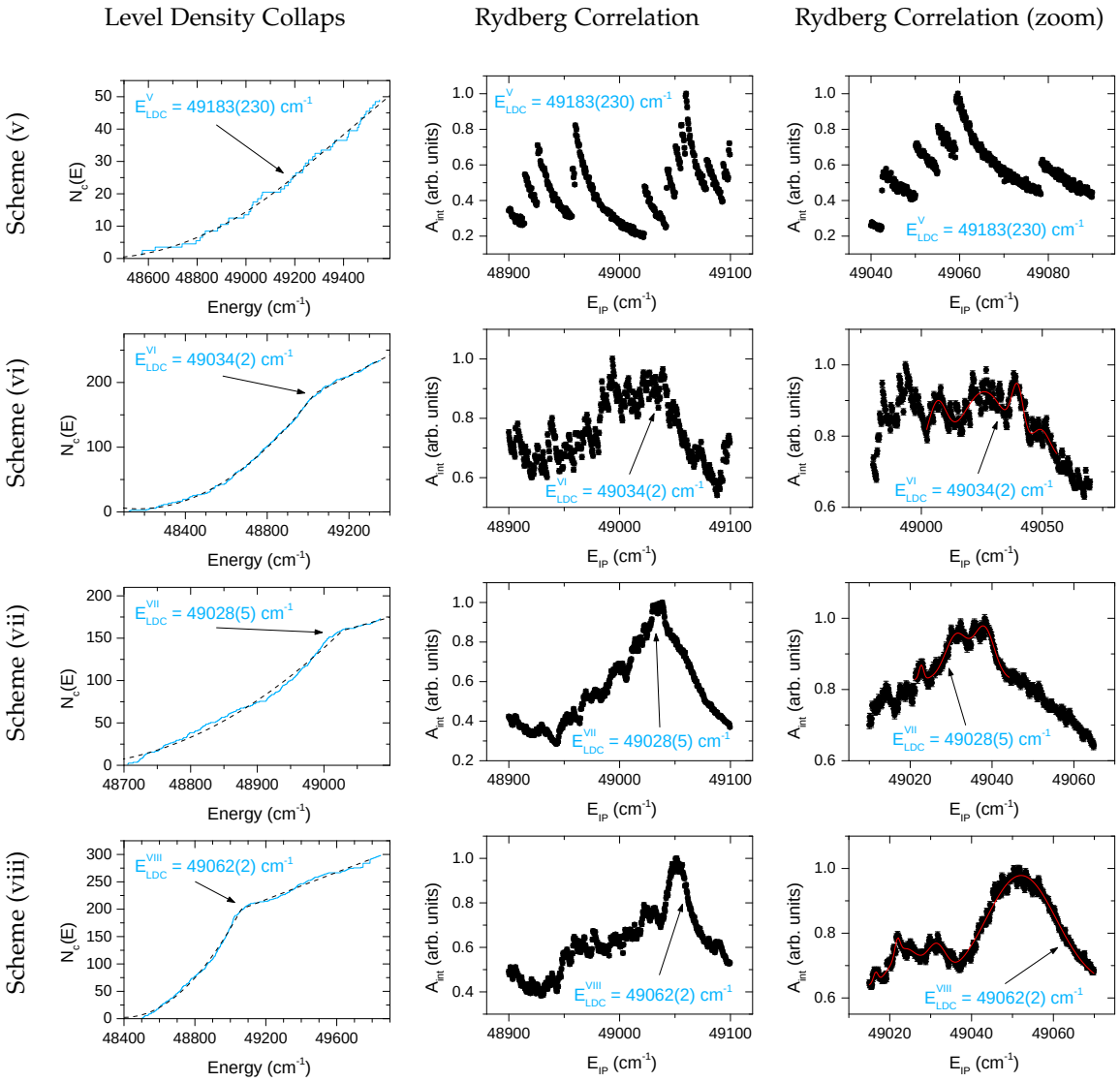

Table 4.3: Compilation of the results from the LDC and RC method for the eight protactinium excitation schemes which were studied. The uncertainty given for the LDC values is given by the fit error. The RC uncertainty is the half width at half maximum of the fitted peak structure. For the schemes where different RC peaks could be fitted, all relevant energy values are given. There, the bold values mark the energies matching the LDC values within their uncertainties.

Scheme	LDC (cm^{-1})	RC (cm^{-1})
(i)	48983(5)	**48985(5)**
		48993(2)
		49004(7)
		49021(7)
(ii)	49025(24)	N.A.
(iii)	49044(3)	**49031(16)**
(iv)	N.A.	N.A.
(v)	49183(230)	N.A.
(vi)	49034(2)	49006(5)
		49026(11)
		49040(3)
		49050(4)
(vii)	49028(5)	**49023(1)**
		49031(3)
		49038(3)
(viii)	49062(2)	49017(1)
		49022(1)
		49024(4)
		49031(3)
		49052(10)

Chapter 5

Intrinsic quantum chaos within atomic protactinium

The exceptional complexity of the protactinium spectra as investigated in the previous sections leads to a well visible "chaoticity" within the spectra. Not only this subjective impression, but more an expected strong disturbance of the individual energy levels leads to the assumption of a truly chaotic electronic level structure for the protactinium atom. This prediction is thoroughly examined on the basis and theory of quantum chaos involving measures known from the theory of random matrices [53, 54]. The first subsection here introduces the basics of quantum chaos and few examples of its manifestation. It was aimed to present the physical concepts without the need of advanced mathematics, which would complicate this overview and can easily be found in detail elsewhere. The ideas and explanations given in the following are partly inspired by the lecture notes of T. Guhr [55] and the book by H.-J. Stöckmann [56] as well as by personal discussions with A. Buchleitner, B. Dietz, T. Guhr and F. Haake. Further relevant literature will be given later in this chapter. The derivation of the contiguities, which required a precise analysis of the protactinium spectra, are described in publication IV featuring the main part of this chapter.

5.1 Quantum chaos

5.1.1 Access through classical mechanics

In classical physics, unlike the impressions given in most classical mechanics lectures, most systems existing in nature are chaotic. The definition of a chaotic system lies in its non-integrability. Obviously, a system called non-integrable if it is not analytically or numerically integrable; i.e. a conservative Hamiltonian system is integrable as long as it has as many independent constants of motion as it has degrees

of freedom. This means the constants of motion have to Poisson commute pairwise and every conservative system – we focus on conservative systems within this work – with only one degree of freedom is *per definitionem* integrable since the conservation of energy is the one necessary constant of motion. With increasing complexity, more constants of motion are getting relevant. The three dimensional Kepler problem with its constants of motion (total energy $E = H(\vec{q},\vec{p})$, angular momentum $\vec{L}^2$, its projection L_z, and the Runge-Lenz-Vector $\vec{M} = \frac{1}{m}\vec{p} \times \vec{L} - \frac{\kappa}{r}\vec{r}$) is an example that is even over-integrable.

While for integrable systems the equation of motion leads to a stable solution under small perturbations the same small perturbations lead to instabilities or divergent integrals for the solutions of the (Hamiltonian) equations of motion for non-integrable or chaotic systems. Such instabilities can be easily visualized with a system of three defocusing elements, e.g. disks in the unit plane, like it is depicted in Fig. 5.1. The lines may be for example the trajectories of ideally reflected billiard balls or light rays. In this setup, strong deviating trajectories result due to only slight perturbation of the input parameters.

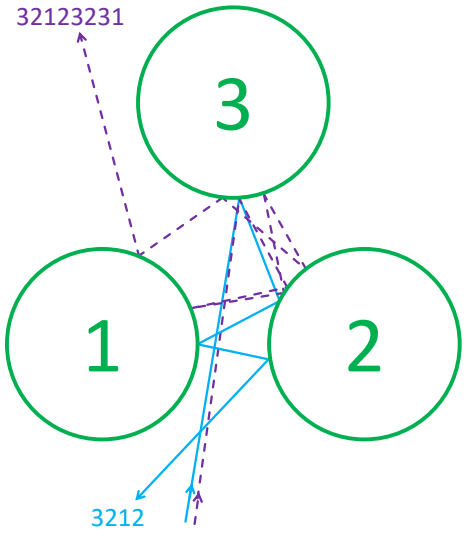

Figure 5.1: Instabilities of neighboring trajectories within a system of three disks in the unit plane under small perturbations of the input parameters. The number chains denote the specific path of the trajectories. Adapted from [55].

Hamiltonian systems like the one in the example above are deterministic despite their chaotic properties. That means, as long as the input parameters in phase space and the Hamiltonians are known, every trajectory can be calculated exactly at any time. Additionally, these trajectories are explicit, what is given by the theorem of Picard and Lindelöf [57], and, moreover gives the explanation for the non-crossing of trajectories in phase space. If trajectories could cross, the crossing point could be taken as starting point and the trajectory could never know which path to take from

there. This would be in complete contradiction to the uniqueness of the trajectories in phase space. Having said this, it becomes obvious, that the herein discussed chaos is a "deterministic chaos".

Chaotic systems are classified according to their emphasis of chaos. Systems that are generally accepted as chaotic systems are called K-systems after the mathematician Andrey Kolmogorov [58]. One specific illustrative property pf K-systems is that the trajectories in phase space are exponentially departing from their neighboring one once they came close to each other. This property holds for the mean so that trajectories can proceed some time next to each other before diverging, but the very most depart quickly after approaching. An example for visualizing this "repulsion", even though not visualized in phase space, is the chaotic double pendulum. Imagine the trajectory the outer end of the second arm describes: most of the time, it is departing from its prior path very quickly and in arbitrary shape, direction and amplitude. Fig. 5.2 shows an exemplary trajectory of the second arm of a double pendulum.

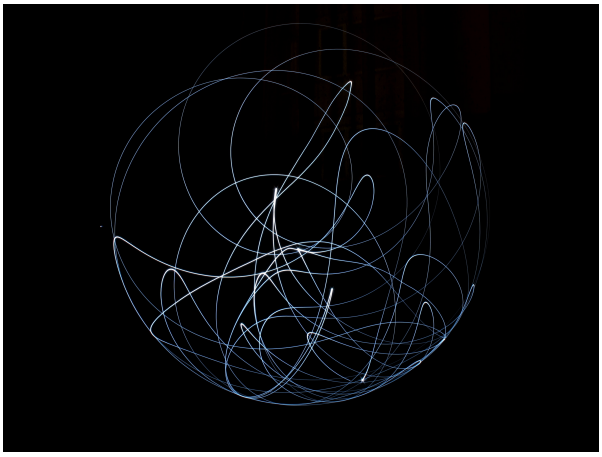

Figure 5.2: Trajectory of the outer and of the second arm of a double pendulum [59]. The chaotic path arbitrarily changes direction and amplitude, even though it is deterministic.

Specific K-systems showing the strongest chaotic properties are the so-called Bernoulli systems after the famous Swiss mathematician Jacob Bernoulli. Their supplementary property is that the exponentially departing phase space trajectories are producing perfect randomness, although still deterministic. This can be imagined as follows [55]: At all times, phase space is divided into small cells numbered with integers from 1 to n as shown in Fig. 5.3. As time evolves, a trajectory passes different cells described by a series of numbers, i.e. $\{6, 2, 7\}$. For Bernoulli systems, these numbers are distributed as produced by a perfect random number generator. This equals the production of perfect randomness out of a deterministic propagation of time.

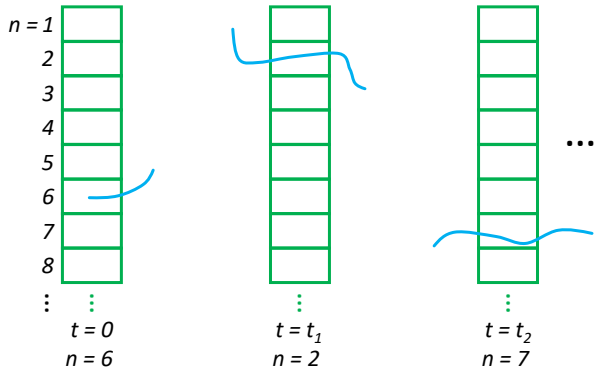

Figure 5.3: Phase space and trajectory of a Benoulli system. The phase space is divided into small cells and the trajectory acts as a perfect random number generator by passing the numbered cells. For more information see text. Adapted from [55].

Billards are often regarded as ideal examples of chaotic (Bernoulli) systems for research and teaching purposes and shall also act herein as examples. First of all, a Billiard is a two-dimensional domain with a closed curve acting as border. Inside the area, a particle, i.e. the "Billiard ball", can move without friction and is ideally reflected on the border. No further requirement on the shape of the closed border is necessary. Rectangle, circle or ellipse are examples for integrable, non-chaotic billiards. They have symmetries and therewith resulting constants of motion for at least every degree of freedom, which are (figures adapted from [55]):

- Rectangle
  Besides the total energy, the absolute values for the two components of the momentum $|p_x|$ and $|p_y|$ for both directions $\vec{x}$ and $\vec{y}$.

- Circle
  Total energy and the total angular momentum relative to the circle center.

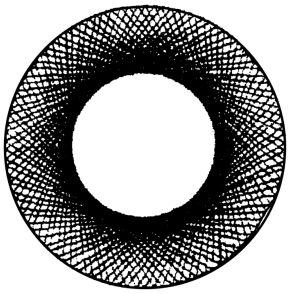

- Ellipse
  Total energy and the product of the two angular momenta relative to the two focal points $\vec{L_1}\vec{L_2}$.

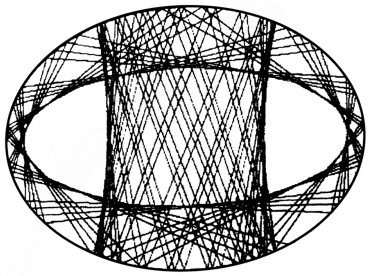

There are endless possibilities to create a chaotic system from a former regular billiard, by simply reducing the number of symmetries to a number smaller than the degrees of freedom. Three examples shall be given, adapted figures from [55, 60]:

- Sinai Billiard
  The momentum constants of motion of the rectangle billiard can easily be destroyed for example by placing a defocussing element like a circle inside the rectangle. In the resulting Sinai billiard, named after the Russian mathematician Yakov Sinai, the trajectories of the particle are defocused resulting in the exponential repulsion within this Bernoulli system.

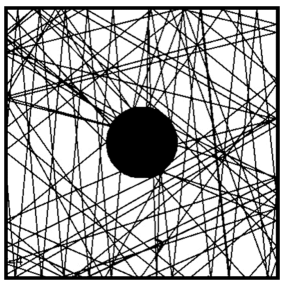

- Bunimovich Stadium
  Stretching the circular billiard by inserting straight parts between the two half circles destroys the radial symmetry and thus the angular momentum constant of motion. The Bernoullian chaos of this so-called Bunimovich stadium, after

the Russian mathematician Leonid Bunimovich, results not from a defocussing of the trajectories but from over-focussing similar to an unstable laser resonator.

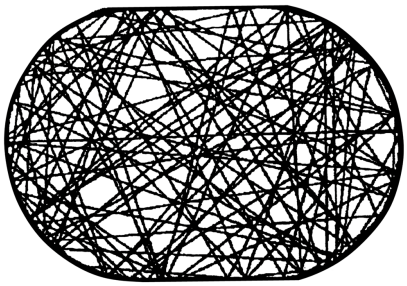

- Africa Billiard
  The Africa billiard – named Africa, because some representations look similar to the continent – is a more generalized chaotic billiard initially investigated by Berry and Robnik in 1986 [61]. It shall underline, that almost every thinkable billiard is chaotic while regular ones are very exceptional.

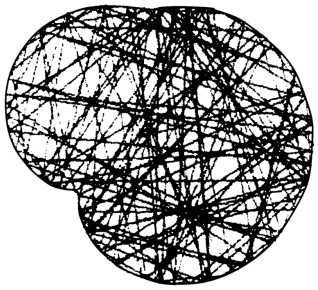

Please note, even though these examples are completely chaotic Bernoulli systems, stable regular or periodic trajectories are possible and allowed. One very simple example is a particle bouncing straight back and forth from the lower to the upper boundary in the Sianai billiard just next to the defocussing element. Actually there are countable infinite ways to realize such trajectories, but there are much more chaotic ones, namely of uncountable infinite number [55]. Additionally, in most natural chaotic systems chaotic and regular structures can coexist. This feature will be investigated later on in this work.

5.1.2 From classical to quantum chaos

Billiards are very useful in many aspects. With them even the transition from classical chaos to quantum chaos can be easily illustrated. One has just to replace the particles for example by electromagnetic radiation like microwaves or laser light to observe chaos within quantum mechanical systems. There, the billiard is nothing else than a arbitrarily shaped resonator. To start one step earlier, Bohr formulated in his correspondence principle, that classical mechanics is correct for macroscopic systems in the similar way as quantum mechanics for microscopic systems [62].

Consequently, quantum theory has to merge asymptotically into classical theory for large quantum numbers [55]. From this we can infer, that every quantum chaotic system has its classical analog – as for the billiard example.

Unfortunately, the simple concept of exponentially departing phase space trajectories is not applicable in quantum mechanics because of Heisenberg's uncertainty principle, which prevents the simultaneous measurement of position and momentum for a quantum particle. Nevertheless, the requirement for an integrable system remains: Like in the classical analog, a quantum mechanical system is integrable and therewith non-chaotic and fully solvable, if it has at least one constant of motion for every degree of freedom. In quantum mechanics, the classical constant of motion is replaced by its operator and the Poisson bracket by the quantum mechanical commutator. Once the number of degrees of freedom exceeds the number of constants of motion, the system is no longer integrable, thus resulting in chaotic behavior. Instead of phase space investigations – they are not applicable anymore as mentioned above – a different measure for quantifying chaotic behavior is needed. Therefore the focus lies now on the so-called spectral statistics, the properties of quantum spectra. Here, not a single spectral component, e.g. a resonance or energy level, is investigated, but the statistical interplay between all of them. For atomic systems, interestingly, the expected correlations appear only for spectra or level sets showing identical "good" quantum numbers of total angular momentum and parity [63].

5.1.3 Random matrix theory

In the 1950's Wigner was concerned with investigations on spectra of neutron scattering resonances. Due to the complexity of these spectra he started to describe the spectra according to their statistical properties. He studied the properties of the nowadays well established random matrix theory (RMT)[1] and proved that the spectral statistics of nuclear resonances behave identical to the Gaussian orthogonal ensemble (GOE) of the RMT [64, 65]. Here, the eigenvalues of many large GOE matrices form the complement to nuclear resonances. For the detailed mathematical background and the generation of the eigenvalues of the different ensembles, the reader is referred to more specialized books on this topic, in particular the book by M.L. Mehta [53]. In this place it shall just be mentioned, that the GOE matrices are invariant under orthogonal transformations and the entries of the symmetric matrices are real and random, but follow a Gaussian distribution.

An analog to the repulsion of trajectories in classical chaotic systems can also be found in the case of GOE statistics: In RMT the eigenvalues are "repelling" each other. This correlation can be quantified with different measures. But before these measures can be applied, the eigenvalues have to be "unfolded". This unfolding

[1] The RMT appeared already in the 1930's in mathematical statistics due to the work of Hsu, Wishart and others, but took not much attention until Wigner connected it to the field of nuclear physics [53].

is necessary in order to make the sequence of values independent from the specific eigenvalue density at any position in the sequence. After a proper unfolding process, measures with different correlation lengths can be investigated. The three most common measures shall be briefly mentioned here:

- Nearest neighbor spacing distribution
  This gives the "repulsion" of the nearest neighboring eigenvalues and thus is the measure with the shortest possible correlation length.

- Number variance $\Sigma^2(L)$
  Long-range measure, which is comparable with an error square depending on the correlation length L.

- Spectral rigidity $\Delta_3(L)$
  Most common long-range measure, which is comparable with an χ^2 measurement depending on the correlation length L.

The measures and the unfolding process are addressed in full detail in the publication *Intrinsic quantum chaos and spectral fluctuations within the protactinium atom*.

Until today, no proof is found, that the statistics as inferred from random matrix theory should be expected for every chaotic system. Nonetheless, every investigation, from billiards and quantum billiards over complex nuclei and atoms to ultracold gases or quartz oscillations, revealed significant coincidence with GOE statistics. This inspired Bohigas, Giannoni and Schmit in 1984 to their famous conjecture, that, due to its importance, shall be given here in full [66]:

"Spectra of timereversal-invariant systems whose classical analogs are K systems show the same fluctuation properties as predicted by GOE (alternative stronger conjectures that cannot be excluded would apply to less chaotic systems, provided that they are ergodic). If the conjecture happens to be true, it will then have been established the universality of the laws of level fluctuations in quantal spectra already found in nuclei and to a lesser extent in atoms. Then, they should also be found in other quantal systems, such as molecules, hadrons, etc."

This statement initiated a huge hype in quantum chaos research [56] and thus, the conjecture is probably the most often verified statement in chaos research. The following investigation in the protactinium atom regarding quantum chaos also relies on the correctness of the universality of the GOE statistics. Beside several examples of different manifestations of quantum chaos given in the publication, almost every atomic or nuclear system – except for hydrogen – reveals chaotic properties. For all these systems there is a very limited number of quantum numbers available for a much larger number of degrees of freedoms of nucleons or electrons. Similar as for billiards, even a hydrogen atom can "be made" chaotic if the number of constants

of motion is reduced via symmetry breaking – e.g. a strong magnetic field destroys the spherical symmetry of the atomic system and the angular momentum no longer is a constant of motion anymore [67]. It must be mentioned, that the transition from regular to chaotic behavior need not to be abrupt like in the classical billiard, which is either integrable or fully chaotic [67]. In a complex many-body system regularity and chaos can coexist and the amount of both can vary arbitrarily. However, the conjecture, that the chaotic behavior increases with excitation energy, e.g., in an atomic system should be pointed out here, but still lacks any proof.

As a last point before the quantum chaos research on the atomic protactinium is presented, an attempt of a qualitative explanation of the level repulsion in atomic systems, which is responsible for all the spectral correlation measures, shall be given: The regular level structuring is disturbed due to a residual interaction. This disturbance causes the repulsion of levels that can easily be seen in the nearest neighbor distribution of energy levels. The residual interaction may be reducible to the chaotic mixing of several thousands of possible electronic eigenstate configurations ($\approx 3 \cdot 10^5$ in Pa). In quantum mechanics, this can be interpreted as overlap of wave functions for all the different possible configurations. A non-vanishing probability results, that the arising "compound" level contains part of the same wave function as the adjacent one. For close lying energy levels, this leads to a strong repulsion of these states caused by Pauli's exclusion principle.

5.2 Publication: Intrinsic quantum chaos and spectral fluctuations within the protactinium atom

The last article of this work was published in August 2018 in *Physical Review A* together with the previous publication III. Besides the IP extraction in Sec. 4, it forms the second analytical research topic derived from the spectroscopic data of the protactinium measurements. The main objective of this article is the proof of full expression of quantum chaos within the protactinium atom. Additionally, it is investigated how variations in the ratio of energy levels with different total angular momentum or missing levels influence the spectral statistics. These findings are compared with ideal level sets from RMT.

Because the field of quantum chaos was completely new for the candidate as well as for his research group LARISSA, lots of efforts were invested for gaining enough knowledge to seriously contribute to this research area of sophisticated theoretical depth. The thesis author and first author of the publication carried out the entire analysis and also prepared the manuscript, while the co-authors supported the experimental work and further consultatively contributed to this endeavor.

Intrinsic quantum chaos and spectral fluctuations within the protactinium atom

Pascal Naubereit,[1,*] Dominik Studer,[1] Anna V. Viatkina,[2] Andreas Buchleitner,[3]
Barbara Dietz,[4] Victor V. Flambaum,[2,5] and Klaus Wendt[1]
[1]*Institute of Physics, University of Mainz, 55128 Mainz, Germany*
[2]*Helmholtz Institute, University of Mainz, 55128 Mainz, Germany*
[3]*Physikalisches Institut, Albert-Ludwigs-Universität Freiburg, 79104 Freiburg, Germany*
[4]*School of Physical Science and Technology and Key Laboratory for Magnetism and Magnetic Materials of MOE, Lanzhou University, Lanzhou, Gansu 730000, China*
[5]*School of Physics, University of New South Wales, Sydney 2052, New South Wales, Australia*

(Received 18 May 2018; published 10 August 2018)

Recently, spectroscopic investigations of the protactinium atom applying resonant laser ionization spectroscopy revealed high-resolution data of the single-excitation spectrum of protactinium, reaching slightly beyond the first ionization potential [P. Naubereit *et al.*, preceding paper, Phys. Rev. A **98**, 022505 (2018)]. The more than 1500 recently detected energy levels contain several complete sequences of levels. In this work we study the spectral fluctuations of these data exhibiting clear signatures of intrinsic quantum chaos within the protactinium atom. In order to obtain an estimate on possibly missing levels, simulations were performed based on large ensembles of random matrices from the Gaussian orthogonal ensemble. Our experimental results show that tabulated data in the literature are far from completeness and atomic structure calculations severely underestimate the density of states in the spectral range of highly excited states. However, the statistical analysis of our data as well as of the data from literature and calculations predict a level statistics close to that of fully developed chaos at energies well below the single-ionization threshold.

DOI: 10.1103/PhysRevA.98.022506

I. INTRODUCTION

As much as classical systems, like, e.g., the double pendulum, can exhibit a transition from regular to chaotic dynamics, the spectral properties of quantum systems can change drastically [1]. This is well established by now both theoretically and experimentally for few-degrees-of-freedom systems [2–11]. In contrast, evidence for quantum chaos in systems existing on higher-dimensional (classical) phase spaces which also have a much more intricate topology, giving rise, e.g., to Arnold diffusion [12–15], and likely are at the origin of many-body localization [16,17], is rather scarce, with only a few systematic results [18–24] so far. This fact is due to the unfavorable scaling properties of the density of states with increasing excitation energy, accompanied by strong coupling between the various degrees of freedom. On the theoretical as well as on the experimental side, this defines substantial challenges for the resolution of the relevant spectral structures [7]. Atomic many-body systems constitute ideal, naturally occurring test cases for such proliferation of complexity, where the generic presumption holds that the chaotic proportion of phase space increases with the excitation energy, while an unambiguous designation of the demarcation line between regularity and chaos has so far remained elusive [15,20,25–27]. In truly complex many-body systems, e.g., an actinide atom, the transition point from regularity to significant chaoticity is expected already at low excitation energies. A proof is pending, because complete high-resolution spectroscopic data from the ground state up to the first-ionization potential were and still are unavailable. Even for lighter elements, very few cases of investigation of intrinsic quantum chaos (IQC), meaning without outer influence of artificially applied electromagnetic fields or scattering processes by specific projectiles, in complex atomic systems are available [28–30].

Here we analyze spectral fluctuation properties in the recent spectroscopic data collected for protactinium and presented in Ref. [31] using as statistical measures the nearest-neighbor spacing distribution (NNSD), the number variance Σ^2, and the spectral rigidity Δ_3. For further explanations see Sec. II. According to the Bohigas-Giannoni-Schmit conjecture [32], the spectral fluctuation properties are universal and coincide with those of uncorrelated random numbers exhibiting Poisson statistics for classically integrable systems and with those of random matrices from the Gaussian orthogonal ensemble (GOE) if the classical dynamics is fully chaotic. For a proper analysis we have to deal with problems stemming primarily from missing or spurious levels. Therefore, large ensembles of random matrices from the GOE were generated and a certain fraction of eigenvalues was randomly deleted in order to simulate missing levels. The resulting statistics are compared to the experimental data.

Recently [31], about 1500 hitherto unknown resonances were detected in the bound spectrum of the Pa atom, covering selected energy ranges, different total angular momentum states, and both parities have been tabulated. An exemplary spectrum, corresponding to scheme (iii) of [31], is shown in the top panel of Fig. 1, covering excitation energies from below

*naubereit@uni-mainz.de

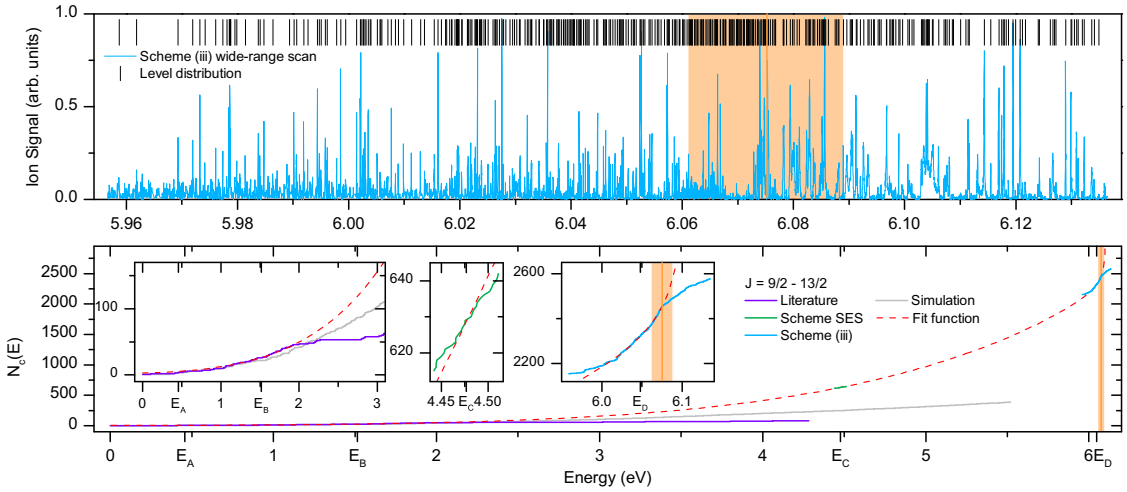

FIG. 1. The top graph shows the highly resolved excitation spectrum of protactinium for excitation scheme (iii) of [31], complemented by the corresponding level distribution (black lines above spectrum). The bottom graph shows the staircase functions for the cumulative number of resonances, as inferred from the literature (purple) [33], simulation (light gray) [34], and the present experimental data sets (green and blue) around E_C and E_D, respectively. The dashed red line represents the self-consistent fit to the spectral density over the entire energy range; see the main text for details. The orange vertical line in all plots indicates the estimated ionization potential, with its uncertainty range identified by the orange-shaded region [35]. For further explanations also on the three insets, see the text.

to slightly above the first ionization potential. The data of [31] serve as a basis for the analysis of intrinsic quantum chaos and its spectral characteristics in this highly complex atomic system.

II. LEVEL STATISTICS AND LEVEL DENSITY FLUCTUATIONS

A. Level density in general

Let us first compare the density of states of the experimental data, the available literature, and simulation data. The bottom panel of Fig. 1, together with the insets which zoom into three selected energy ranges, shows the cumulated number of energy levels

$$N_c(E) = \int_0^E \sum_i \delta(E' - E_i) dE' \tag{1}$$

as a staircase function of the excitation energy, with E_i the energy of the ith resonance. As explained in Ref. [31], our experimental data are limited to a range of three subsequent total angular momenta. Therefore, we took into account in the analysis of the simulated and the literature data only energy levels with $J = \frac{9}{2}, \ldots, \frac{13}{2}$. The apparent significant decrease of the level density just above the first ionization potential, as evident in the rightmost inset, can be explained by our experimental method: While resonances in the continuum still may bind all five electrons, many of these resonances are hidden by a continuum background due to broad autoionizing or ionic resonances, which becomes manifest in the top panel of Fig. 1 as a clearly visible broadening of the resonances above approximately 6.07 eV. This behavior was generally observed for all scans reaching beyond the expectation value of the ionization potential. A second reason is the termination of various Rydberg series converging towards the ionization potential.

For the simulation data, a loss of accuracy and completeness is anticipated already well below threshold, because only low-energy configurations had so far been included in these calculations [34]. In addition, the model neglects correlations between core and valence electrons, which are known to contribute substantially at higher excitation energies. Consequently, the experimental staircase function is expected to grow faster than the one predicted by the simulation, which exhibits an approximately quadratic energy dependence (see the gray line in the leftmost inset of the bottom panel of Fig. 1).

In order to compare the level densities of the experimental data [31] with those of the literature and simulation data and to localize strong deviations between them we performed a fit of $N_c^{\mathrm{tot}}(E)$ to the overall experimental density using the prediction for its average

$$\frac{d}{dE} N_c'(E) = \rho_0 e^{a\sqrt{E}} \tag{2}$$

for the density of states of an interacting many-body spectrum [29], which neglects Rydberg excitations of either one of the electrons. Thus, in the ansatz for $N_c^{\mathrm{tot}}(E)$, a phenomenological Rydberg term is included:

$$N_c^{\mathrm{tot}}(E) = N_c'(E, \rho_0, a) + r\sqrt{\frac{hcR}{E_{\mathrm{IP}} - E}}. \tag{3}$$

Here hcR is the mass-reduced Rydberg energy and ρ_0, a, r, and E_{IP} are free fitting parameters, where r could be interpreted as the number of Rydberg series involved and E_{IP} as the ionization potential. This procedure is legitimate since no chaotic perturbation is expected for high principal quantum numbers of single-electron Rydberg levels according to [36]. However, the data sets of scans in the energy range between 4.48 and 6.05 eV, denoted by SES (for second excitation step) and (iii), which are exemplarily considered from [31] and shown in the middle and right insets of the bottom panel

of Fig. 1, provide no information on how many levels lie below and between these associated energy ranges. To extract a consistent offset for the disjoint data sets, we fit $\partial N_c^{\rm tot}(E)/\partial E$ to the slopes of the cumulated density of states, as visualized in Fig. 1, within four predefined energy intervals E_A, E_B, E_C, and E_D, centered around the excitation energies 0.46, 1.52, 4.48, and 6.05 eV, respectively. These regions most optimally incorporate the different available data sets, stemming either from the literature at low excitation energies (E_A and E_B, where only the three J values studied in the experiment are accounted for) or from the experimental data of [31] at medium or high excitation energies (E_C and E_D). By this procedure, initially the offsets of the SES and (iii) scans were determined and the specific subsets of the three different data sets depicted in the three insets, now properly leveled, were fitted by $N_c^{\rm fit}(E)$. The resulting fitting parameters are reasonable: A value of $r = 16(6)$ for the different involved Rydberg series is realistic and $E_{\rm IP} = 6.11(1)$ eV matches the estimate of 6.075(14) eV for the ionization potential derived from systematics [35].

The resulting curve for the overall level density is shown as a red dashed line in the bottom panel of Fig. 1 as well as in the close-ups of the three insets. The comparison to the experimental data reveals three remarkable facts.

(a) The theoretical simulations, which only incorporate low-energy configurations, give correct and complete level densities up to excitation energies around 1.5 eV and slowly start to deviate at higher energies.

(b) Literature data appear to be complete up to energies around 2 eV, with a sharp cutoff at this value.

(c) The experimental data taken around E_C and E_D are well matched by the fit. Both data sets thus confirm the completeness of the levels detected in these energy ranges.

The issue of missing levels will be addressed Sec. III. Here "completeness" refers to unexpected deviations of the level density from its energy-dependent average, for example visible in the bottom panel of Fig. 1 for the literature data above 2 eV or for scheme (iii) above 6.07 eV. The slight deviations observed at the edges of both data sets (middle and right inset) are ascribed to a signal depletion at the edges of our laser scan ranges, due to decreasing laser power, as well as to the emerging continuum background discussed above for the energy range beyond the ionization threshold. Therefore, only the following parts of the individual data sets were employed in our subsequent analysis: For the even literature data a range of $0.00, \ldots, 2.00$ eV, for the SES scheme a range of $4.44, \ldots, 4.51$ eV, and for scheme (iii) a range of $5.96, \ldots, 6.08$ eV were evaluated.

B. Nearest-neighbor spacing distribution

Based on the above confirmation of the essential completeness of our experimental spectra in the inspected energy intervals, we can now proceed towards an analysis of the spectral structure of protactinium in terms of statistical measures commonly used in random matrix theory (RMT). We extract the nearest-neighbor spacing distribution, as one of the fundamental quantifiers of regularity-to-chaos transition in complex quantum systems [37], as area-normalized histograms of normalized, dimensionless energy spacings

$$s_i = \xi_{i+1} - \xi_i, \tag{4}$$

with the unfolded energy

$$\xi_i = N_c^{\rm fit}(E_i), \tag{5}$$

obtained by utilizing the smooth part of the staircase function, i.e., its fit function $N_c^{\rm fit}(E)$ [38]. Second-order polynomials serve as fit functions for the unfolding of all experimental level sets as well as of the numerically simulated spectral data from [34].

Random matrix theory predicts a Poisson distribution

$$P_{\rm P}(s) = e^{-s} \tag{6}$$

for the individual s_i in the limit of regular spectra, i.e., in systems of well-preserved quantum numbers, and a Wigner-Dyson distribution [39]

$$P_{\rm WD}(s) = \frac{\pi}{2} s e^{-(\pi/4)s^2} \tag{7}$$

in the limit of fully broken integrability, synonymous with the complete destruction of good quantum numbers, within subspaces defined by one specific value J of the total angular momentum [37]. Both these idealized limits are interpolated by the Brody distribution

$$P_{\rm B}(s,\eta) = a s^{\eta} e^{-b s^{\eta+1}}, \quad a = (\eta+1)b, \quad b = \Gamma\left(\frac{\eta+2}{\eta+1}\right)^{\eta+1}, \tag{8}$$

with Euler's Gamma function Γ. The Brody parameter η controls this interpolation, with the limiting cases $\eta = 0$ for the Poisson and $\eta = 1$ for the Wigner-Dyson distribution [40].

Since our experimental spectra are superpositions of three independent J manifolds, we furthermore need to account for the thereby induced convolution of distinct distributions. This can be achieved with the help of the superposition formula initially suggested by Rosenzweig and Porter [28]. Here we utilize Eq. (3.69) from [38], giving the spacing distribution $P_{\rm 3B}(s,\eta)$ for superpositions of three independent subspectra. In doing so, we make two assumptions.

(i) The level density in all three J manifolds is equal.

(ii) The manifolds exhibit the same energy dependence of $\eta(E)$.

A comparison with simulation and literature data validates both assumptions as reasonable first-order approximations [33,34]. A second interpolating function applicable to superimposed spectra is the Abul-Magd distribution [24,41]

$$P_{\rm AM}(s,f) = \left(1 - f + \frac{\pi}{2} Q(f) s\right) e^{-(1-f)s - (\pi/4)Q(f)s^2}, \tag{9}$$

with $Q(f) = 0.7f + 0.3f^2$. The parameter f of this description similarly approaches the Poisson distribution for $f \to 0$ and the Wigner-Dyson distribution for $f \to 1$, but the meaning is different as for the superposition of three Brody distributions: While the η parameter of the Brody convolution gives a hint at a close-to-GOE behavior of the three independent subspectra, the f parameter expresses a prediction for the number of superimposed fully chaotic GOE spectra. Thus, the number of independent GOE subspectra is given by $n = \frac{1}{f}$.

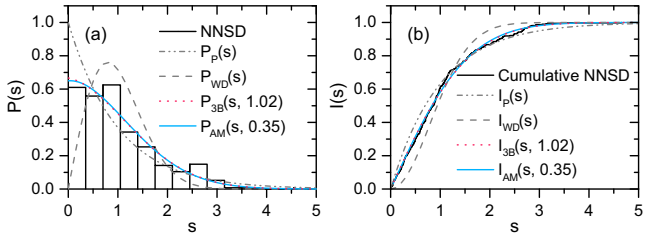

FIG. 2. (a) Nearest-neighbor spacing distribution $P(s)$ and (b) corresponding cumulative NNSD $I(s)$ for simulated data with $J = \frac{9}{2}, \ldots, \frac{13}{2}$. The Poisson and Wigner-Dyson distributions are shown as gray dash-dotted and dashed lines, respectively. The fitted Abul-Magd distribution is displayed as a blue line and the convoluted Brody distribution as a dotted red line.

The special case of three superimposed subspectra yields $P_{3B}(s, 1) \equiv P_{AM}(s, \frac{1}{3})$.

To determine the best-fit Brody parameter η or Abul-Magd parameter f, the maximum-likelihood (MLH) method [42] was used. This method is, in contrast to a least-squares-fitting method, completely independent from the binning procedure, since it is directly applied to the raw data. The uncertainty of η and f is conservatively approximated by the half-width at half maximum (HWHM) of the likelihood distribution.

Figure 2(a) shows an exemplary NNSD. Especially for small spacings and/or a small number of spacings, the cumulative nearest-neighbor spacing distribution (CNNSD)

$$I(s) = \int_0^s P(s')ds' \tag{10}$$

is more reliable for comparing the fits with the data. In Fig. 2(b) the CNNSD is shown. The NNSD is obtained from the simulated data with superimposed subspectra with $J = \frac{9}{2}, \ldots, \frac{13}{2}$. Besides the two fitted distributions P_{3B} and P_{AM} for the NNSD and I_{3B} and I_{AM} for the CNNSD, the curves for Poisson (P_P and I_P) and Wigner-Dyson (P_{WD} and I_{WD}) distributions are indicated as gray dash-dotted and dashed lines, respectively. The histograms are depicted for illustration; however, they were not used for the fitting procedure. The NNSD and CNNSD for the simulated data show a level repulsion close to that of chaotic GOE spectra. Both repulsion parameters $\eta = 1.02(30)$ and $f = 0.35(14)$ match the expected values of $\eta = 1$ and $f = \frac{1}{3}$, respectively, for a convolution of three GOE spectra very well. The rather large uncertainties of these values are caused by a broad likelihood distribution because the convoluted Brody distribution and the Abul-Magd distribution barely change in their shapes when varying the parameters η and f around a given value.

For an estimation of the quality of the fits for the CNNSD, the residuals $I_{3B} - I(s)$ and $I_{AM} - I(s)$ are shown in Fig. 3 as the difference between the resulting fit curves and the data. This form of presentation gives an idea of the shape of the NNSD and CNNSD by regarding the distribution parameters η and f and therefore a hint of the chaotic repulsion of the neighboring energy levels. In addition, it provides information on the quality of the individual fits of the CNNSD. Thus, in the following analysis only these residuals will be discussed when analyzing the level repulsion in the experimental data sets as short-range correlation.

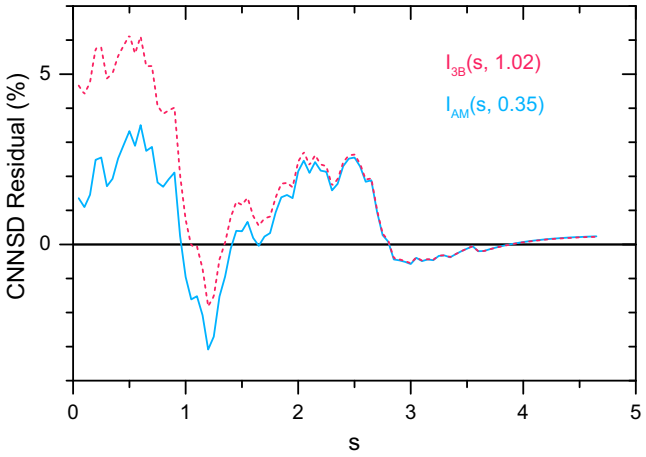

FIG. 3. Residuals of the fitted curves for the CNNSD. Here $I_{3B} - I(s)$ is given as a dotted red line and $I_{AM} - I(s)$ as a blue solid line.

For the experimental data, the NNSDs are conclusive only after accounting for missing levels. Because of that, we proceed similarly in the following two sections about the statistical measure's number variance and spectral rigidity and explain them by means of the simulated data first. The experimental measurements will be discussed afterward in detail in Sec. IV involving all statistical measures.

C. Number variance $\Sigma^2(L)$

The NNSD gives information on the repulsion of energy levels and shows correlations on the shortest possible scale, namely, on the scale of one or two mean spacings. Accordingly, the NNSD is sensitive with respect to the unfolding procedure, missing levels and the fitting procedure used for its description, however, by far not as sensitive as long-range correlations. Thus the NNSD itself does not serve as a significant measure for GOE or Poisson behavior. One additional measure for spectral statistics, which gives information on long-range correlations, is given by the variance $\Sigma^2(L)$ of the number $\nu(L)$ of unfolded levels in an interval with length L [38],

$$\Sigma^2(L) = \langle \nu^2(L) \rangle - \langle \nu(L) \rangle^2. \tag{11}$$

Here the angular brackets stand for a spectral average. Like a variance in stochastics, also the quantity $\Sigma^2(L)$ gives the mean-square deviation of the number of energy levels in an interval L from their mean L. For uncorrelated Poissonian spectra, $\Sigma^2_P(L)$ grows linearly with the correlation length L. For highly correlated GOE spectra, the variance $\Sigma^2_{GOE}(L)$ grows slower according to a logarithmic slope for large L. For our case of three superimposed subspectra, the spectral correlation is lower as in the GOE case. The resulting curve for $\Sigma^2_{3GOE}(L)$ can easily be calculated [38]:

$$\Sigma^2_{3GOE}(L) = \sum_{m=1}^{3} \Sigma^2_{GOE}\left(\frac{L}{3}\right). \tag{12}$$

Figure 4(a) shows the level number variance for the simulated data with $J = \frac{9}{2}, \ldots, \frac{13}{2}$ and the theoretical curves for the cases of Poissonian statistics, GOE statistics, and the statistics of three convoluted GOE spectra. The data matches the expected

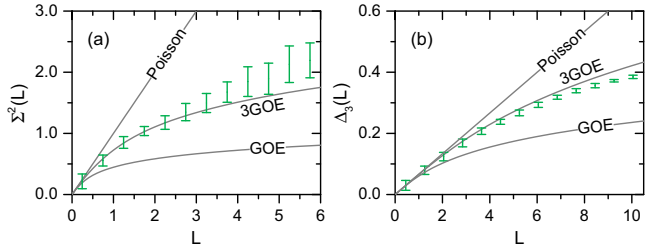

FIG. 4. (a) Number variance $\Sigma^2(L)$ and (b) spectral rigidity $\Delta^3(L)$ for the simulated data with $J = \frac{9}{2}, \ldots, \frac{13}{2}$. The error bars display the standard deviation of the binning process. The theory curves for Poissonian, GOE, and 3GOE statistics are given as gray lines.

curve for three superimposed GOE spectra (3GOE) perfectly up to a correlation length of $L \leqslant 3.5$. Only for higher L, the data points gradually start to deviate from the theoretical expectation of 3GOE, but still are significantly off from the Poissonian curve. This finding can be interpreted as GOE-like statistics for each of the involved J subspectra as already predicted in [34]. Nevertheless, another observable for long-range correlation statistics, the spectral rigidity $\Delta_3(L)$, will be investigated as a further preparation step for the data analysis presented in Sec. IV.

D. Spectral rigidity $\Delta_3(L)$

The spectral rigidity or Dyson-Metha statistic $\Delta_3(L)$ is defined as the least-squares deviation of the *unfolded* staircase function $\nu(\xi)$ from the best linear fit. Note that after proper unfolding the smooth part of the staircase function is by definition a straight line. The spectral rigidity $\Delta_3(L)$ is given as

$$\Delta_3(L) = \frac{1}{L}\left\langle \min_{A,B} \int_{\xi_s}^{\xi_s+L} [\nu'(\xi) - A\xi - B]^2 d\xi \right\rangle, \qquad (13)$$

where ξ_s defines the first unfolded level energy of an interval of length L [38,39]. Due to its definition, the spectral rigidity is comparable to a χ^2 depending on the correlation length L. Since Δ_3 is rather similar to Σ^2, the spectral rigidity can also be expressed as an integral transform of the number variance [38]

$$\Delta_3(L) = \frac{2}{L^4}\int_0^L (L^3 - 2L^2 r + r^3)\Sigma^2(r)dr. \qquad (14)$$

Similar to the number variance, for the Poissonian case of noncorrelated spectra (14) also leads to a linear expression of $\Delta_3^{\mathrm{P}}(L) = \frac{L}{15}$, while $\Delta_3^{\mathrm{GOE}}(L)$ for correlated GOE spectra again follows a logarithmic trend for large L. The resulting curve for three superimposed GOE spectra is simply calculated in analogy to Eq. (12) by [38]

$$\Delta_3^{\mathrm{3GOE}}(L) = \sum_{m=1}^{3} \Delta_3^{\mathrm{GOE}}\left(\frac{L}{3}\right). \qquad (15)$$

Figure 4(b) shows the spectral rigidity for the three superimposed simulated subspectra with $J = \frac{9}{2}, \ldots, \frac{13}{2}$ as well as the theory curves for Poisson, GOE, and convoluted GOE statistics. The rather small error bars again stem from the standard deviations of each bin. Like the number variance, also the spectral rigidity confirms chaotic GOE behavior of the simulated data for every involved J subset. The data fit the expected theory curve up to correlation lengths of $L \leqslant 5$ and start to slightly deviate above.

As described earlier in this section, the spectral rigidity is calculated from the number variance, which makes both quantities very similar by definition. Therefore, and because of its more smooth character due to the "smoothing" integral transform in Eq. (14), only $\Delta_3(L)$ will be utilized as a measure for long-range correlations of the energy levels in the following analysis of the experimental data.

III. MISSING LEVELS

For an accurate analysis of the experimental data sets it is mandatory to take into account the possibility of missing levels leading to incomplete spectra. The incompleteness of a spectrum will influence the spectral statistics leading to either more GOE-like or more Poissonian-like behavior. Imagine levels are "overlooked" due to the obviously finite spectral resolution of the experiment, where two or more levels may overlap, especially with increasing level density. Also resonances with intensities below the detection threshold may be missed. If levels are randomly extracted from the spectra, all statistical measures for the spectral properties of such incomplete spectra will show a displacement towards Poissonian statistics, simply because the correlation between levels is decreased. In our experiment, which utilizes resonance ionization spectroscopy, such situations cannot be avoided. In addition, especially as three J submanifolds are superimposed, the strength for transitions in subspectra of one specific J value might be significantly suppressed compared to the others. This causes the missing of levels in the respective J submanifold. In this case, the fluctuation properties would exhibit a displacement towards GOE-like behavior for every subspectrum, if the complete spectra exhibit GOE, because the correlations in each independent subspectrum seem to be higher if levels from only one J submanifold are missing. One possible method for characterizing the consequences for a certain number of missing levels in the experimental data is to randomly delete a specific percentage of levels from a set of levels from which we know that it shows GOE statistics.

A. Random matrices

The members of the Gaussian orthogonal ensemble are real symmetric matrices with Gaussian-distributed entries that are invariant under real orthogonal transformations [43]. We generated such matrices with dimension $N = 300$. In order to simulate the experimental situation, where the level sequences are composed of three independent subspectra corresponding to different values of J, we merged the eigenvalues of three random matrices into one sequence before applying the unfolding procedure. In order to improve the statistical significance we considered ensembles composed of five such sequences, thus yielding a set of 4500 levels.

Figure 5 shows the statistical measure for long-range correlation $\Delta_3(L)$ as well as the residuals from fitting the CNNSD with the convolution of three Brody functions and

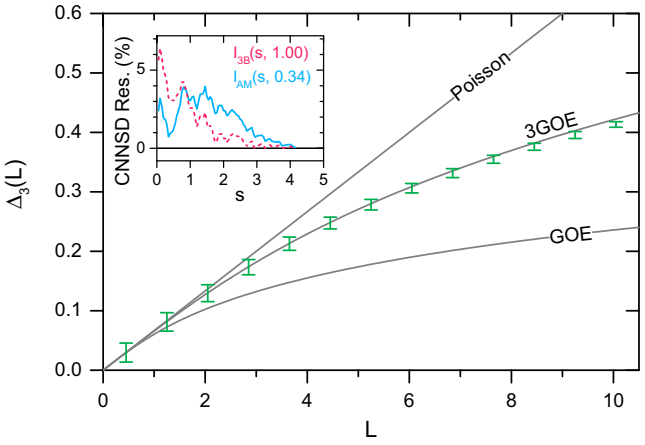

FIG. 5. Spectral rigidity for the RMT eigenvalues. The error bars display the standard deviation of the binning process. The theory curves for Poissonian, GOE, and 3GOE statistics are given as gray lines. The inset comprises the residuals of the CNNSD for the fitted Brody convolution (red dashed line) and the fitted Abul-Magd distribution (blue solid line).

the Abul-Magd distribution for this set of eigenvalues. In the inset of Fig. 5, a Brody parameter of $\eta = 1.00(23)$ and an Abul-Magd parameter of $f = 0.34(4)$ illustrate the expected repulsion of the nearest neighbors in a convolution of three GOE spectra. Even though the fits are lying at slightly higher values than the data, the small residuals also confirm the two extracted repulsion parameters and their uncertainties. In addition, the RMT data coincide perfectly with the theoretical results for the spectral rigidity. Thus, the dimension of the random matrices is large enough to ensure good agreement of the numerical simulations with the theoretical results for correlation lengths in ranges relevant for the experimental data.

B. Missing level statistics

As mentioned above, we have to take care of two types of missing levels. First, there may be randomly missing levels regardless of the subset, or in our case of the J value. Second, levels of a specific subset, or synonymous J manifold, might be suppressed at random and thus not detected. There actually exist exact analytical results for incomplete eigenvalue spectra of random matrices from the Gaussian ensembles [44] which can be generalized to the case of a superposition of three independent GOE matrices. However, because of the fact that we here have to deal with the above-mentioned cases of missing levels, the chosen way of using random matrix ensembles is more straightforward. In the following we will focus on the first case. The second case will be analyzed in detail in Sec. III C.

We simulated the first case by removing a specific percentage of randomly chosen levels from the total set of eigenvalues. To match the experimental situation, this has to be done before the unfolding process takes place. We created an ensemble of random matrices which will have slightly differing spectral properties. To extract the universal fluctuation behavior for a specific percentage of missing levels, we analyzed the distributions of the Brody and Abul-Magd parameters deduced

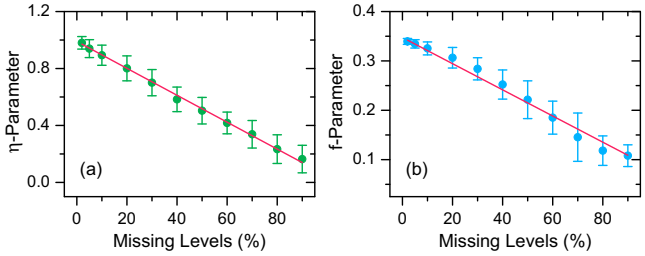

FIG. 6. Dependence of (a) the Brody parameter and (b) the Abul-Magd parameter on the percentage of missing levels regardless of the level subset. For each data point the distribution of the parameters for 100 different level sets has been evaluated. The red lines show linear fits to the data with fit parameters of (a) 0.9902(54) and −0.0095(1) and (b) 0.3474(21) and −0.0027(1) for the intercepts and slopes, respectively.

from fits to the NNSD of 100 level sets for various values of the percentage of missing levels. The resulting distributions are of Gaussian shape and the center positions together with the HWHM values as uncertainties are displayed in Fig. 6 for various percentages of missing levels reaching from 2% to 90%. Both parameters are linearly decreasing as a function of omission percentage. Thus, as expected, the correlations between the remaining neighboring levels are reduced with increasing fraction of missed eigenvalues.

For each fraction of missing levels a representative set of eigenvalues was identified for which a fit of the convoluted Brody and Abul-Magd distributions to the NNSD yields values of η and f as evaluated via Fig. 6. For these data sets also the dependence of the spectral rigidity $\Delta_3(L)$ on the fraction of missing levels has been obtained. Figure 7 shows the spectral rigidity for a choice of percentages of missing levels regardless of their J value, i.e., subset. The plots concerning that type of missing level are labeled with "All J missing." The data for the

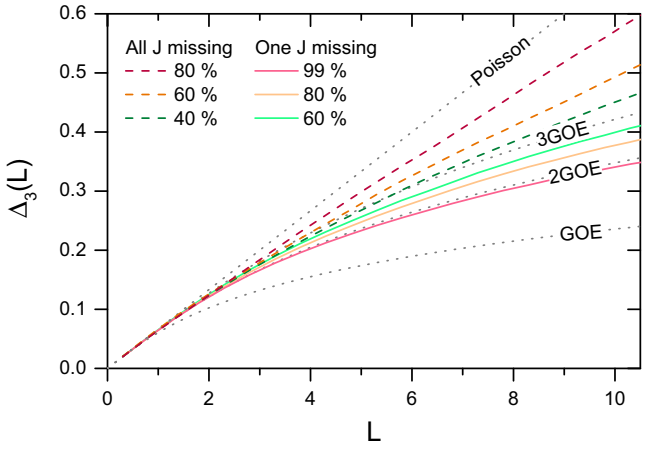

FIG. 7. Spectral rigidity for different percentages of missing levels from all subsets as colored dashed lines with increasing percentages from top to bottom. The colored solid lines represent the spectral rigidity for different percentages of missing levels from one certain subset with increasing percentages from bottom to top. The curves for Poissonian, GOE, 2GOE, and 3GOE behavior are given as gray dotted lines. For more information see the text.

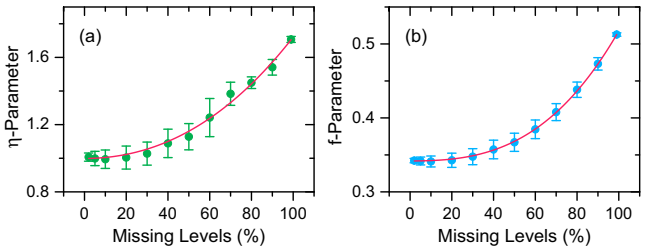

FIG. 8. Dependence of (a) the Brody parameter and (b) the Abul-Magd parameter on the percentage of missing levels in one specific level subset. For each data point the distribution of the parameters for 100 different level sets has been evaluated. The red lines show a cubic fit to the data.

different percentages of missing levels are given as differently colored dashed lines, while the curves for Poissonian and convoluted GOE behavior are given as gray dotted lines. The error bars are omitted in these graphs for the sake of clarity. The remaining graphs will be discussed in Sec. III C. As expected from the features of the NNSDs, the correlations between the remaining levels dwindle the more levels have been taken out, thus the corresponding spectral rigidity approaches the curve for Poissonian statistics accordingly. In contrast to the NNSDs, this approach does not take place in a linear manner: A clear deviation of $\Delta_3(L)$ from the 3GOE curve is observed not before approximately 30% of missing levels, at least within these rather short correlation lengths.

C. J suppression

Comparable to the approach in Sec. III B, here also specific amounts of levels are deleted, but now from only one subset in order to simulate the suppression of levels with a specific J value. We proceeded as in Sec. III B and thus obtained for the NNSD parameters a dependence on η and f as illustrated in Fig. 8. Unlike in Fig. 6, here the parameters η and f are well described by a cubic increase with an increasing number of missing levels.[1] Both starting at the values for NNSDs of three convoluted GOE spectra around $\eta = 1$ and $f = \frac{1}{3}$, the parameters remain fairly unchanged until about 30% of missing levels. From this point on the parameters are quickly approaching their final values of $\eta = 1.71(2)$ and $f = 0.51(0.2)$ at 99% missing levels. Of course, a Brody parameter larger than $\eta = 1$ is not very meaningful if a single spectrum is evaluated. Contrarily, it accentuates in our case the increase in level correlation due the reduced influence of one of the independent subsets. Also the Abul-Magd parameter delivers the expected value for a convolution of now only two GOE subspectra with $n = \frac{1}{f} \approx 2$.

Again, representative level sets are found with NNSDs predicted by the distribution of η and f as given in Fig. 8. From these representative sets the spectral rigidity $\Delta_3(L)$ was calculated for several percentages of missing levels. Figure 7 illustrates the results for this type of missing levels as graphs labeled with "One J missing." The theory curves for one, two convoluted, and three convoluted GOE spectra are given together with the curve for the Poissonian case as gray dotted lines. The analyzed data are given as solid lines, differently colored according to the number of missing levels. At first sight it is recognizable that the colored solid lines of Fig. 7 lie between the theory curves of 2GOE and 3GOE. Accordingly, the spectral rigidity $\Delta_3(L)$ shows the expected trend: Starting at the 3GOE curve, it approaches the 2GOE curve where it finally ends up. Note that the curve for 99% missing levels also fully agrees with the 2GOE curve within its uncertainty range, which was omitted here for the sake of clarity. That behavior corresponds to the increase of spectral correlation as seen before in the NNSDs of Fig. 8. Remarkably, $\Delta_3(L)$ does not change very much for percentages of missing levels below 40%–50%, like it was already suggested by the behavior of the NNSD parameters in Fig. 8.

Note that in a spectroscopic experiment, naturally a mixture of both types of missing levels will occur. As described in Secs. III B and III C, either type has a more or less opposite influence on the measures for spectral correlations. Thus, a specific ratio of the occurrence of both types might lead to a compensation of the effects on one of the measures for spectral correlations. Since the effects caused by missing levels are strongly nonlinear for the various statistical measures, we expect that a simultaneous cancellation for all of them is not possible. Hence, in the following analysis of experimental data, always the residuals of the fits for the CNNSD *and* the spectral rigidity are evaluated.

IV. SPECTROSCOPIC DATA

Based upon the statistical measures for spectral fluctuation properties introduced in Sec. II and the results on missing level statistics presented in Sec. III, we can now begin with a detailed analysis of the vast spectroscopic data of the protactinium atom. We will analyze several spectra composed of mainly three subspectra with individual total angular momenta covering different ranges of excitation energy and both parities.

A. Literature data

Data available in the literature [33] cover excitation energies from the ground state at 0 eV up to about 4.5 eV and both parities. We furthermore merged the levels with total angular momenta of $J = \frac{9}{2}, \ldots, \frac{13}{2}$ into one data set. Even-parity levels with an excitation energy above 2 eV have been omitted because of incompleteness indicated by the sharp cutoff observed in Fig. 1 in the left inset. For odd-parity levels we proceeded similarly by also omitting levels for energy ranges where obviously levels are missing according to the level density; in this case levels with excitation energies above 3.7 eV are neglected. Due to the low total count of only 46 energy levels,

[1]Cubic and quadratic fits have been tested, both with an fixed apex at 0% missing levels to guarantee a monotonically increasing function. Because of the worse adjusted R^2 for the quadratic fits of $R^2_\eta = 0.9972$ and $R^2_f = 0.9955$, respectively, in addition to larger residuals in comparison to the cubic fits—here the adjusted R^2 were $R^2_\eta = 0.9975$ and $R^2_f = 0.9999$, respectively—we decided to rely on the cubic fits. We presume that the dependence would be described best by a quadratic function if levels from two subsets, not one or all three, would be taken out. A proof for that conjecture as well as a reason for the found dependences is pending.

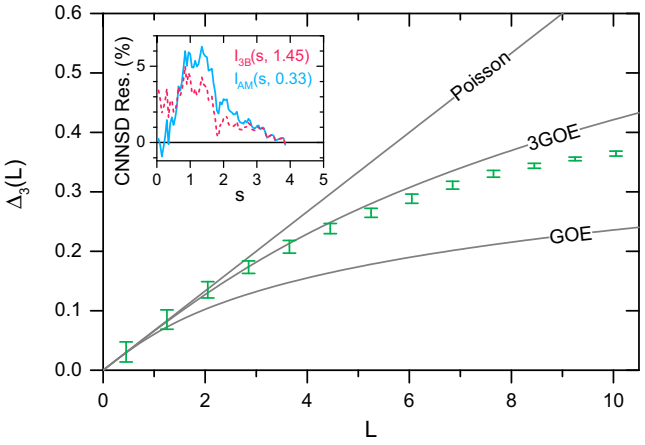

FIG. 9. Spectral rigidity for low-energy odd-parity levels of [33]. The error bars display the standard deviation of the binning process. The theory curves for Poissonian, GOE, and 3GOE statistics are given as gray lines. The inset comprises the residuals of the CNNSD for the fitted Brody convolution (red dashed line) and the fitted Abul-Magd distribution (blue solid line).

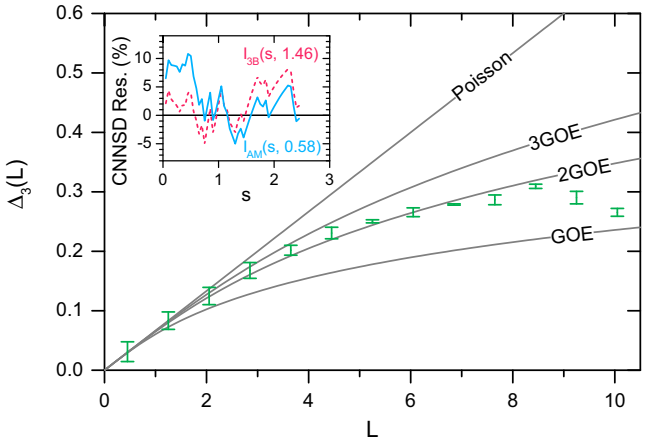

FIG. 10. Spectral rigidity for the midenergy even-parity levels of the SES scheme from [31]. The error bars display the standard deviation of the binning process. The theory curves for Poissonian, GOE, 2GOE, and 3GOE statistics are given as gray lines. The inset comprises the residuals of the CNNSD for the fitted Brody convolution (red dashed line) and the fitted Abul-Magd distribution (blue solid line).

the even spectrum is not significant and is thus only discussed in Appendix A.

Within the superimposed odd-parity spectrum, we analyzed a total of 217 levels. Figure 9 shows the results of this analysis. The parameters of the Abul-Magd function and the composition of three Brody functions of $f = 0.33(9)$ and $\eta = 1.45(49)$, respectively, predict 3GOE level statistics of these energetically low-lying energy levels. However, the MLH fit somewhat overestimated the Brody parameter. This is probably caused by the midsize level spacings, where both functions have problems to fit the data as visible in the residual plot of the CNNSD in the inset of Fig. 9. The spectral rigidity $\Delta_3(L)$ perfectly coincides with the 3GOE curve up to correlation lengths of about $L = 4.5$, which is comparable to the correlation length of the simulated data as analyzed in Fig. 4.

From these level statistics we learn two important things.

(i) The analyzed level sequence tabulated in [33] shows no apparently missing levels. This seems to be the fact also for the case of the even-parity levels analyzed in Appendix A.

(ii) Already at these very low energies (the spectrum reaches from 0.8 to 3.7 eV) the level fluctuations are not distinguishable anymore from 3GOE statistics, at least within the correlation lengths mentioned above.

Especially the second point is remarkable, as it affects a detailed investigation of the transition region into the chaotic regime. As pointed out in Sec. I, regularity and intrinsic quantum chaos are coexisting in a specific energy region until the chaotic behavior finally becomes prevalent above. In order to analyze the spectral statistics in this region, the spectrum has to be divided into several parts which need to be analyzed separately. Unfortunately, the transition is apparently located at such low excitation energies that the number of levels in the individual parts of the spectrum is too low to extract statistically significant information on the spectral properties of this region.

B. The SES scheme

In the following we discuss the spectral statistics of three representative spectra of even-parity levels identified in Ref. [31], covering different energy ranges and both types of missing levels; an example of spectral statistics for odd-parity levels is additionally given in Appendix B. The spectrum of the SES scheme of [31], also shown in Fig. 1, covers a medium-energy range around 4.5 eV. Since excitation starts from an excited level with $J = \frac{11}{2}$, the detected levels may have values for total angular momentum in the range $J = \frac{9}{2}, \ldots, \frac{13}{2}$. With 28 energy levels this spectrum constitutes the shortest level sequence evaluated here and thus suffers from low statistical significance, which also results in very large uncertainties. Nonetheless, the analysis of the observables for level fluctuations, as comprised in Fig. 10, reveals spectral statistical properties that can be well understood if missing levels are taken into account. Already the η and f parameters of the CNNSD, $\eta = 1.46(103)$ and $f = 0.58(29)$, respectively, predict an overestimation of chaotic behavior which would be caused by missing levels of one specific submanifold, even though the large residuals as shown on the inset of Fig. 10 suffer by the low statistical significance. Comparing the data in Fig. 10 with the curves in Figs. 7 and 8, one can estimate that a very high percentage of one J manifold of more than 80% must be missing due to the J suppression discussed in Sec. III C. Most important for the SES scheme is that the data clearly deviate from nonchaotic Poissonian behavior, which testifies again to the presence of IQC in the protactinium atom already at low excitation energies.

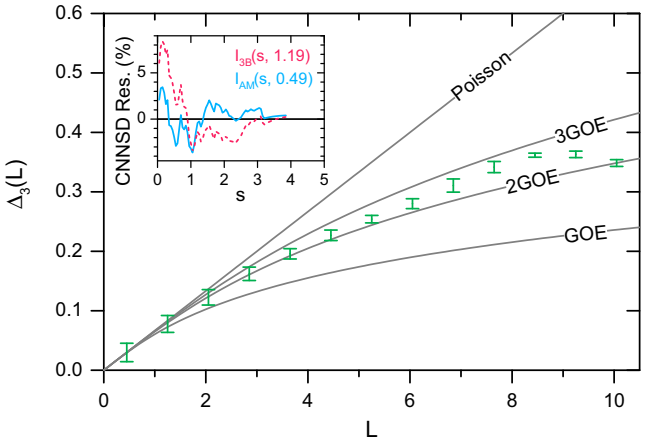

FIG. 11. Spectral rigidity for the high-energy even-parity levels of scheme (iii) from [31]. The error bars display the standard deviation of the binning process. The theory curves for Poissonian, GOE, 2GOE, and 3GOE statistics are given as gray lines. The inset comprises the residuals of the CNNSD for the fitted Brody convolution (red dashed line) and the fitted Abul-Magd distribution (blue solid line).

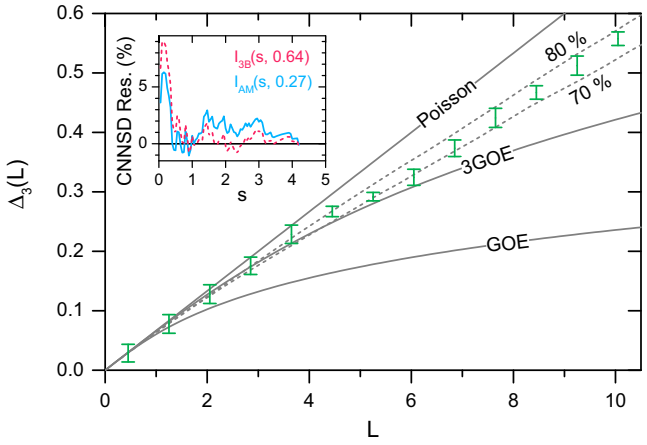

FIG. 12. Spectral rigidity for the high-energy even-parity levels of scheme (vi) from [31]. The error bars display the standard deviation of the binning process. The theory curves for Poissonian, GOE, and 3GOE statistics are given as gray solid lines. Additionally, the curves for 70% and 80% of missing levels regardless of their total angular momentum are included as gray dashed lines. The inset comprises the residuals of the CNNSD for the fitted Brody convolution (red dashed line) and the fitted Abul-Magd distribution (blue solid line). For more information see the text.

C. Scheme (iii)

The spectrum of excitation scheme (iii) in [31] with a total of 226 spectrally investigated energy levels involving total angular momenta of $J = \frac{9}{2}, \ldots, \frac{13}{2}$ is much more significant in terms of statistics. The spectral properties of this scheme covering high-energy regions just below the ionization potential are summarized in Fig. 11. The spectral rigidity follows the curve for 2GOE similarly to the SES midenergy scheme up to correlation lengths around $L = 5$. For higher L the spectral rigidity starts to slowly fluctuate between the curves for 2GOE and 3GOE. Regarding the inset of Fig. 11, the CNNSD is well described by the fitted distributions with $\eta = 1.19(44)$ and $f = 0.49(10)$, also predicting a slight overestimation of the GOE behavior of each involved J subset. Only for the smallest spacings, the residuals are somewhat larger, which can be explained by missing levels. Once again, the observables for the CNNSD and $\Delta_3(L)$ clearly deviate from Poissonian statistics consistently exhibiting an overestimation of GOE statistics due to suppression of transitions leading into levels with a certain total angular momentum J.

D. Scheme (vi)

For scheme (vi) from [31] with a total of 173 analyzed energy levels also lying in an energy range just below the ionization potential and having total angular momenta of $J = \frac{9}{2}, \ldots, \frac{13}{2}$, the situation regarding the spectral properties is consistent and convincing, although it is not satisfactory for the applied spectroscopic method: Inspecting the spectral fluctuation properties in Fig. 12, the results imply a high number of missing levels in this scan, here regardless of J. A Brody parameter of $\eta = 0.64(28)$ and an Abul-Magd parameter of $f = 0.27(11)$ already suggest a percentage of more than 30%−40% missing levels if compared to Fig. 6. In addition, the residuals depicted on the inset of Fig. 12 show strong deviation of both fitted distribution only for very small spacings, which is also clearly provoked by missing levels. The result for $\Delta_3(L)$ in Fig. 12 lies exactly between the two gray dashed curves for 70%−80% missing levels as evaluated in Sec. III B. The very long correlation lengths of this coincidence together with the consistency of the distribution parameters η and f, the corresponding residuals, and the evaluated spectral rigidity validates the applied methods of analysis. Despite the rather large amount of missing levels obtained in this excitation scheme (vi), a full expression of intrinsic quantum chaos seems nonetheless confirmed.

V. CONCLUSION AND OUTLOOK

We have analyzed several sets of energy levels of the protactinium atom concerning their spectral fluctuation properties. The sets are of different origins, stemming from the literature [33], calculations [34], and recent experimental data [31]. Since the experimental data were not separable into sets with only one total angular momentum J, all analyzed data, separable for J or not, were composed for incorporating the same range of J levels as the experimental data. Moreover, for the spectroscopic data, it was essential to investigate the influence of missing levels on the spectral fluctuations, which was performed accurately. Therefore, randomly levels were taken out either from the whole spectrum or only from one subspectrum of three superimposed submanifolds simulated by three GOE matrices in order to correctly simulate the experimental situations. In addition, the mathematical analysis of the statistical measures had to be customized for the special difficulty of nonseparability for the "good" numbers, or at least for the total angular momentum J.

As already suggested in [34], besides the short-range correlation of the therein investigated NNSD, $\Delta_3(L)$ clearly indicate agreement with GOE behavior. This was confirmed using the available data from the literature [33] for odd-parity

levels as well as even-parity levels with lower significance. For the experimental data recently obtained in [31], it was possible with extensive analysis of the missing level problem also to extract level statistics that coincide well with those of a composition of three independent GOE spectra. The spectral statistics for all cases studied strongly deviate from Poissonian statistics, or nonchaotic behavior, and therefore emphasize the prognosticated occurrence of IQC in the protactinium atom.

At excitation energies below 2 eV the energy levels available in the literature [33] already show chaotic level statistics. This means that the onset of chaos, or synonymously the transition point from regular to chaotic behavior, must be located at even lower energies. In such low-energy regimes, the level density is too small to extract the spectral properties of this transition region with high statistical significance. As a future prospect, one approach to account for the low number of energy levels is to combine several unfolded level sets with excitation energies centered in this region of different elements with comparable atomic properties, i.e., a similar number of open shells and active electrons.

For a quantification of the missing levels of either type, an empirical function that describes the influence of missing levels on the fluctuation laws would be the method of choice. Fitting such a function to the NNSD and the spectral rigidity of experimentally determined data sets could unveil even more details of the spectral properties of the underlying level subsets.

ACKNOWLEDGMENTS

The authors want to thank T. Guhr, F. Haake, and R. Heinke for many fruitful discussions. P.N. gratefully acknowledges the Carl-Zeiss-Stiftung, D.S. gratefully acknowledges the EU through ENSAR2 RESIST (Grant No. 654002), and A.V.V. and V.V.F. gratefully acknowledge the Australian Research Council and Gutenberg Fellowship for financial support. B.D. thanks the NSF of China for financial support under Grant No. 11775100.

APPENDIX A: SPECTRAL STATISTICS OF EVEN-PARITY LITERATURE DATA

Figure 13 shows the spectral statistics for the even-parity energy levels that can be found in the literature [33]. Even though the results are not significant due to too few levels (only 46) involved, the observables for the short-range correlation between the energy levels promise a full expression of chaos: While the parameters of the composition of three Brody functions and the Abul-Magd function of $\eta = 0.91(78)$ and $f = 0.31(21)$, respectively, are close to the ideal values of $f = \frac{1}{3}$ and $\eta = 1$ and thus already suggest GOE behavior, the spectral rigidity is more sensitive to non-GOE features. Here, similar to the short-range correlation due to their large uncertainties, also the spectral rigidity is not very conclusive, which is also confirmed by the rather large residuals in the inset of Fig. 13: Regarding small correlation lengths L, it might coincide with regular just as well as with 3GOE statistics. Only for larger L, the spectral rigidity starts to deviate more strongly from the Poissonian statistics. Despite the poor statistics, the results seem to be consistent with those for the odd-parity energy levels of [33] in Sec. IV A.

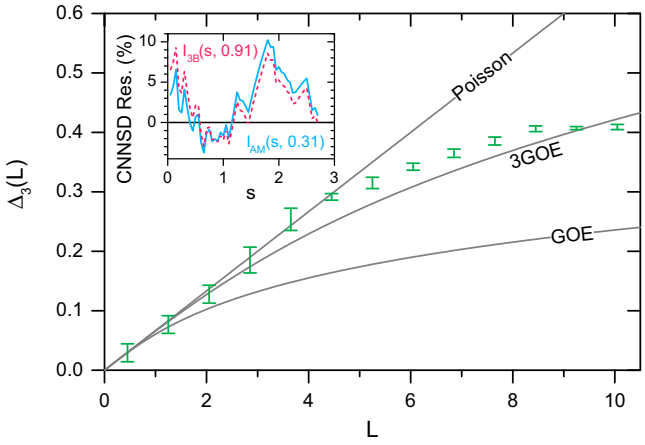

FIG. 13. Spectral rigidity for low-energy even-parity levels of [33]. The error bars display the standard deviation of the binning process. The theory curves for Poissonian, GOE, and 3GOE statistics are given as gray lines. The inset comprises the residuals of the CNNSD for the fitted Brody convolution (red dashed line) and the fitted Abul-Magd distribution (blue solid line).

APPENDIX B: SPECTRAL STATISTICS OF ODD-PARITY LEVELS FROM SCHEME (viii)

With scheme (viii) from [31], a spectrum with 168 odd-parity energy levels lying in the energy region just below the ionization potential is investigated regarding level correlations and spectral statistics. The corresponding observables for the spectral statistics, namely, the η and f parameters for fitting the CNNSD with the corresponding residuals and the spectral rigidity $\Delta_3(L)$, are comprised in Fig. 14. For the explanation of the results, the consideration of missing levels is again

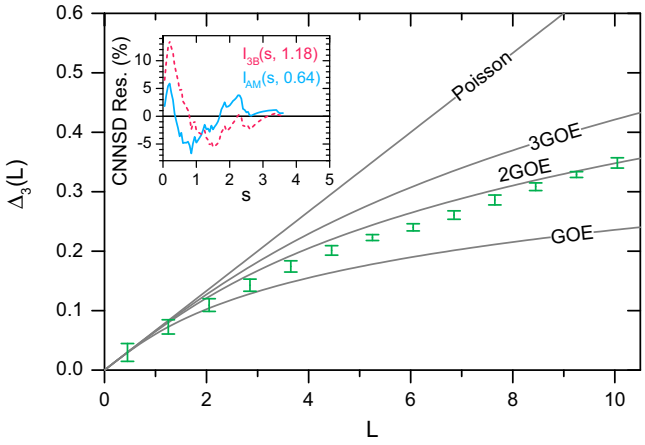

FIG. 14. Spectral rigidity for the high-energy odd-parity levels of scheme (viii) from [31]. The error bars display the standard deviation of the binning process. The theory curves for Poissonian, GOE, 2GOE, and 3GOE statistics are given as gray lines. The inset comprises the residuals of the CNNSD for the fitted Brody convolution (red dashed line) and the fitted Abul-Magd distribution (blue solid line).

mandatory. The spectral rigidity $\Delta_3(L)$ exhibits a behavior very close to the curves for 2GOE, which would be explained by the case of missing levels from only one J manifold. In addition, the results for the distribution parameters, which are with $\eta = 1.18(38)$ and $f = 0.64(13)$ close to a 2GOE behavior, testify to this overestimation of chaoticity due to the missing levels. Even though the residuals shown in the inset of Fig. 14 are at least for small spacings quite large, also here the spectral statistics clearly deviate from pure Poissonian behavior and therefore also these data seem to prove the quantum chaotical behavior of the protactinium atom.

[1] D. Delande, in *Chaos and Quantum Physics*, edited by M.-J. Giannoni, A. Voros, and J. Zinn-Justin, Proceedings of the Les Houches Summer School of Theoretical Physics, LII, Varenna, 1989 (North-Holland, Amsterdam, 1991).

[2] A. Holle, J. Main, G. Wiebusch, H. Rottke, and K. H. Welge, Phys. Rev. Lett. **61**, 161 (1988).

[3] H.-J. Stöckmann and J. Stein, Phys. Rev. Lett. **64**, 2215 (1990).

[4] H.-D. Gräf, H. L. Harney, H. Lengeler, C. H. Lewenkopf, C. Rangacharyulu, A. Richter, P. Schardt, and H. A. Weidenmüller, Phys. Rev. Lett. **69**, 1296 (1992).

[5] B. E. Sauer, M. R. W. Bellermann, and P. M. Koch, Phys. Rev. Lett. **68**, 1633 (1992).

[6] J. C. Robinson, C. Bharucha, F. L. Moore, R. Jahnke, G. A. Georgakis, Q. Niu, M. G. Raizen, and B. Sundaram, Phys. Rev. Lett. **74**, 3963 (1995).

[7] A. Buchleitner, D. Delande, J. Zakrzewski, R. N. Mantegna, M. Arndt, and H. Walther, Phys. Rev. Lett. **75**, 3818 (1995).

[8] H. Held, J. Schlichter, G. Raithel, and H. Walther, Europhys. Lett. **43**, 392 (1998).

[9] M. B. d'Arcy, R. M. Godun, M. K. Oberthaler, D. Cassettari, and G. S. Summy, Phys. Rev. Lett. **87**, 074102 (2001).

[10] S. Urazhdin, P. Tabor, V. Tiberkevich, and A. Slavin, Phys. Rev. Lett. **105**, 104101 (2010).

[11] K. Karremans, W. Vassen, and W. Hogervorst, Phys. Rev. Lett. **81**, 4843 (1998).

[12] M. C. Gutzwiller, *Chaos in Classical and Quantum Systems* (Springer, Berlin, 1990).

[13] J. von Milczewski, G. H. F. Diercksen, and T. Uzer, Phys. Rev. Lett. **73**, 2428 (1994); **76**, 2890 (1996).

[14] P. Schlagheck and A. Buchleitner, Physica D **131**, 110 (1999).

[15] N. N. Choi, M.-H. Lee, and G. Tanner, Phys. Rev. Lett. **93**, 054302 (2004).

[16] D. M. Basko, I. L. Aleiner, and B. L. Altshuler, Ann. Phys. (NY) **321**, 1126 (2006).

[17] *Many-Body Localization*, edited by J. H. Bardarson, F. Pollmann, U. Schneider, and S. Soudhi, special issue of Ann. Phys. (Berlin) **529**(7), 1700191 (2017).

[18] R. U. Haq, A. Pandey, and O. Bohigas, Phys. Rev. Lett. **48**, 1086 (1982).

[19] H. Alt, C. Dembowski, H.-D. Gräf, R. Hofferbert, H. Rehfeld, A. Richter, R. Schuhmann, and T. Weiland, Phys. Rev. Lett. **79**, 1026 (1997).

[20] T. Maier, H. Kadau, M. Schmitt, M. Wenzel, I. Ferrier-Barbut, T. Pfau, A. Frisch, S. Baier, K. Aikawa, L. Chomaz, M. J. Mark, F. Ferlaino, C. Makrides, E. Tiesinga, A. Petrov, and S. Kotochigova, Phys. Rev. X **5**, 041029 (2015).

[21] J. Madroñero and A. Buchleitner, Phys. Rev. Lett. **95**, 263601 (2005).

[22] G. Stania and H. Walther, Phys. Rev. Lett. **95**, 194101 (2005).

[23] L. Muñoz, R. A. Molina, J. M. G. Gómez, and A. Heusler, Phys. Rev. C **95**, 014317 (2017).

[24] B. Dietz, A. Heusler, K. H. Maier, A. Richter, and B. A. Brown, Phys. Rev. Lett. **118**, 012501 (2017).

[25] R. Püttner, B. Grémaud, D. Delande, M. Domke, M. Martins, A. S. Schlachter, and G. Kaindl, Phys. Rev. Lett. **86**, 3747 (2001).

[26] Y. H. Jiang, R. Püttner, D. Delande, M. Martins, and G. Kaindl, Phys. Rev. A **78**, 021401 (2008).

[27] H. Held and W. Schweizer, Phys. Rev. Lett. **84**, 1160 (2000).

[28] N. Rosenzweig and C. E. Porter, Phys. Rev. **120**, 1698 (1960).

[29] H. S. Camarda and P. D. Georgopulos, Phys. Rev. Lett. **50**, 492 (1983).

[30] V. V. Flambaum, A. A. Gribakina, G. F. Gribakin, and M. G. Kozlov, Phys. Rev. A **50**, 267 (1994).

[31] P. Naubereit, T. Gottwald, D. Studer, and K. Wendt, preceding paper, Phys. Rev. A **98**, 022505 (2018).

[32] O. Bohigas, M. J. Giannoni, and C. Schmit, Phys. Rev. Lett. **52**, 1 (1984).

[33] J. Blaise and J.-F. Wyart, *Energy Levels and Atomic Spectra of Actinides*, available at http://web2.lac.u-psud.fr/lac/Database/Contents.html (accessed 20 March 2018) (TIC, Paris, 1992).

[34] A. V. Viatkina, M. G. Kozlov, and V. V. Flambaum, Phys. Rev. A **95**, 022503 (2017).

[35] K. Wendt, T. Gottwald, C. Mattolat, and S. Raeder, Hyperfine Interact. **227**, 55 (2014).

[36] A. A. Gribakina, and G. F. Gribakin, J. Phys. B **29**, L809 (1996).

[37] F. Haake, *Quantum Signatures of Chaos*, Springer Series in Synergetics Vol. 54 (Springer, Berlin, 2013).

[38] T. Guhr, A. Müller-Groeling, and H. A. Weidenmüller, Phys. Rep. **299**, 189 (1998).

[39] F. J. Dyson and M. L. Mehta, J. Math. Phys. **4**, 701 (1963).

[40] T. A. Brody, Lett. Nuovo Cimento **7**, 482 (1973).

[41] A. Y. Abul-Magd and M. H. Simbel, Phys. Rev. C **54**, 1675 (1996).

[42] M. A. Jafarizadeh, N. Fouladi, H. Sabri, and B. Rashidian Maleki, Nucl. Phys. A **890-891**, 29 (2012).

[43] M. L. Mehta, *Random Matrices* (Academic, New York, 2004), Vol. 142.

[44] O. Bohigas and M. P. Pato, Phys. Lett. B **595**, 171 (2004).

Chapter 6

Conclusion

The four publications comprised in this cumulative thesis address a series of scientific topics, starting from experimental to more theoretical nature, all applying resonance ionization spectroscopy as general base. With this regard, the choice of *Resonance ionization spectroscopy of sodium Rydberg levels using difference frequency generation of high-repetition-rate pulsed Ti:sapphire lasers* as initial article had two scopes: The first was to verify and validate the method of RIS regarding Rydberg spectroscopy and the general approach and precision of the Rydberg analysis for extracting the ionization potential of an element. The second aspect of the article, somewhat less highlighted in the frame of this thesis, was the extension of the accessible wavelength range for RIS via establishing a difference frequency generation process for the Mainz Ti:sapphire lasers. For a proper validation of both aspects of the technique, the element sodium was the ideal candidate. It is an element with a very precisely known ionization potential and, more over, its very simple atomic level structure is perfectly suited for RIS. For the laser excitation, the famous 589 nm fine structure doublet was chosen, clearly lying in the DFG range of a Ti:sapphire laser. The task could successfully be mastered by performing RIS on both, the sodium D1 and D2 line applying an DFG-extended wavelength range and re-measuring the ionization potential with $E_{\mathrm{IP}}^{\mathrm{Na}} = 41449.455(6)_{\mathrm{stat}}(7)_{\mathrm{sys}}$ cm^{-1} in very good agreement with the precise literature value of $E_{\mathrm{IP}}^{\mathrm{Na}} = 41449.451(2)$ cm^{-1} [50,51].

The second article, co-authored by the author of this thesis, *Developments towards in-gas-jet laser spectroscopy studies of actinium isotopes at LISOL* explores an important part of the LARISSA collaboration network with regard to on-line RIS applications. Most importantly, it demonstrated the high specifications and broad capabilities of the novel in-gas-laser ionization and spectroscopy (IGLIS) technique and therewith paved the way for a number of follow-up studies in this field, see e.g. [32,33].

As main part of this thesis, the resonance ionization spectroscopy of protactinium is presented. This work included extensive and time consuming studies in the spectrum of this rare element as well as sophisticated analyses of the recorded atomic

spectra. Despite many complications and challenges which appeared during the handling of protactinium, *Excited atomic energy levels in protactinium by resonance ionization spectroscopy* comprises all information on the atomic data and the complex separation procedure of energy levels. The compilation of more than 1500 newly obtained energy levels in Pa I is given in the supplementary material to this article.

Since a determination of the ionization potential was impossible by just applying conventional evaluation techniques, the focus was shifted towards the development and understanding of refined theoretical methods for extracting the IP from ultra dense atomic spectra. In chapter 4 of this thesis two of such methods are derived and elucidated in detail. Named *Level Density Collapse* and *Rydberg Correlation*, both analytical techniques can be used to extract estimates for the ionization potential from atomic spectra. As shown, a combination of both methods gives a reliable IP value even for the very complex and strongly disturbed spectra as found in the case of protactinium. With the aid of these newly developed analytical methods it was finally possible to extract a consistent value for the ionization potential of protactinium from the different spectra, whereas only a very rough estimate from comparison with other actinides was known before. The newly found value of

$$E_{IP}^{Pa} = 49034(10)\ \mathrm{cm}^{-1} \tag{6.1}$$

lies perfectly within the uncertainty range of the earlier estimation of 49000(110) cm^{-1} by Wendt et al. [37]. Despite of its scientific relevance, a publication of this finding and the involved analytical methods is still pending due to time constraints during the finalization of the present work.

With the last topic of this thesis, a completely new field of research was worked out and established within the LARISSA group in Mainz. The more theoretical approach of investigating intrinsic quantum chaos is rather far from the central area of expertise within the group. Nonetheless, the studies aroused deep interest among specialists in chaos research. This was accompanied by the high visibility and long-standing expertise of the group around Prof. Dr. Klaus Wendt: Based upon several decades of experience in lasers and specifically resonance ionization spectroscopy, the IQC studies in such exceptionally complex atomic systems like protactinium became possible at first. The article *Intrinsic quantum chaos and spectral fluctuations within the protactinium atom* comprises the findings and results of the investigations on quantum chaos in the Pa I spectrum. Amongst other insights, the proof was delivered that protactinium is a fully chaotic many-body system as presumed, e.g., by A.V. Viatkina et al. [68]. Due to the extremely high level density, full expression of chaotic behavior is visible already at excitation energies as low as 2 eV, implying that the onset of chaos must be located at even lower energies close to the ground state. Moreover, the influence of missing levels, which cannot be avoided in spectroscopy with finite resolution, on spectral fluctuations was investigated in great detail within this article.

With the results presented in the featured articles, this thesis contributes to the broad oeuvre of the Mainz LARISSA group and extends it into a new direction. On the one hand, the method of RIS and the validation of the Rydberg analysis was proven at highest precision as well as a most useful technique for enhancement of the accessible wavelength range for the Mainz Ti:sapphire lasers was accomplished. On the other hand, two new research fields with promising application areas were established: The development and application of specific analytic methods for the determination of ionization potentials applicable wherever classical procedures fail. On top of that, intrinsic quantum chaos was investigated as self-contained research field. In summary, these contributions lay the foundation for further application of the procedures and methods described in this work for the LARISSA working group at the University of Mainz and others.

Bibliography

[1] S. Rothe, A.N. Andreyev, S. Antalic, A. Borschevsky, L. Capponi, T.E. Cocolios, H. De Witte, E. Eliav, D.V. Fedorov, V.N. Fedosseev, D.A. Fink, S. Fritzsche, L. Ghys, M. Huyse, N. Imai, U. Kaldor, Y. Kudryavtsev, U. Köster, J.F.W. Lane, J. Lassen, V. Liberati, K.M. Lynch, B.A. Marsh, K. Nishio, D. Pauwels, V. Pershina, L. Popescu, T.J. Procter, D. Radulov, S. Raeder, M.M. Rajabali, E. Rapisarda, R.E. Rossel, K. Sandhu, M.D. Seliverstov, A.M. Södin, P. Van den Bergh, P. Van Duppen, M. Venhart, Y. Wakabayashi, and K.D.A. Wendt, *Measurement of the first ionization potential of astatine by laser ionization spectroscopy*. Nature Comm. **4**, 1835 (2013).

[2] D. Leimbach, J. Sundberg, Y. Guo, R. Ahmed, J. Ballof, L. Bengtsson, F. Boix Pamies, A. Borschevsky, K. Chrysalidis, E. Eliav, D. Fedorov, V. Fedosseev, O. Forstner, N. Galland, R.F. Garcia Ruiz, C. Granados, R. Heinke, K. Johnston, A. Koszorus, U. Köster, M.K. Kristiansson, Y. Liu, B. Marsh, P. Molkanov, L.F. Pašteka, J.P. Ramos, E. Renault, M. Reponen, A. Ringvall-Moberg, R.E. Rossel, D. Studer, A. Vernon, J. Warbinek, J. Welander, K. Wendt, Sh. Wilkins, D. Hanstorp, and S. Rothe, *The electron affinity of astatine*. arXiv:2002.11418 [physics.atom-ph] (2020).

[3] C. Mattolat, T. Gottwald, S. Raeder, S. Rothe, F. Schwellnus, K. Wendt, P. Thörle-Pospiech, and N. Trautmann, *Determination of the first ionization potential of technetium*. Phys. Rev. A **81**, 547 (2010).

[4] J. Roßnagel, S. Raeder, A. Hakimi, R. Ferrer, N. Trautmann, and K. Wendt, *Determination of the first ionization potential of actinium*. Phys. Rev. A **85**, 1478 (2012).

[5] D. Studer, S. Heinitz, R. Heinke, P. Naubereit, R. Dressler, C. Guerrero, U. Köster, D. Schumann, and K. Wendt, *Atomic transitions and the first ionization potential of promethium determined by laser spectroscopy*. Phys. Rev. A **99**, 062513 (2019).

[6] R.V. Ambartzumian and V.S. Letokhov, *Selective Two-Step (STS) Photoionization of Atoms and Photodissociation of Molecules by Laser Radiation*. Appl. Optics **11**, 354 (1972).

[7] V.S. Letokhov and V.I. Mishin, *Highly selective multistep ionization of atoms by laser radiation*. Opt. Commun. **29**, 168 (1979).

[8] B. Cheal and K.T. Flanagan, *Progress in laser spectroscopy at radioactive ion beam facilities*. J. Phys. G: Nucl. Part. Phys. **37**, 113101 (2010).

[9] P. Campbell. I.D. Moore, and M.R. Pearson, *Laser spectroscopy for nuclear structure physics*. Prog. Part. Nucl. Phys. **86**, 127 (2016).

[10] M. Franzmann, *A New Tool for Ultra-Trace Analysis of Radionuclides – Setup, Optimization and Characterization of the Resonant Laser-SNMS System for IRS Hannover*. PhD thesis, Gottfried Wilhelm Leibniz Universität Hannover (2018).

[11] R. Menzel, *Photonics - Linear and Nonlinear Interactions of Laser Light and Matter*. 978-3-540-23160-8. Springer, 2. edition (2007).

[12] A.E. Siegman, *Lasers*. 0-935702-11-5. University Science Books (1986).

[13] W.T. Silfvast. *Laser Fundamentals*. 978-0-521-55617-0. Cambridge University Press (1996).

[14] S. Rothe, *An all-solid state laser system for the laser ion source RILIS and in-source laser spectroscopy of astatine at ISOLDE/CERN*. PhD thesis, Johannes Gutenberg-Universität Mainz (2012).

[15] P. Naubereit, *Weiterentwicklung eines weitabstimmbaren Titan:Saphir-Lasers und sein Einsatz zur Spektroskopie hochliegender Resonanzen in Holmium*. Master thesis, Johannes Gutenberg-Universität Mainz (2014).

[16] T. Kron, *Pushing the Limits of Resonance Ionization Mass Spectrometry -– Ionization Efficiency in Palladium and Spectral Resolution in Technetium*. PhD thesis, Johannes Gutenberg-Universität Mainz (2017).

[17] P. Moulton, *Ti-doped sapphire: tunable solid-state laser*. Opt. News, **8**:6, 9 (1982).

[18] S. Rothe, B.A. Marsh, C. Mattolat, V.N. Fedosseev, and K. Wendt, *A complementary laser system for ISOLDE RILIS*. J. Phys.: Conf. Ser. **312**, 052020 (2011).

[19] R.W. Boyd, *Nonlinear Optics*. 978-0-12-369470-6. Academic Press, 3. edition (2008).

[20] V. Sonnenschein, I.D. Moore, I. Pohjalainen, M. Reponen, S. Rothe, and K. Wendt, *Intracavity Frequency Doubling and Difference Frequency Mixing for Pulsed ns Ti:sapphire Laser Systems at On-line Radioactive Ion Beam Facilities*. JPS Conf. Proc. **6**, 030126 (2015).

[21] M. Franzmann, *Resonanzionisations-Massenspektrometrie an Aktiniden mit der Mainzer Atomstrahlquelle MABU*. Diploma thesis, Johannes Gutenberg-Universität Mainz (2013).

[22] T. Gottwald, *Studium hochkomplexer atomarer Spektren mittels Methoden der Laserresonanzionisation*. PhD thesis, Johannes Gutenberg-Universität Mainz (2010).

[23] W. Demtröder, *Laserspektroskopie 1*. 978-3-642-21305-2. Springer, 6. edition (2011).

[24] W. Demtröder, *Laserspektroskopie 2*. 978-3-642-21446-2. Springer, 6. edition (2013).

[25] S. Rothe, B. A. Marsh, C. Mattolat, V. N. Fedosseev, and K. Wendt, *A complementary laser system for ISOLDE RILIS*. J. Phys.: Conf. Ser. **312**, 052020 (2011).

[26] T.E. Cocolios, H.H. Al Suradi, J. Billowes, I. Budinčević, R.P. de Groote, S. De Schepper, V.N. Fedosseev, K.T. Flanagan, S. Franchoo, R.F. Garcia Ruiz, H. Heylen, F.Le Blanc, K.M. Lynch, B.A. Marsh, P.J.R. Mason, G. Neyens, J. Papuga, T.J. Procter, M.M. Rajabali, R.E. Rossel, S. Rothe, G.S. Simpson, A.J. Smith, I. Strashnov, H.H. Stroke, D. Verney, P.M. Walker, K.D.A. Wendt, and R.T.Wood, *The Collinear Resonance Ionization Spectroscopy (CRIS) experimental setup at CERN-ISOLDE*. Nucl. Instr. Meth. B **317**, 565 (2013).

[27] N. Lecesne, R. Alvès-Condé, E. Coterreau, F. De Oliveira, M. Dubois, J.L. Flambard, H. Franberg, T. Gottwald, P. Jardin, J. Lassen, F. Le Blanc, R. Leroy, C. Mattolat, A. Olivier, J.Y. Pacquet, A. Pichard, S. Rothe, M.G. Saint-Laurent, and K. Wendt, *GISELE: A resonant ionization laser ion source for the production of radioactive ions at GANIL*. Rev. Sci. Instrum. **81**, 02A910 (2010).

[28] J. Lassen, P. Bricault, M. Dombsky, J.P. Lavoie, Ch. Geppert, and K. Wendt, *Resonant Ionization Laser Ion Source Project at TRIUMF*. Hyperfine Interact. **162**, 69 (2006).

[29] M. Reponen, I.D. Moore, T. Kessler, I. Pohjalainen, S. Rothe, and V. Sonnenschein, *Laser developments and resonance ionization spectroscopy at IGISOL*. Eur. Phys. J. A **48**, 45 (2012).

[30] T. Sonoda, M. Wada, H. Tomita, C. Sakamoto, T. Takatsuka, T. Noto, H. Iimura, Y. Matsuo, T. Kubo, T. Shinozuka, T. Wakui, H. Mita, S. Naimi, T. Furukawa, Y. Itou, P. Schury, H. Miyatake, S. Jeong, H. Ishiyama, Y. Watanabe, and Y. Hirayama, *Development of a gas cell-based laser ion source for RIKEN PALIS*. Hyperfine Interact. **216**, 103 (2013).

[31] R. Ferrer, V.T. Sonnenschein, B. Bastin, S. Franchoo, M. Huyse, Yu. Kudryavtsev, T. Kron, N. Lecesne, I.D. Moore, B. Osmond, D. Pauwels, D. Radulov, S. Raeder, L. Rens, M. Reponen, J. Roßnagel, H. Savajols, T. Sonoda, J.C. Thomas, P. Van den Bergh, P. Van Duppen, K. Wendt, and S. Zemlyanoy, *Performance of a high repetition pulse rate laser system for in-gas-jet laser ionization studies with the Leuven laser ion source @ LISOL*. Nucl. Instr. Meth. B **291**, 29 (2012).

[32] R. Ferrer, A. Barzakh, B. Bastin, R. Beerwerth, M. Block, P. Creemers, H. Grawe, R. de Groote, P. Delahaye, X. Fléchard, S. Franchoo, S. Fritzsche, L.P. Gaffney, L. Ghys, W. Gins, C. Granados, R. Heinke, L. Hijazi, M. Huyse, T. Kron, Yu. Kudryavtsev, M. Laatiaoui, N. Lecesne, M. Loiselet, F. Lutton, I.D. Moore, Y. Martínez, E. Mogilevskiy, P. Naubereit, J. Piot, S. Raeder, S. Rothe, H. Savajols, S. Sels, V. Sonnenschein, J.-C. Thomas, E. Traykov, C. Van Beveren, P. Van den Bergh, P. Van Duppen, K. Wendt, and A. Zadvornaya, *Towards high-resolution laser ionization spectroscopy of the heaviest elements in supersonic gas jet expansion*. Nat. Commun. **8**, 14520 (2017).

[33] C. Granados, P. Creemers, R. Ferrer, L. P. Gaffney, W. Gins, R. de Groote, M. Huyse, Yu. Kudryavtsev, Y. Martínez, S. Raeder, S. Sels, C. Van Beveren, P. Van den Bergh, P. Van Duppen, K. Wrzosek-Lipska, A. Zadvornaya, A. E. Barzakh, B. Bastin, P. Delahaye, L. Hijazi, N. Lecesne, F. Luton, J. Piot, H. Savajols, J.-C. Thomas, E. Traykov, R. Beerwerth, S. Fritzsche, M. Block, X. Fléchard, S. Franchoo, L. Ghys, H. Grawe, R. Heinke, T. Kron, P. Naubereit, K. Wendt, M. Laatiaoui, I. Moore, V. Sonnenschein, M. Loiselet, E. Mogilevskiy, and S. Rothe, *In-gas laser ionization and spectroscopy of actinium isotopes near the N=126 closed shell*. Phys. Rev. C **96**, 054331 (2017).

[34] L.R. Morss, N.M. Edelstein, J. Fuger, and J.J. Katz (*Eds.*), *The Chemistry of the Actinide and Transactinide Elements*. 978-1-4020-3555-5. Springer, 3. edition (2006).

[35] C. Keller, *The Chemistry of Protactinium*. Angew. Chem. internat. Edit. **5**, 23 (1966).

[36] J. Sugar, *The Chemistry of Protactinium*. J. Chem. Phys. **59**, 788 (1973).

[37] K. Wendt, T. Gottwald, C. Mattolat, and S. Raeder, *Ionization potentials of the lanthanides and actinides – towards atomic spectroscopy of super-heavy elements*. Hyperfine Interact. **227**, 55 (2014).

[38] K. Fajans, *Die radioaktiven Umwandlungen und das periodische System der Elemente*. Ber. Dtsch. Chem. Ges. **46**, 422 (1913).

[39] F. Soddy, *The Radio-Elements and the Periodic Law*. Nature **91**, 57 (1913).

[40] P. Curie, *Sur la variation avec le temps de l'activité de quelques substances radioactives*. Radium **8**, 353 (1911).

[41] O. Hahn and L. Meitner, *Die Muttersubstanz des Actiniums, ein Neues Radioaktives Element von Langer Lebensdauer*. Phys. Z. **19**, 208 (1918).

[42] L. Meitner, *Die Muttersubstanz des Actiniums, Ein Neues Radioaktives Element von Langer Lebensdauer*. Z. Elektrochem. **24**, 169 (1918).

[43] *Protactinium*, From Wikipedia, the free encyclopedia [Online]. Available: https://en.wikipedia.org/wiki/Protactinium [Wed April 18 2018].

[44] V.V. Flambaum, A.A. Gribakina, G.F. Gribakin, and M.G. Kozlov *Structure of compound states in the chaotic spectrum of the Ce atom: Localization properties, matrix elements, and enhancement of weak perturbations*. Phys. Rev. A **50**, 267 (1994).

[45] W. Ritz *Magnetische Atomfelder und Serienspektren*. Ann. Phys. **330**, 660 (1908).

[46] N. Erdmann, M. Nunnemann, K. Eberhardt, G. Herrmann, G. Huber, S. Köhler, J.V. Kratz, G. Passler, J.R. Peterson, N. Trautmann, and A. Waldeck, *Determination of the first ionization potential of nine actinide elements by resonance ionization mass spectroscopy (RIMS)*. J. Alloy. Compd. **271-273**, 837 (1998).

[47] J.R. Peterson, N. Erdmann, M. Nunnemann, K. Eberhardt, G. Huber, J.V. Kratz, G. Passler, O. Stetzer, P. Thörle, N. Trautmann, and A. Waldek, *Determination of the First Ionization Potential of Einsteinium by Resonance Ionization Mass Spectroscopy (RIMS)*. J. Alloy. Compd. **271-273**, 876 (1998).

[48] D. Studer, *Probing atomic and nuclear structure properties of promethium by laser spectroscopy*. PhD thesis, Johannes Gutenberg-Universität Mainz (2020).

[49] J. Hostetter, J.D. Pritchard, J.E. Lawler, and M. Saffman, *Measurement of holmium Rydberg series through magneto-optical trap depletion spectroscopy*. Phys. Rev. A **91**, 012507 (2015).

[50] M. Ciocca, C.E. Burkhardt, J.J. Leventhal, and T. Bergeman, *Precision Stark spectroscopy of sodium: Improved values for the ionization limit and bound states*. Phys. Rev. A **45**, 4720 (1992).

[51] J.F. Baugh, C.E. Burkhardt, J.J. Leventhal, and T. Bergeman, *Precision Stark spectroscopy of sodium ^2P and ^2D states*. Phys. Rev. A **58**, 1585 (1998).

[52] A.A. Gribakina, and G.F. Gribakin, *Perturbation of Rydberg series by atomic compound states*. J. Phys. B: At. Mol. Opt. Phys. **29**, L809 (1996).

[53] M.L. Mehta, *Random Matrices*. Academic Press, New York, 3. edition (2004).

[54] T. Guhr, A. Müller-Groeling, and H.A. Weidenmüller, *Random-Matrix Theories in Quantum Physics: Common Concepts*. Phys. Rep. **299**, 189 (1998).

[55] T. Guhr, *Quantenchaos*. Lecture Notes, University of Duisburg-Essen (2014).

[56] H.-J. Stöckmann, *Quantum Chaos – An Introduction*. Cambridge University Press, Cambridge, 1. edition (with corrections) (2006).

[57] W.G. Kelley, A.C. Peterson, *The Theory of Differential Equations: Classical and Qualitative*. Springer Science+Business Media, LLC, New York, 2. edition (2010).

[58] P. Walters, *An Introduction to Ergodic Theory*. Springer-Verlag, New York (1982).

[59] *Double Pendulum*. Photograph by Cristian V. (2014), distributed under a CC BY-SA 4.0 license.

[60] P. Jung, *The emergence of stable limits from chaotic billiard models*, From KAIST Compass for Natural and Life Sciences [Online]. Available: http://kaistcompass.kaist.ac.kr/?magazine=the-emergence-of-stable-limits-from-chaotic-billiard-models&ckattempt=2 [Wed October 24 2018].

[61] M.V. Berry, and M. Robnik, *Statistics of energy levels without time-reversal symmetry: Aharonov-Bohm chaotic billiards*. J. Phys. A: Math. Gen. **19**, 649 (1986).

[62] N. Bohr, *Über die Serienspektra der Elemente*. Z. Physik **2**, 423 (1920).

[63] N. Rosenzweig, and C.E. Porter, *"Repulsion of Energy Levels" in Complex Atomic Spectra*. Phys. Rev. **120**, 1698 (1960).

[64] E.P. Wigner, *On a Class of Analytic Functions from the Quantum Theory of Collisions*. Ann. Math. **53**, 1 (1951)

[65] E.P. Wigner, *On the statistical distribution of the widths and spacings of nuclear resonance levels*. Math. Proc. Cambridge Philos. Soc. **47**, 790 (1951)

[66] O. Bohigas, M.J. Giannoni, and C. Schmit, *Characterization of Chaotic Quantum Spectra and Universality of Level Fluctuation Laws*. Phys. Rev. Lett. **52**, 1 (1984).

[67] D. Wintgen, H. Friedrich, *Classical and quantum-mechanical transition between regularity and irregularity in a Hamiltonian system*. Phys. Rev. A **35**, 1464(R) (1987).

[68] A.V. Viatkina, M.G. Kozlov, and V.V. Flambaum, *Prediction of quantum many-body chaos in the protactinium atom*. Phys. Rev. A **95**, 022503 (2017).